Clemson University
TigerPrints

All Theses | Theses

8-2019

Application of Electrical Resistivity Geophysical Monitoring for Detection of Preferential Flow

Jeffrey Britton Hundley Jr.
Clemson University, Silverliquid4100@hotmail.com

Follow this and additional works at: https://tigerprints.clemson.edu/all_theses

Recommended Citation
Hundley Jr., Jeffrey Britton, "Application of Electrical Resistivity Geophysical Monitoring for Detection of Preferential Flow" (2019). *All Theses*. 3188.
https://tigerprints.clemson.edu/all_theses/3188

This Thesis is brought to you for free and open access by the Theses at TigerPrints. It has been accepted for inclusion in All Theses by an authorized administrator of TigerPrints. For more information, please contact kokeefe@clemson.edu.

APPLICATION OF ELECTRICAL RESISTIVITY GEOPHYSICAL MONITORING FOR DETECTION OF PREFERENTIAL FLOW

A Thesis
Presented to
the Graduate School of
Clemson University

In Partial Fulfillment
of the Requirements for the Degree
Master of Science
Hydrogeology

by
Jeffrey Britton Hundley, Jr.
August 2019

Accepted by:
Dr. Brian Powell, Committee Chair
Dr. Stephen Moysey
Dr. Christophe Darnault

ABSTRACT

Preferential flow is a common occurrence during infiltration yet is often not accounted for in predictive flow models. This has implications for contaminant transport in that the extent of constituent plumes are often underestimated, thereby reducing the effectiveness of any remediation efforts. Electrical resistivity monitoring could be a useful tool to determine if infiltration is bypassing parts of the subsurface through preferential flow pathways and to better inform predictive models. The viability of this method was evaluated through simple electrical simulations and with multiple column experiments across scales using advanced observation techniques like 4D computed tomography. Electrical resistivity was used to monitor the progression of uniform wetting fronts as well as preferential flow and infiltration through macropore networks. Results indicate that certain characteristics in the response of apparent resistivity to preferential flow are distinct from uniform flow. Vertical bulk resistivity reduces rapidly as wetting in a macropore network increases the connectivity between electrodes. Strong positive spikes in electrical anisotropy are observed during preferential flow events and the arrival of a wetting front observed through resistivity monitoring occurs much earlier than predicted using bulk soil properties. These characteristics indicate that electrical resistivity monitoring is a viable method for the application of detecting preferential flow during infiltration in a heterogeneous system.

DEDICATION

I would like to dedicate this work to my fiancée, Allison Sams, who has loved and supported me through the trials of this adventure and to my wonderful parents, Jeff and Penny Hundley, who have provided for me all the resources and encouragement that I needed to be who and where I am today.

ACKNOWLEDGMENTS

I would like to acknowledge my advisors, Drs. Stephen Moysey and Brian Powell for their guidance and insight in producing the following work and in my professional and personal development. Thank you to Abdullah Al. Mamun for lending me his knowledge and expertise in our collaborations. Thank you to Kayla Collins for her technical support in developing the lysimeter pan at Clemson and Rodney Merek for his assistance machining experimental parts. Also, I would like to thank the Dr. Moysey research group for their help and support.

TABLE OF CONTENTS

Page

TABLE OF CONTENTS
(CONTINUED)

Page

TABLE OF CONTENTS
(CONTINUED)

Page

LIST OF FIGURES

LIST OF FIGURES
(CONTINUED)

Figure Page

LIST OF FIGURES
(CONTINUED)

Figure Page

LIST OF EQUATIONS

LIST OF ABBREVIATIONS

CT ..... Computed Tomography

DoE ..... Department of Energy

DDI..... Distilled De-ionized Water

EC ..... Electrical Conductivity

ER ..... Electrical Resistivity

ERT ..... Electrical Resistivity Tomography

PVC ..... Polyvinyl Chloride

RadFLEx ..... Radionuclide Field Lysimeter Experiment

RadFATE ..... Radionuclide Fate and Transport Experiment

SRS..... Savannah River Site

VWC..... Volumetric Water Content

SECTION 1: INTRODUCTION

1.1 PURPOSE OF RESEARCH

Earth is referred to as the watery planet as it is the only object in the universe known to have an abundance of liquid water on its surface which makes it suitable to sustain life. Water cycles across our planet and is used by plants, wildlife and humans alike as a fundamental part of our biology. Clean water is an invaluable resource that has an ever increasing importance as earth's population grows and expands. Contamination of water sources is an inevitable problem in this modern world with sprawling industry and agriculture. Industrial solvents, pesticides, petroleum products, radionuclides and more can be found in rivers, lakes and aquifers and we must improve our knowledge of how to clean these contaminants from water sources to minimize health risks to consumers.

Contaminants are often introduced by spills into the ground which penetrate down through the subsurface and reside within the earth or interact with water in aquifers. It is critical to improve our understanding of these processes in order to effectively remediate environmental damage. Hydrologists have worked for decades to quantitatively describe the movement of water through earth materials. The achievements of scientists such as Henry Darcy and Lorenzo Richards established the foundations of modern hydrology but much of their work was based on controlled

laboratory experiments and not observations of complex natural processes. Richards proposed an equation describing flow through unsaturated porous media in his 1931 publication but his equation has assumptions of homogeneity and held many variable hydraulic parameters constant (Jarvis, 2007).

Concerns arose with this method of describing and predicting flow when strongly sorbing contaminants such as pesticides, which under Richards' framework should be trapped in near surface soils, began to be routinely found in groundwater quality sampling (Beven, 2013). Somehow infiltrating contaminants were not being filtered out in the soil matrix but passing through the subsurface and finding their way into aquifers and reservoirs. Such behavior could be explained by the preferred channeling of water through certain parts of the ground or preferential flow pathways.

As early as the mid-19th century, scientists began describing observations of preferential flow behavior and recognizing its importance (Beven, 2013). Preferential flow behavior still remains challenging to accurately quantify and predict despite significantly increasing research effort focused on the topic in recent years. There are several mechanisms that have been identified at different scales to cause preferential flow in the subsurface, such as flow instability at a layer boundary, air entrapment, soil aggregation, or bioturbation (Fig. 1). In some cases, observations have been made of turbulent flow regimes occurring in natural macropore structures where infiltration bypasses the soil matrix with velocities on the order of meters per hour (Jarvis, 2007).

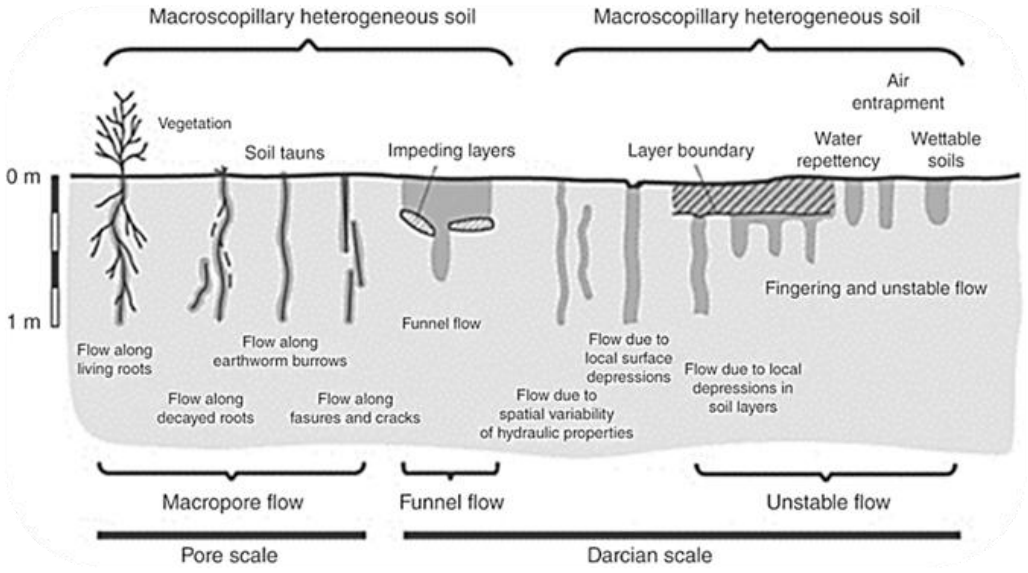

Figure 1: Representation of different types of preferential flow mechanisms in the vadose zone. (Bogaard, 2015)

The need to predict flow through systems with macropores or other preferential pathways has led to the development of methods like the van Genuchten dual-porosity model or newer dual-permeability methods like the Gerke and van Genuchten model or other approaches like the kinematic wave equation (Simunek, 2003). Still, there are many unknown aspects of preferential flow behavior as it is difficult to study at the scales of practical applications. Advances in technology and experimental approaches like 3D computer tomography and continuous monitoring will enable researchers to enhance our knowledge of these processes (Jarvis, 2007). Furthermore, the ability to "develop methods to support predictive modeling of the impacts of macropore flow on water quality at the landscape scale" (Jarvis, 2007) is key to the successful application of our knowledge to enhance the effectiveness of remediation efforts.

One such geophysical method is the electrical resistivity (ER) sensing technique, which can be applied across scales to continuously monitor infiltration and provide additional hydrologic data on a particular area of interest. Resistivity is an intrinsic property of a material related to the ease at which electrical current can flow through the material. In earth material such as soil, resistivity is a function of its properties such as mineralogy, pore volume and structure, the amount of fluid in the pore space and its conductivity as well as temperature. ER measurements are typically made using four electrodes spaced at precise distances along a transect of the ground surface where two electrodes provide current flow and two electrodes measure voltage (Fig. 2).

Alternating current is introduced into the subsurface and, in the ideal case of a homogeneous material, current flows between electrodes A and B to produce a potential field that is symmetric about the midpoint between current electrodes (Herman, 2001). Difference in potential is measured at electrodes M and N and by accounting for the current injected and the geometry of the electrode array, a resistivity value can be assigned for the measured region. Multiple measurements can be made along a transect and with varying electrode separation to create a profile of the subsurface and through inversion a tomogram of resistivity distribution can be produced. Alternatively, measurements can

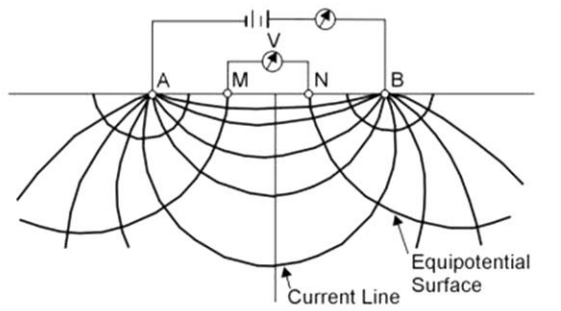

Figure 2: Four electrode 'Wenner' ER array in homogenous half-space. Current and potential fields are represented with contour lines. A and B mark current electrodes, M and N mark potential electrodes. (Wightman, 2003)

also be made repeatedly with a stationary electrode array through time to monitor changes in the resistivity of the subsurface as a result of groundwater flow.

Simple ER monitoring methods have the potential to be used for determining effective hydraulic parameters of groundwater systems (Fowler, 2011). Experimental observations have also indicated that electrical resistivity monitoring is also responsive to changes in active porosity of macropore networks within a soil system (Liu, 2012a). When flow becomes active within connected pathways, which bypass parts of the soil matrix in an observed region, the material is better able to conduct current and ER monitoring is sensitive to those changes. Electrical resistivity monitoring has potential to be a simple and cost effective tool to assess dominant flow mechanisms in the field and provide additional information to more accurately predict the spread of harmful contaminants.

1.2 SPECIFIC APPLICATION

The Savannah River Site (SRS) is a 310 acre facility in Aiken, South Carolina operated by the Department of Energy (DoE) that has been in operation for more than sixty years. In the past, the site has been host to nuclear reactors built to produce weapons grade material for national defense as well as multiple processing facilities and nuclear waste management facilities (SRS, 2019). Since the end of the cold war production of weapons grade materials has ceased and emphasis has shifted to the treatment and management of nuclear waste (SRS, 2019). Several nuclear waste storage

tanks have been constructed at the SRS to hold millions of gallons of material (Fig. 3). Over the years, accidental release of radionuclide material from different facilities at the site has caused contamination of substantial tracts of land.

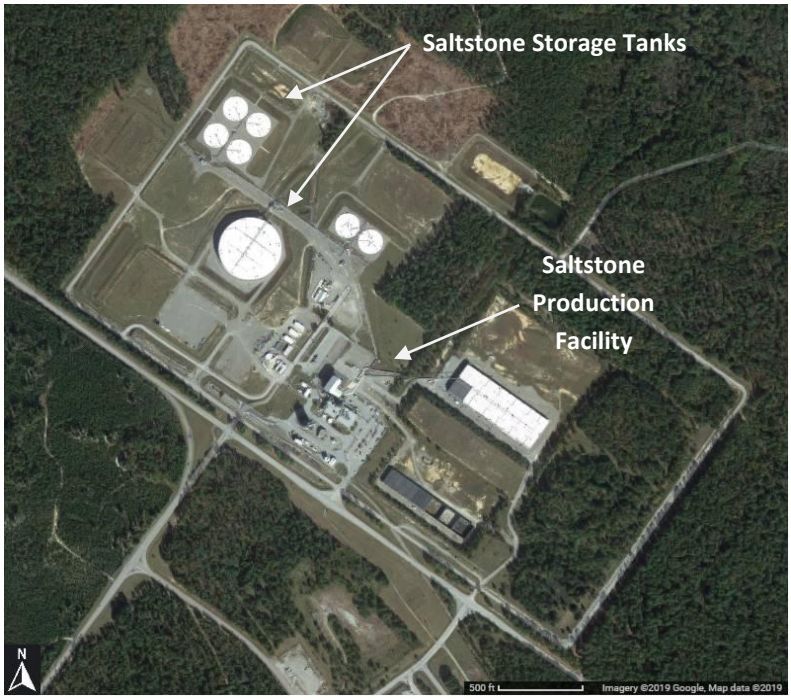

Figure 3: Satellite image of waste materials storage facilities at SRS, Aiken, SC. (Google, 2019)

Savannah River National Laboratory initialized a long term project to better understand behavior of contaminants at the site by developing the radionuclide field lysimeter experiment (RadFLEx) testbed (Fig. 4). Each RadFLEx lysimeter has a depth of 2 feet and diameter of 4 inches, is open to natural rainfall and has an effluent collection system to monitor concentration of radionuclide's coming from a source material contained within the soil in the column. Clemson University expanded on this project through the established program to stimulate competitive research (EPSCoR) by developing the radionuclide fate and transport experiment (RadFATE) testbed (Fig. 5). Using slightly larger 6 inch diameter lysimeter columns, advanced sensing methods could be integrated into the column design for monitoring conditions in the soil system.

Figure 4: Savannah River National Labs RadFLEx lysimeter facility at the DoE SRS.

Figure 5: Clemson University RadFATE lysimeter facility at the Clemson research park.

RadFATE lysimeter columns provide a controlled environment to enable the observation of radionuclide behavior under different biogeochemical conditions in physically complex heterogeneous systems (Powell, 2017). The extent of contaminated area at the SRS has been underestimated in many cases and unexpected anomalous transport of radionuclide material has been observed in RadFLEx lysimeters, both indicating that the behavior of radionuclides in these complex systems is not yet fully understood (Powell, 2017). Tools like ER monitoring could be help to improve the

effectiveness of remediation efforts by characterizing flow processes in the field and assisting predictive modeling.

SECTION 2: METHODOLOGY

The approach taken in this study to determine the feasibility of using electrical resistivity geophysical methods to detect the occurrence of preferential flow is to assess conceptual foundations using numerical modeling and to further investigate using empirical methods. Soil columns are traditional platforms used to examine flow processes in soils and are improved in this case with the incorporation of advanced monitoring techniques. Smaller scale columns are designed to monitor infiltration into unsaturated soil using ER while simultaneously capturing high resolution 4D X-ray computed tomography (CT) scans of the entire system. Larger scale columns or lysimeters are used to provide an analog to the vadose zone of a field environment that can be more closely monitored and controlled. Macroporous and non-macroporous soil systems are included in each experimental scale. The empirical approach not only requires controlled experimental platforms but also calibration experiments and an assessment of error to provide confidence in data and observations.

2.1 PHYSICAL SIMULATION

Simulation or numerical modeling is a powerful tool which can be used to provide insight and improve understanding of physical processes. COMSOL Multiphysics is a comprehensive physics modeling software that is effective at simulating laboratory

scale processes. Here, COMSOL is utilized to simulate electrical response to flow in macroporous and non-macroporous systems as a preliminary investigation to the feasibility of using electrical resistivity methods to detect preferential flow. Examination of this problem is done by using a simple 2D stationary study configuration where only electrical physics are used. Wetting fronts are represented by geometry elements which are assigned electrical conductivity (EC) values which are lesser than the EC values assigned to the background representative of a soil matrix. Geometries representative of fluid distributions at different times during wetting are produced manually by progressing the wetted area geometry through space and recalculating the model at each step. Geometry of wetted regions is designed to be either the idealized uniform wetting front scenario or a macropore dominated flow scenario produced to roughly represent a cross-section of a desiccation crack through soil (Fig. 6). Models are run for four different scenarios consisting of macroporous and non-macroporous systems with electrode arrays oriented both vertically and horizontally.

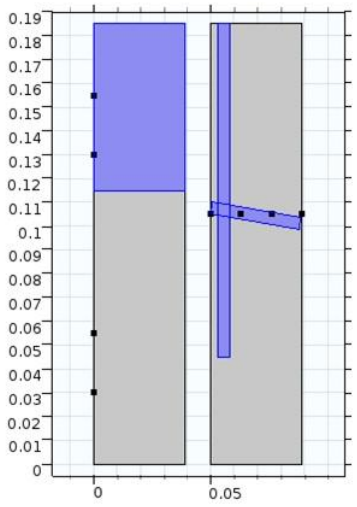

Figure 6: Illustration of each models geometry design at a particular time step. Electrodes are represented by black dots, blue represents fluid and grey represents soil matrix.

In the non-macroporous cases the background EC is set to 100 S/m and the wetted region is set to 300 S/m, where in the macroporous cases the background EC is

set to 1 S/m and the wetted region is again set to 300 S/m to produce slightly more contrast. Also in non-macroporous cases a total of 18 model geometries were simulated and in macroporous cases a total of 20 model geometries were evaluated. Electrical physics were calculated by COMSOL using equations 1 and 2 in a stationary 2D space (no time-dependence) (COMSOL, 2019).

$$J = \sigma E \quad \text{(Equation 1)}$$

Where σ is electrical conductivity, E is the electrical field. Current J is applied at the current electrodes.

$$E = -\nabla V \quad \text{(Equation 2)}$$

Where V is electrical potential.

2.2 ELECTRICAL RESISTIVITY MONITORING

During experiments, ER measurements are taken using an IRIS Instruments SYSCAL-Pro device with a 48 channel switch box. The SYSCAL-Pro is controlled remotely using the COMSYS-Pro software package which allows scheduled and continuous data collection. Electrical resistivity tomography (ERT) images can be collected in the Lysimeter columns as supplementary data to aid interpretations. ERT images are produced using R2 inversion software developed by Andrew Binley of Lancaster

University (Binley, 2013). MATLAB software is used to produce input files and run the R2 software as well as compile, process and plot 1D bulk ER data measurements.

Relating bulk ER measurements of resistivity to apparent water content is possible through the application of Archie's Law (Eqn. 3) (Archie, 1942). Archie's Law is applied here under the assumption that physical soil properties in the system are constant and that saturation is the dominant parameter. For this relationship to be meaningful however, calibration experiments must be done to find parameters *a, m* and *n* for the specific soil being used.

$$\rho_b = a\phi^{-m}S_w^{-n}\rho_w \qquad \text{(Equation 3)}$$

Where ρ_b is bulk resistivity (ohm-m), *a* is the tortuosity factor, ϕ is soil porosity, S_w is soil saturation, ρ_w is fluid resistivity (ohm-m), *m* describes the degree of soil cementation and *n* describes the connectivity of the fluid phase.

Calibration experiments were done in the laboratory using a Humboldt soil box connected to the IRIS SYSCAL-Pro (Fig. 7). Prior to sample preparation, SRS soil intended for common use throughout all experiments was sieved using a soil sieve with 2mm aperture size. Porosity of the SRS soil was found by packing a steel cylinder of a known volume with soil and allowing it to saturate from the bottom up and then measuring change in the mass of the system and calculating the volume of fluid stored (Appx. 2.2). Porosity was estimated to be 43% based on the results of multiple duplicate

measurements. Initial calibration measurements were made with the Humboldt box filled with various solutions (no soil)

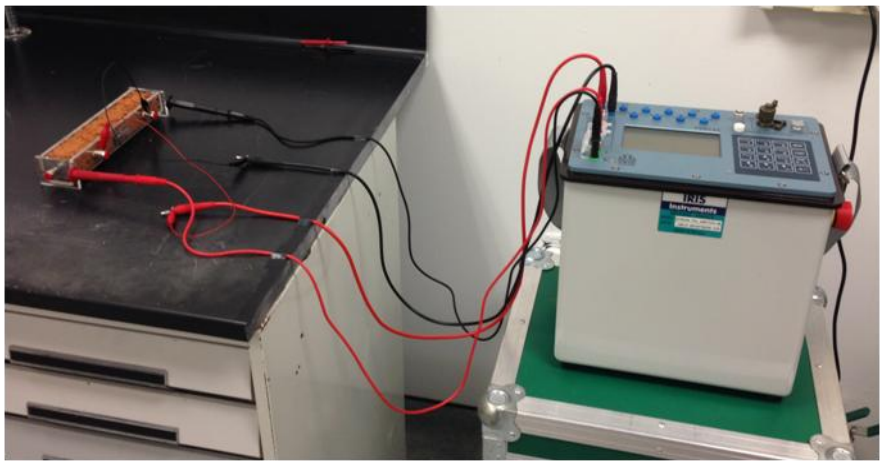

Figure 7: SRS soil sample prepared in a Humboldt soil box being measured by an IRIS Instruments SYSCAL-Pro resistivity meter.

to determine the resistance of the fluid solutions to be mixed with soil to prepare calibration samples and to determine the geometric factor (Eqn. 4) of the electrode array in box. The geometric factor converts measured resistance to resistivity by accounting for the geometry of electrode locations in the specific system.

$$K = \frac{\rho_w}{R} \qquad \text{(Equation 4)}$$

Where K is the geometric factor, ρ_w is the fluid resistivity (ohm-m) and R is the measured fluid resistance (ohms).

Solutions used for calibration were distilled de-ionized water (DDI), tap water from the lab faucet, and half gram per liter concentration increments of Sodium Chloride solution between 0 and 3 grams. Soil samples were prepared to 25%, 37.5%, 50%, 62.5% and 75% saturation for each of these solutions and measured in the Humboldt soil box with the IRIS resistivity meter. Data were fit to Archie's Law (Eqn. 3) by minimizing error solving for parameters a, m and n. Saturated data were additionally

fit to the Formation Factor (Eqn. 5) which is a function of the character of the material being measured (Archie, 1942).

$$F = \frac{\rho_b}{\rho_w} = a\phi^{-m} \quad \text{(When } S_w=1\text{)} \qquad \text{(Equation 5)}$$

Where *F* is the formation factor, ρ_b is bulk resistivity (ohm-m), ρ_w is fluid resistivity (ohm-m), *a* is the tortuosity factor, ϕ is soil porosity, and *m* describes the degree of soil cementation.

2.3 ERROR ASSESSMENT

Identifying sources of error is important in any scientific application but especially when using geophysical sensing methods as there are many potential sources of error contribution. For example, ER measurements can be affected by contact resistance between material and electrode, highly resistive target material, charge buildup at the electrode or low signal to noise ratio from interference (Singh, 2013). Many of these measurement issues are resolved by using a quadripole or a four electrode configuration with proper cable shielding (Singh, 2013). In order to evaluate measurement error, each channel of the IRIS SYSCAL-Pro resistivity meter was tested by measuring circuit resistance across resistors of a known resistance value (Appx. 3.1, 3.2). Additionally, the quality of each electrode produced for resistivity monitoring was checked by measuring line resistance to ensure it was below a threshold of 1 ohm. All

cabling used had integrated shielding to reduce signal interference. Results of IRIS error analysis are presented in appendix section 3.

2.4 CT IMAGING COLUMNS

Smaller scale soil columns are designed to investigate the relationship between bulk electrical resistivity signals and the spatial distribution of fluid through time during infiltration events. These smaller columns are called 'CT imaging columns' as they are specifically designed to be housed in a vertically oriented MILabs Vector4 Pre-clinical X-ray computed tomography (CT) machine during unsaturated flow experiments (Fig. 8). The CT machine has an image resolution of 80 microns and a 7 minute scan duration which allows 4D monitoring of infiltration. Two soil columns are constructed for a series of experiments in the CT machine named 'CT1' and 'CT2'. Column CT1 is packed with SRS soil to be a homogenous or non-macroporous soil column, where column CT2 is packed with SRS soil to be macroporous with a network of desiccation cracks.

Figure 8: Clemson Universities MILabs Vector4 Pre-clinical CT machine with vertical imaging bed orientation.

Both of the CT columns share the same basic design and differ primarily by the structure of the soil matrix. The columns are constructed of clear polycarbonate tubing

and have a diameter of 3.9 cm and a height of 18.5 cm. The columns are capped at the top and bottom by machined PVC inserts with dual o-rings to prevent leakage as well as small diameter tube connections for secure influent and effluent lines. The upper caps are designed to hold the influent tubing at the center and slightly above the soil surface to allow slow drip infiltration. They are also vented to prevent pressure buildup at the upper boundary. The lower cap of column CT1 has a 1 atm porous ceramic plate insert flush against the soil base and CT2 has a central hole bored through the ceramic plate for direct drainage to effluent tubing. Each column has 30 electrodes oriented along 6

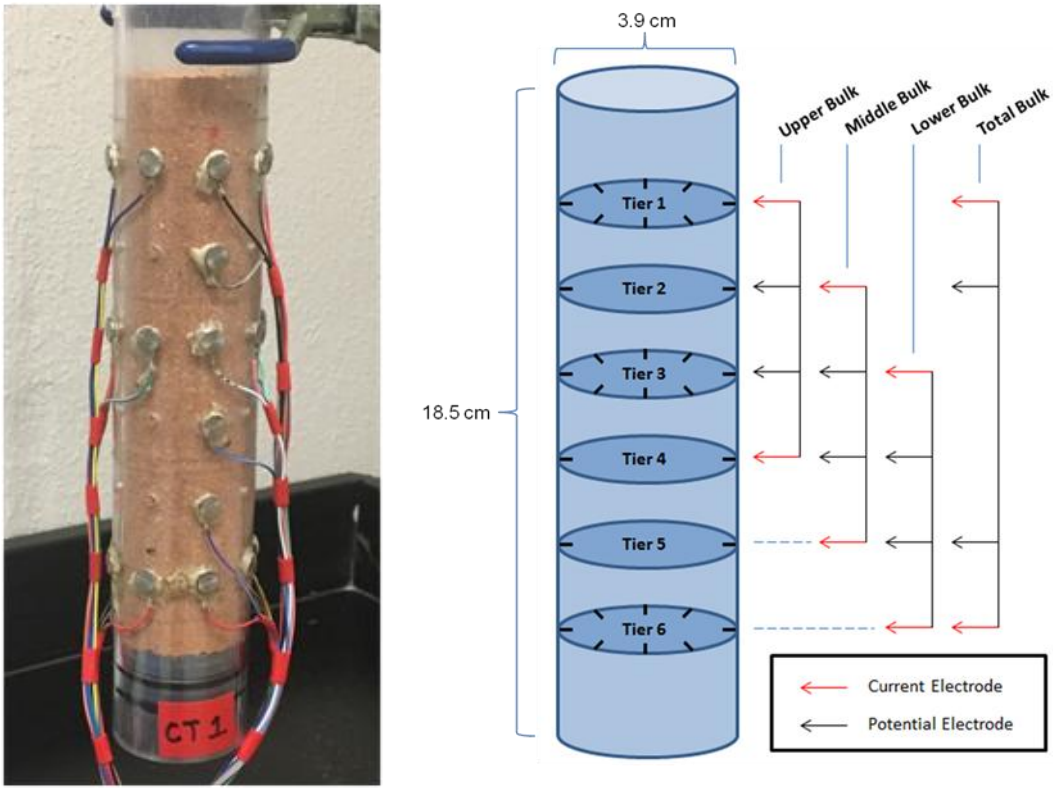

Figure 9: Image of column CT1 on left with glued steel electrodes prior to epoxy sealant application and upper cap installation. Shown to right, a schematic of electrode placement within the column at each electrode tier. Also indicated are vertical bulk electrical resistivity measurement configurations.

horizontal planes or electrode tiers in the column at soil depths of 3 cm, 5.5 cm, 8 cm, 10.5 cm, 13 cm, and 15.5 cm (Fig. 9). Electrode placement is designed to provide vertical bulk ER measurements averaged over the soil profile in the upper, middle, and lower regions as well as across the full column. Also, local bulk ER signals can be measured horizontally across the column at different orientations at electrode tiers 1, 3 and 6.

Column CT1 is designed to be non-macroporous by packing the soil into the column using a modified Proctor method (ASTM D-1557) to achieve a higher soil density to reduce likelihood of cracking when dried (Appx. 4.1). SRS soil is prepared at 12.5% volumetric water content (VWC) and added to the column in 2-3 cm layers, while being compressed by a drop weight between each layer addition. After packing, the column is allowed to dry by evaporation at the upper surface for roughly one month resulting in 56% moisture loss, resulting in a final VWC of 5.5%. Column CT2 is designed to be macroporous by packing using modified Proctor method with significantly higher water content at 32% (VWC) into the column and allowing it to dry by evaporation until roughly 90% moisture loss was achieved, forming a network of desiccation cracks (Appx. 4.2). Initial water content of the CT2 column is 3.2% (VWC) or 8% saturated.

2.5 CT IMAGING COLUMN EXPERIMENTS

Column experiments that were carried out within the X-ray CT machine share the same basic setup but differed in terms of boundary conditions and soil structure within the column. Experimental setup included a reservoir of influent solution,

delivered to the soils upper surface by an inline low flow peristaltic pump. Effluent drainage at the lower boundary was delivered to a fractional collector (Fig. 10). Bulk ER was monitored on a continuous cycle by the IRIS SYSCAL-Pro where each unique quadripole was measured approximately every 7 minutes. CT scans were also collected continuously at 15 minute intervals. Influent solution for all experiments was a 1 molar sodium iodide (NaI) solution intended as a contrast agent for X-ray imaging and conductive target for resistivity measurements.

The first CT column experiment conducted was with the non-macroporous column CT1. The upper boundary condition of the soil matrix was a constant flux with a

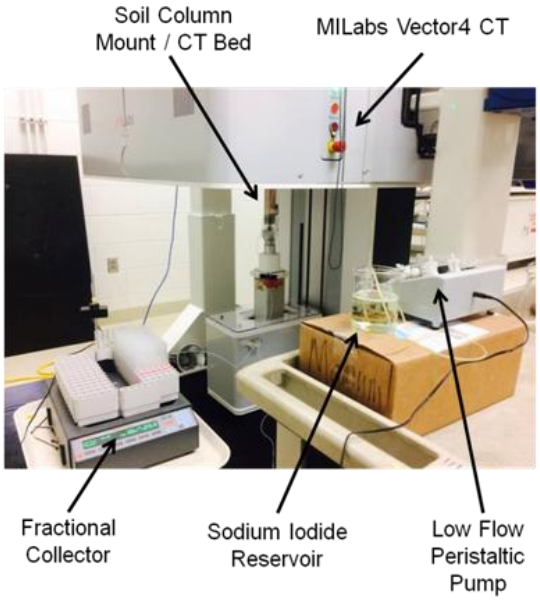

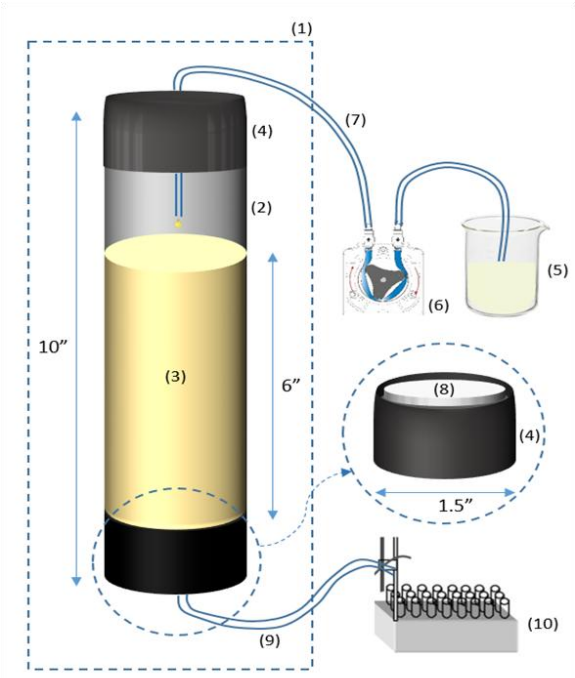

1. Setup inside CT
2. Polycarbonate Column
3. Soil Sample
4. Tube Cap
5. NaI Reservoir
6. Peristaltic Pump
7. Irrigation Tube
8. Porous plate at outlet
9. Outflow Tubing
10. Fractional Collector

Figure 10: Shown left, photo of the imaging laboratory during experiment. Shown to right, a schematic of the experimental setup (Modified from Mamun, 2018).

no flow condition at the lower boundary. Initial condition of the soil moisture in the column was 12% saturated. Flow was applied for a period of 13 hours at a rate of 0.11 mL/min. After flow was stopped, the upper cap of the column was then removed to allow evaporative drying while bulk ER measurements continued to be collected.

Progressing to experimentation with the macroporous column featuring a desiccation crack network, column CT2 was used to conduct a flow experiment structured similarly to the CT1 study. Low flow continuous infiltration was used to investigate fluid interaction between the soil matrix and macropore network and the bulk ER response to observed flow behavior. The upper boundary condition of the soil matrix was a constant flux with a lower boundary condition of constant atmospheric pressure. Initial condition of the soil moisture in the column was less than 10% saturated. Flow was applied for a period of 8 hours at a rate of 0.11 mL/min and an additional 2 hour period at an increased rate of 0.69 mL/min. Flow was increased after the wetting front progressed to the base of the soil profile in an effort to saturate the macropore network.

Resulting data from these experiments is intended for comparison of bulk ER response to similar infiltration events on differing soil structures and associated flow behavior. Applying a linear mixing law (Eqn. 6) presented by Luo et al. 2008, water content can be determined from CT scan data using a calibrated model (Eqn. 7) (Mamun, 2018).

$$CT(x,y,z) = CT_{solid}(x,y,z) * [1 - \phi(x,y,z)] + CT_{liquid}(x,y,z) * \phi(x,y,z) * S_{liquid} + CT_{gas}(x,y,z) * \phi(x,y,z) * S_{gas} \quad \text{(Equation 6)}$$

Where *CT* is voxel intensity value, ϕ is porosity and *S* is saturation. (Lou, et al. 2008)

$$\theta(x,y,z,t) = \frac{CT_{wet\ scan}(x,y,z,t) - CT_{dry\ scan}(x,y,z)}{CT_{NaI}(x,y,z) - CT_{air}} \quad \text{(Equation 7)}$$

Where *Θ* is volumetric water content, and *CT* is voxel intensity value.

2.6 LYSIMETER COLUMNS

Larger scale soil columns or lysimeters were designed to provide a controlled system which acts as an analog to the field environment. Seven lysimeter columns were produced in total; two of which were used in the laboratory for this study and five of which were deployed into the RadFATE facility at the Clemson University research park (Fig. 11). RadFATE lysimeters are all 6 inch diameter columns with 24 inches of soil depth and space above the soil for 4 inches of ponding depth. Columns are constructed with a PVC pipe creating the column walls, a PVC gasket on the top of the column for mounting the column from a hanging position, a perforated PVC disc at the base of the column with nylon mesh adhered to its upper surface to retain soil, and PVC pipe reducers to drain effluent into a 0.5 inch tube connection at the bottom. Each column is also equipped with multiple sensors to measure water content, matric potential,

temperature, electrical conductivity and total mass, as well as multiple electrode arrays to measure bulk ER and take cross sectional ERT images.

Lysimeters are mounted by suspension from a three point load cell assembly which monitors fluctuations in mass balance. Each arm of the assembly consists of a Omega LCAE-1KG load cell mounted on a machined aluminum plate beneath an upper balance arm which contacts the lysimeter and the load cell via ball bearings at equal distances from a pivot point. Counter weights made of lead are placed at the back of the balance arm to support and offset the columns mass. Load cell arms are placed at three points of contact around the lysimeter spaced 120 degrees apart. Omega LCAE-1KG load cells used have a measurement window of +/- 1 kilogram and function by measuring the voltage changes caused by deflection in a circuit resulting from applied load (Omega, 2017). The relationship between output voltage and mass in the lysimeter is linear and determined by calibration. Load cell data is recorded using a Campbell Scientific CR-6 Wi-Fi data logger which also directly provides power to the units.

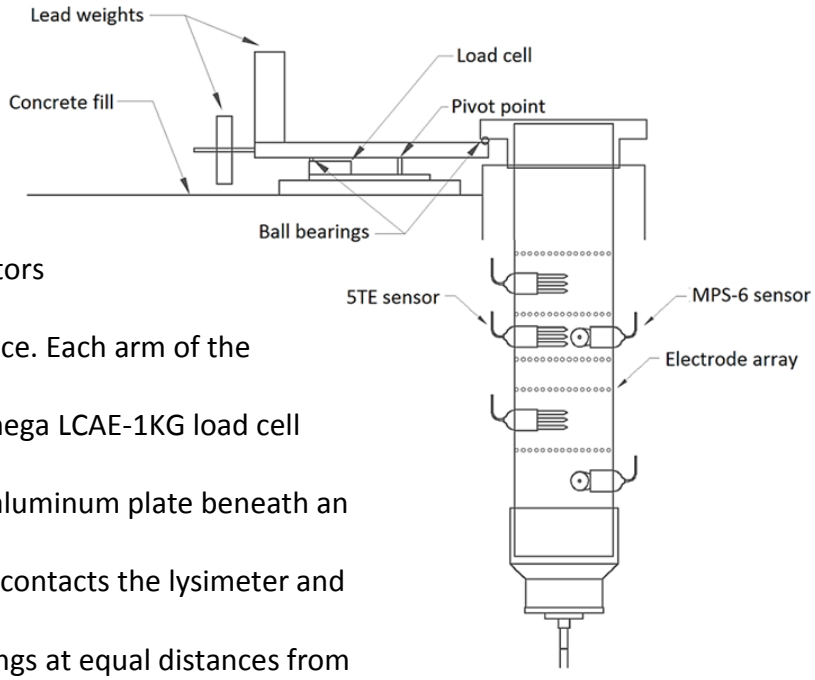

Figure 11: Design schematic of lysimeter column and one arm of load cell mounting system.

Three Decagon 5TE and two Decagon MPS-6 sensors are installed at different depths within each column to provide in situ hydrologic data on the soil moisture dynamics. Decagon 5TE sensors provide moisture, temperature and electrical conductivity data by measuring apparent dielectric permittivity using an oscillator running at 70 MHz which is converted to hydrologic parameters using a surface-mounted thermistor (Decagon Devices, 2017b). Matric potential is monitored by the Decagon MPS-6 sensors using a porous ceramic plate with a moisture release curve (Decagon Devices, 2017a). All Decagon sensors operate on SDI-12 protocol and data is recorded with a Decagon EM50 data logger.

Electrical resistivity arrays are installed at five depth levels in the lysimeter columns, where each array consists of 48 graphite electrodes. Electrodes are constructed with short graphite rods joined to wires of a DB-50 cable using conductive silver epoxy which are housed in a protective plastic cap. Electrode arrays are designed to be reconfigurable to allow collection of tomography or utilized to collect bulk ER measurements of the soil profile (Fig. 12). Each electrode tier functions as a circular ERT array to produce cross sectional resistivity surfaces or to monitor bulk ER where electrodes on tier 2 and 4 can be shorted together to function as two potential electrodes (*V*) and tier

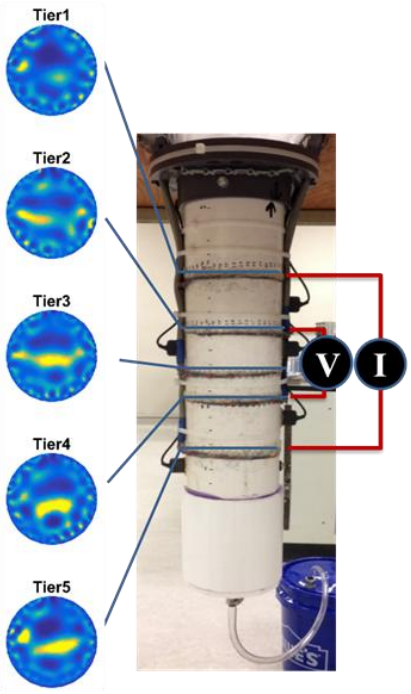

Figure 12: Lysimeter column LYS-1 and different ER array configurations.

1 and 5 can be shorted together to function as two current electrodes (*I*) as seen in figure 12. Additionally the column can be configured to monitor bulk resistivity quadripoles while simultaneously capturing tomography quadripoles in tier 3, but some resolution quality is sacrificed.

Lysimeter LYS-1 is the first lysimeter constructed and is packed with SRS sandy loam soil using 2-3 inch lifts with tamping in between layers to provide compression. The Decagon sensors which are installed into the LYS-1 column are model 5TM moisture probes and MPS-1 matric potential probes. Lysimeter LYS-2 is packed with SRS soil using the modified Proctor method (ASTM D-1557) with an initial VWC of 18 %. Layers with a thickness of 2 inches are added to the column before a 14.5 pound weight is dropped on the soil surface 10 consecutive times from a height of 2 feet. Estimated average soil bulk density after packing is 1.74 g/cm^3. Column LYS-2 was outfit with new 5TE moisture probes and MPS-6 matric potential probes (Appx. 5.2).

2.7 LYSIMETER COLUMN EXPERIMENTS

2.7.1 UNIFORM WETTING FRONT EXPERIMENT

To prepare for dynamic infiltration experiments in the lysimeter, a control experiment was performed to determine what the signature of uniform wetting front progression would look like from the perspective of each sensing method. Flow was injected from the bottom of the column to slowly saturate the soil profile at a constant

rate to minimize potential occurrence of preferential flow, and allow air to escape at the soil surface, thereby avoiding trapping in the pore space. For this uniform wetting experiment the upper boundary condition of the soil matrix was constant atmospheric pressure with no evaporation to simplify the water balance and allow porosity estimations.

The lower boundary was a constant applied head where hydraulic pressure gradient induces flow into the column (Appx. 5.3). Hydraulic head was maintained by attaching a vertical tube to the lower column and maintaining the water level in the tube at a set height above the lower soil boundary. The flux into the column at the lower boundary was estimated to be an average of 0.047 cm/min, where flow was slightly higher at the start and decreased as the hydraulic gradient lessened. Flow continued until free water was visible at the upper soil surface indicating the column had reached full saturation, at which time gravity drainage was initiated. Total inflow volume to saturate is 2.33 liters. Porosity was estimated to be 43%.

2.7.2 STEADY INFILTRATION EXPERIMENT

After establishing characteristic sensor responses to a uniform wetting front, a simple infiltration experiment was conducted. The objective was to monitor steady low intensity infiltration and drainage over a long period (12 hours) where flow through the soil matrix is likely to reach a steady state (Appx. 5.4). The initial condition of the soil

profile was near field capacity at only 24% saturated. The upper boundary of the lysimeter was open to the atmosphere and allowed free evaporation.

During the experiment a constant flux at a single drip irrigation point at the center of the column was applied to the soil surface. Thin nylon mesh was laid along the soil's upper surface to prevent physical displacement of the soil by droplet impact (Appx. 5.5). The lower boundary condition was a seepage face maintained at atmospheric pressure. Flow into the lysimeter was set to a rate of 10 mL/min for a period of 6.5 hours resulting in a total infiltration volume of 4 liters. After irrigation stopped effluent discharge was monitored and the column was left to dry by evaporation at the upper boundary.

2.7.3 RAINFALL SIMULATION EXPERIMENT

Multiple wetting and drying cycles were applied to lysimeter LYS-1, after which the soil in the column was observed to have compacted and slightly receded from the column walls at the upper soil surface (Appx. 5.1, 5.6). This settling of the soil matrix in the column may have developed preferential flow pathways which would affect flow behavior in the column. To take advantage of the macropores formed in the lysimeter, a rainfall simulation experiment was designed. Two 1.5 hour pulses of infiltration were applied to the column separated by a 12 hour period of drainage, evaporative drying and redistribution.

Upper boundary condition was constant flux at atmospheric pressure with the same irrigation configuration as the previous steady infiltration experiment. The upper soil surface remained open to free evaporation between irrigation events. Each wetting event had a flow rate of 8 mL/min or a flux of 0.055 cm/min for a duration of 1.5 hours. During each wetting event a total volume of 700 mL was infiltrated. The lower boundary condition is a seepage face at atmospheric pressure.

2.7.4 MACROPORE EXPERIMENT

Lastly, a final experiment was designed to emphasize the relationship between bulk electrical resistivity and the occurrence of preferential flow. A large 1 inch diameter artificial macropore structure was created in lysimeter column LYS-2 using a push rod core sampler (Fig. 13). The macropore was a 1 inch diameter hole offset from center and cored vertically from the upper surface to approximately half the soil depth (Appx. 5.7). Soil packed using the modified Proctor method (ASTM D-1557) had low permeability and flow through the macropore was dominant over infiltration through the soil matrix.

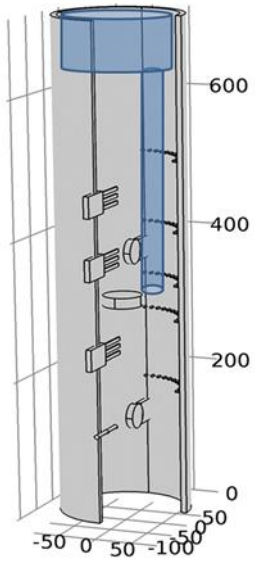

Figure 13: Representation of engineered macropore in lysimeter column LYS-2 where blue shading indicates airspace within the column.

Irrigation was again configured to drip in the center of the upper soil surface with an upper

boundary condition of a constant flux at atmospheric pressure and free evaporation. The flow rate was set to 8 mL/min or a flux of 0.055 cm/min at the upper surface for 1.5 hours, at which time ponding was observed at the upper surface and irrigation halted. Influent used was a solution of water and a blue tracer dye. The lower boundary condition was a seepage face at atmospheric pressure. Following irrigation the lysimeter was monitored during gravity drainage and the upper surface remained open to evaporation. After 7 days of drainage and redistribution the ponded water at the surface was suctioned out and the lysimeter was excavated in 1 inch layers. Excavation revealed the distribution of water throughout the soil profile at each depth interval (Appx. 5.8).

SECTION 3: RESULTS AND DISCUSSION

3.1 PHYSICAL SIMULATION

COMSOL Multiphysics simulations are used to evaluate the way apparent electrical resistivity behaves in a soil column during different flow scenarios (uniform front versus macroporous) with different electrode array geometries (horizontal versus vertical), and to evaluate anisotropy of apparent resistivity. Figure 14 shows how the electric field of a horizontal or vertical array becomes perturbed by interaction with a uniform wetting front. Alternatively, figure 15 presents an example of a horizontal and vertical array being perturbed by a fluid filled macropore structure. The changing electric field over time is characterized by the change in apparent resistivity measured between electrodes M and N in figures 14 and 15.

In the case of the horizontal electrode array with a uniform wetting front, the potential field begins to be altered at a depth of 5 cm as the wetting front comes within 3 cm of the electrode array (Fig. 16, A). As the front enters the region of the array, the apparent resistivity reduces quickly from 0.11 Ohm-cm to 0.02 Ohm-cm when it reaches a depth of 8 cm, then continues to reduce slowly as the front passes. Once the wetting front reaches a depth of 11 cm and has passed through the sensing region, apparent resistivity reaches a minimum of 0.01 Ohm-cm and the potential field reaches

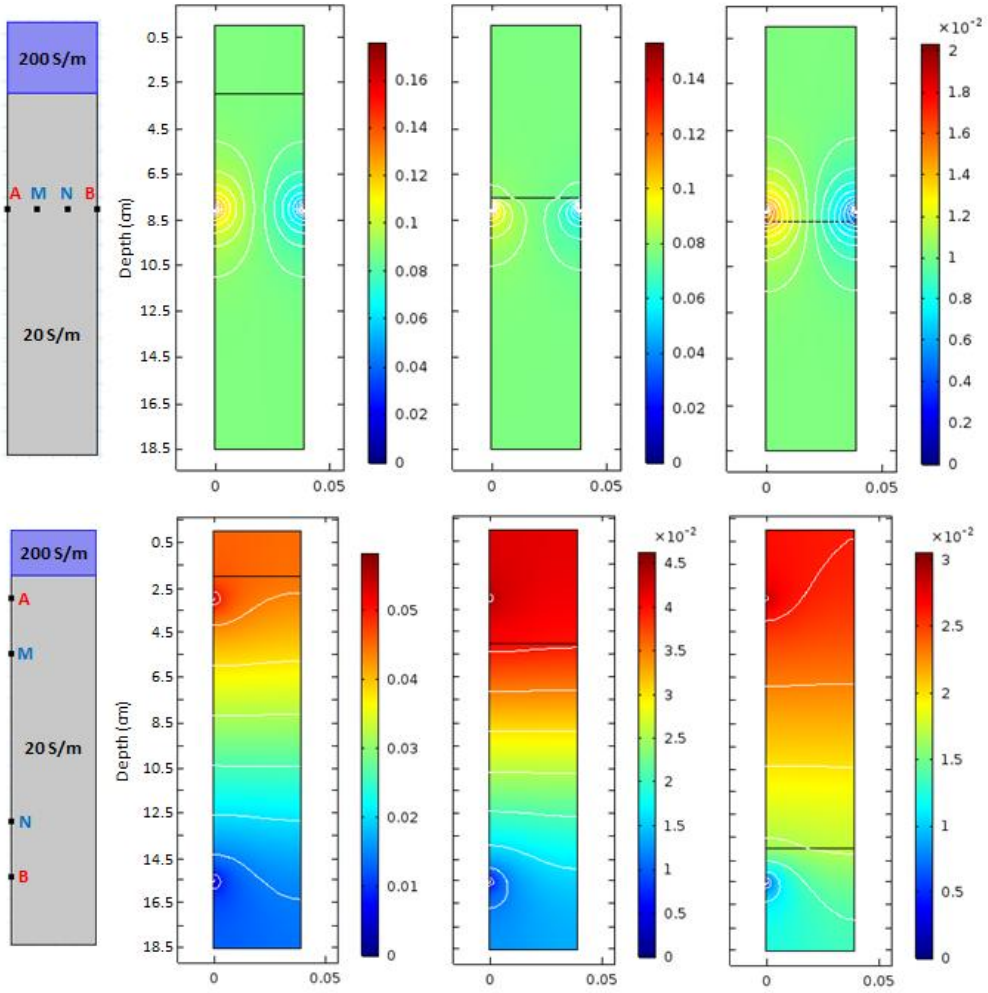

Figure 14: Simulation geometry of uniform wetting front with examples of undisturbed and disturbed electrical potential distributions for each array configuration. (Additional potential distributions see Appx. 1.2 and 1.3).

equilibrium. These results indicate the horizontal array is sensitive to wetting within the soil matrix up to 5 cm above the array depth. Once the area around the electrodes is wetted and the resistance to current flow is greatly reduced but current remains constant, apparent resistivity is thereby reduced. The effective resistance of the sensing region begins to reduce as wetting enters and continues wetting progresses through the array but when wetting is below the array the change is lesser as current is already

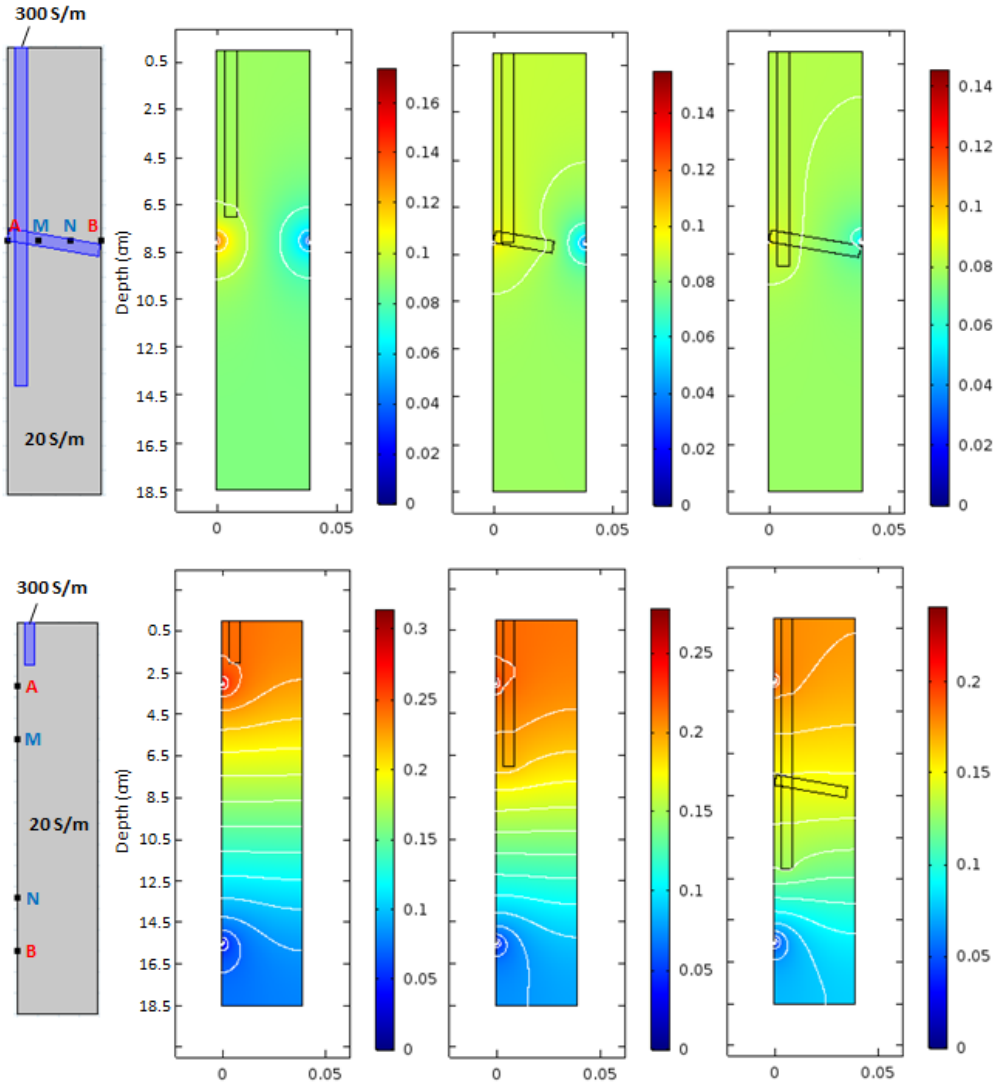

Figure 15: Simulation geometry of macroporous wetting through each array configuration with examples of undisturbed and disturbed electrical potential distributions. (Additional potential distributions see Appx 1.4 and 1.5)

preferentially flowing through the region of higher conductivity. Effective resistivity change with the progression of a uniform wetting front is behaving as an arithmetic average of resistivity along the vertical profile of the column.

When a uniform front passes through a vertical electrode array there is a slight response of 0.003 Ohm-cm when the front comes within 1 cm of current electrode A

and perturbs the potential field (Fig. 16, C, Appx. 1.3). Apparent resistivity remains constant until the wetted area bridges the region between current electrode A and potential electrode M. As the front progresses from potential electrode M at a depth of 5.5 cm to electrode N at 13 cm, apparent resistivity is steadily reduced from 0.277 Ohm-cm to 0.094 Ohm-cm. After the front passes the depth of electrode N, apparent resistivity remains constant.

With the scenario of macropore flow, there is a change in response characteristics for each of the array configurations. When wetting in the macropore comes within 2 cm of the horizontal array, there is an apparent resistivity response that

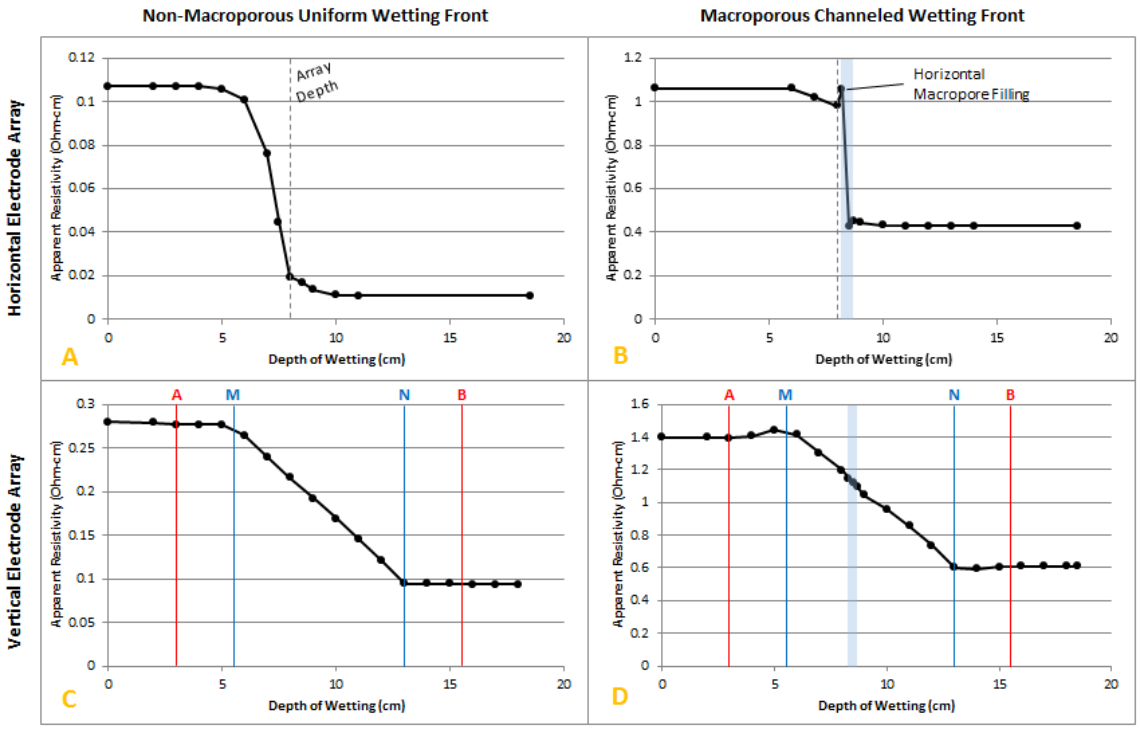

Figure 16: Apparent resistivity with depth for each simulated configuration. Horizontal array depth indicated by dashed line in plot A and B. The blue highlight in plot B and D indicates a period associated with filling in the horizontal portion of the macropore system.

steadily reduces from 1.06 Ohm-cm down to 0.98 Ohm-cm when wetting reaches the array depth of 8 cm (Fig. 16, B). Interestingly, there is an increase in apparent resistivity of 0.076 Ohm-cm as the horizontal section of the macropore begins to fill. This is immediately followed by a sharp decrease from 1.057 Ohm-cm down to 0.426 Ohm-cm as the horizontal flow bridges the space between potential electrodes (Fig. 17). There is another slight increase in apparent resistivity of 0.029 Ohm-cm once the wetted region extends from potential electrode N to current electrode B. Apparent resistivity decreases to equilibrium within 2 cm depth beyond the horizontal array. Effective resistivity change with macroporous wetting is behaving as a harmonic average of resistivity along the vertical profile of the column.

Finally, as macropore flow enters a vertical array there is also an initial reduction in apparent resistivity of 0.004 Ohm-cm as wetting approaches the current electrode A (Fig. 16, D). This is followed by an increase of 0.048 Ohm-cm as wetting progresses between electrode A and M. Once the wetted region is within 1 cm of potential electrode M, apparent resistivity begins reducing continuously from 1.44 Ohm-cm down to 0.60 Ohm-cm at electrode N. In this case there was minimal effect on the potential difference during the filling of the horizontal section. After the wetting front is 1 cm past electrode N, there is a slight increase in apparent resistivity of 0.018 Ohm-cm before reaching current electrode B after which point resistivity stabilizes.

The initial measured reduction in apparent resistivity as the wetted macropore nears the horizontal array is a result of the increasing effective conductivity in the system. The brief increase seen in apparent resistivity happens when the horizontal region of the macropore fills and bridges the space between current electrode A and potential electrode M (Fig. 17). Current density is higher within the macropore and if the local change in current was much greater than the change in effective resistivity, it could cause a local increase in potential and a sharper electric potential gradient between electrodes M and N.

Once the wetted area bridges the space between the two potential electrodes, electric potential rapidly drops when current is more evenly distributed across the array reducing the effective resistivity in the sensing region. If the macropore consisted of only the vertical section the response would likely be similar to the homogenous wetting case but with a higher magnitude of overall voltage. In that case the primary differentiation would likely be the velocity at which flow progressed through the system to provoke a response.

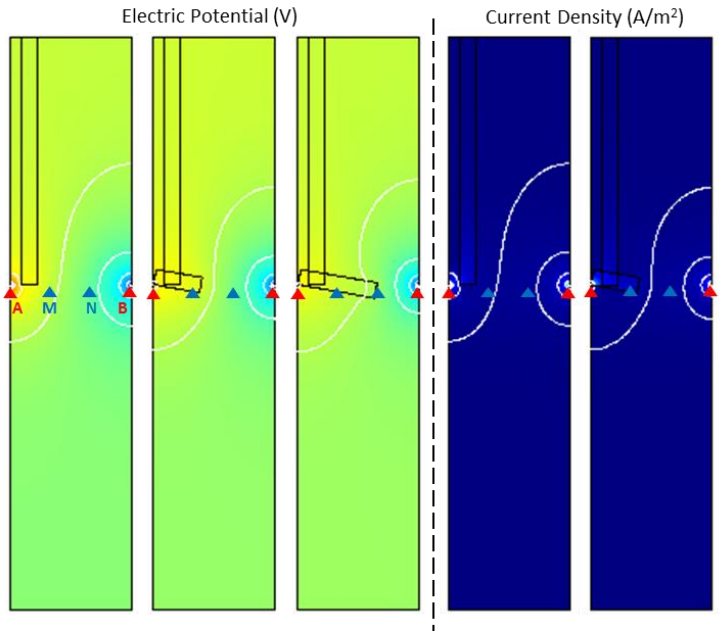

Figure 17: Simulation steps showing macropore geometry which caused a temporary resistivity increase as fluid filled the macropore near the horizontal electrode array. Additionally, current density in the system is shown. Electric potential contours indicated by white lines.

ER monitoring with a vertical array again shows an increase in apparent resistivity as wetting in the macropore approaches the first potential electrode. Simulation indicates that electric current preferentially flows through the more conductive macropore and that the electric potential field is distinctly perturbed by the macropore (Fig. 18). Equipotential lines here can be seen to conform tightly around the boundary of the macropore structure and potential gradient near the macropore increases.

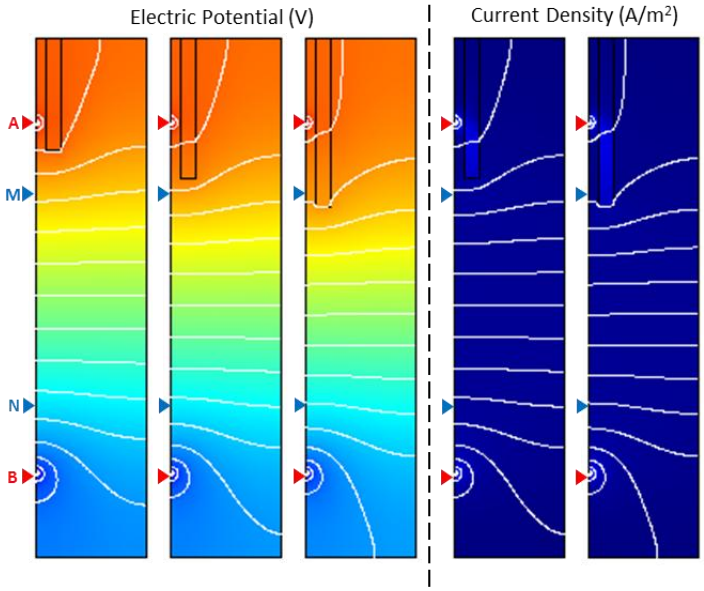

Figure 18: Simulation geometry which caused a temporary voltage increase as fluid filled the macropore between electrodes of the vertical array. Current density is shown to the right of the dashed divide.

The horizontal section of the macropore has minimal effect on the vertical potential distribution though initially some current disperses into the filled portion (Fig. 18). Once the macropore is filled through the lower portion of the column space, current flow effectively bypasses the horizontal wetted area. The greater effect the horizontal macropore section would have in this system is a transient one, where the filling of the horizontal section could retard vertical progression. Rate of reduction of apparent resistivity would temporarily slow and cause a plateau in the transient

monitoring data, an effect not seen in these stationary simulations which are presented in terms of wetting depth.

3.2 ARCHIE'S LAW CALIBRATION

Archie's law (Eqn. 3) calibration data is collected to determine the relationship between bulk electrical resistivity and degree of saturation for the SRS sandy loam soil. Observations made of prepared calibration samples yield a dataset which is used to fit equation 3 and find parameters a = 0.96, m = -1.19 and n = -1.57 (Fig. 19). There is less agreement of Archie's law to the observation points at the lowest saturations. This could be caused by measurement error of the IRIS SYSCAL-Pro ER meter for which error

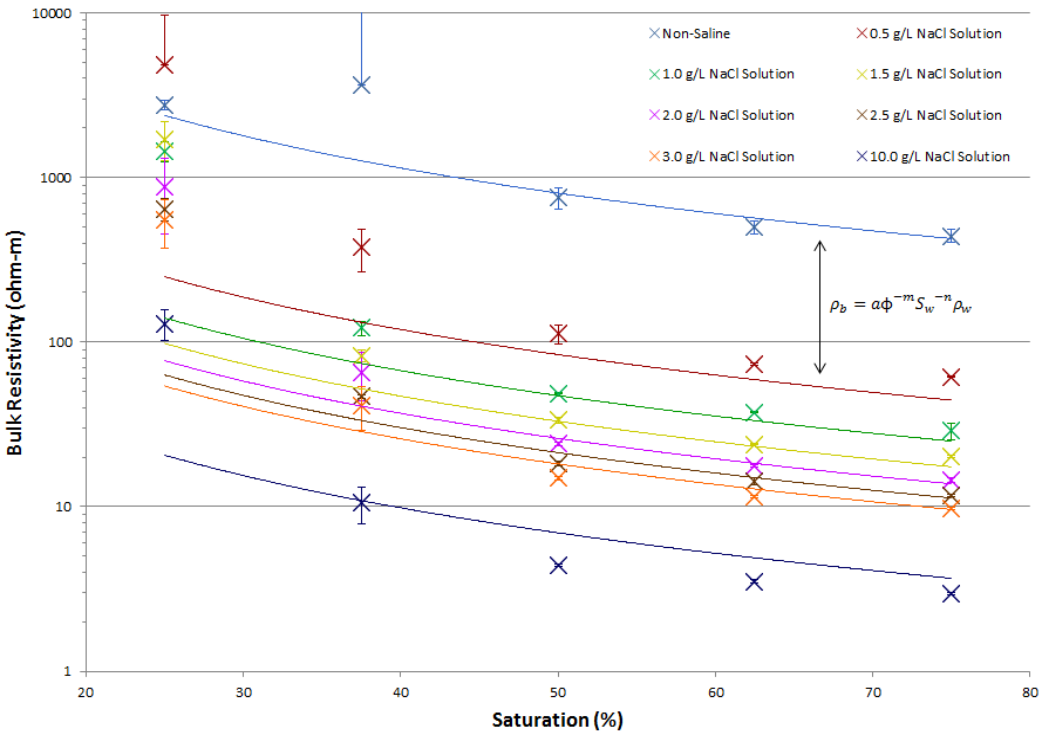

Figure 19: Observations of Archie's law calibration samples. Best fitment of equation 3 shown as lines.

testing indicated a greater error associated with high resistance (Appx. 3.3). Additionally, samples prepared at the lowest saturation (25%) are more difficult to prepare at the same bulk density as the samples at higher saturations. Samples at 25% saturation tended to be approximately 0.5 g/cm^3 lower density, which likely would affect some parameters in equation 3.

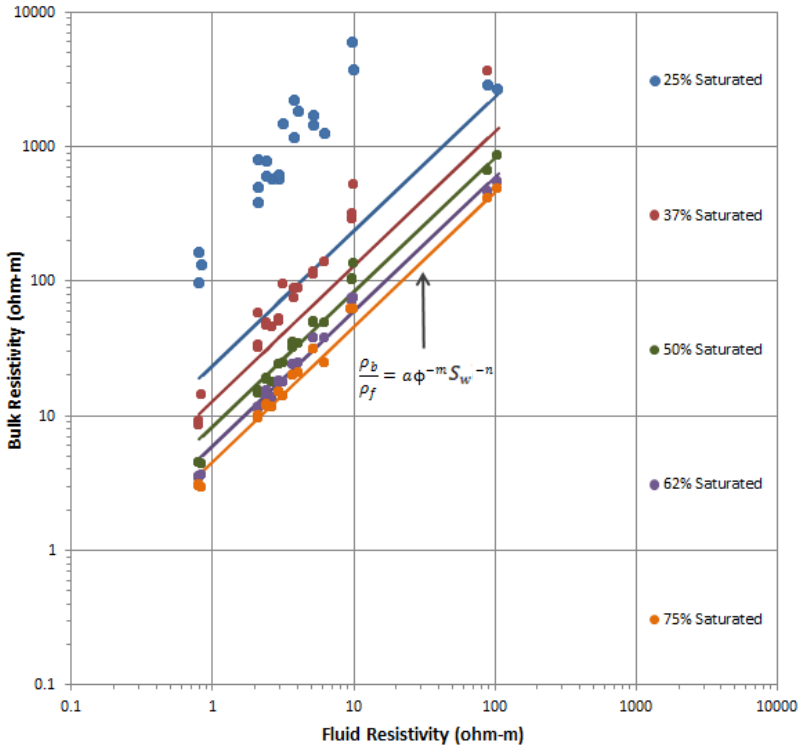

Figure 20: Bulk resistivity relates to fluid resistivity with a slope of 1, where the intercept would be the formation factor *F*.

Plotting measured bulk electrical resistivity of soil samples versus the resistivity of fluid used in each prepared sample illustrates the relationship described in equation 5, where intercept of formation factor *F* is a function of saturation (Fig. 20). Samples of 25% saturation are again offset from the calibration lines shown. This may also be an

influence of surface conductivity, an effect which has greater impact at lower saturations. Li et al. (2015) found that fluid films within the pore space which influence surface conductivity caused divergence from simple power law when plotting formation factor *F*.

3.3 CT IMAGING COLUMN EXPERIMENTS

3.3.1 COLUMN CT1 HOMOGENOUS EXPERIMENT

The first CT column experiment conducted uses the homogenous column CT1. X-ray scans of the column after packing indicate some density interfaces were produced between layers with bulk density decreasing upward (Fig. 21). This column was packed in lifts using a drop weight to compact each layer and achieve optimum soil density to prevent cracking and maintain homogeneity. A horizontal crack was observed to have formed at electrode tier 6 (Fig. 21, C). Image processing of CT scans is unfortunately hindered by the use of steel electrodes which attenuated the X-rays and produced image artifacts (Appx. 4.3). As a result, calculation of water content distribution is not feasible and processing reverted to threshold image differencing to represent qualitatively the spatial distribution of water.

Infiltration into the column begins at time zero and flow is monitored continuously using ER and CT imagery. Progression of the wetting front is initially uniform, however just prior to 5 hours into the experiment finger flow begins to develop

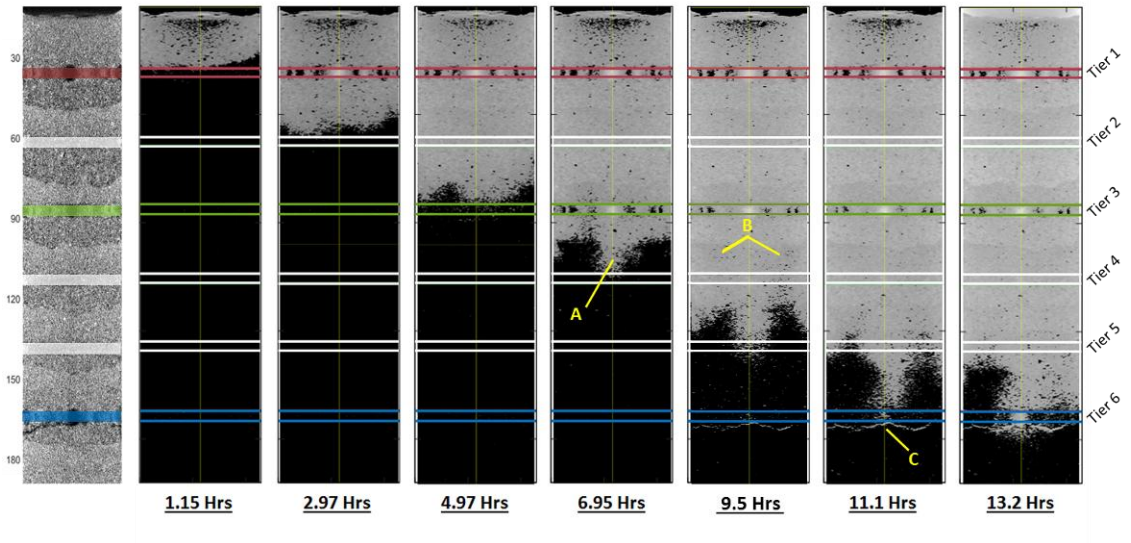

Figure 21: Vertical cross-sections of homogenous CT column CT1 during infiltration. Black areas are where dry soil was subtracted from the image, grey areas show distribution of fluid in the pore space. (Adapted from Mamun)

as the wetting front passes electrode tier 3 (Fig. 21, A). The length of the fingering continues to grow over the next 6 hours and by 11.1 hours into the experiment the soil matrix is seen to be dry along the column walls between tiers 5 and 6. Interaction with the horizontal crack at tier 6 begins by 9.5 hours and by 13.2 hours the crack appears to be saturated and flow does not progress past that point (Fig. 21, C).

For each imaging time, the depth of the wetting front was estimated for each wet/dry differenced CT image by selecting an isolation point from its bimodal histogram to use as a threshold value in determining the wetting front location. The mean and variance in the depth of the wetting front were then determined and plotted as a function of time (Fig. 22). The mean wetting front progresses at an almost constant rate through the first 11 hours of the experiment, after which it no longer advances.

From the onset of infiltration until after 4 hours into the experiment the variance of the wetting front position is low, indicative of a uniform wetting front. At about 3 hours into the experiment, the advance of the wetting front slows slightly. After 4 hours the variance of the wetting front position across the column increases, consistent with the initial formation of the finger. Around 7.5 hours the wetting front slows and variance increases substantially as the finger penetrates deeper. Between 9 and 11 hours the shape of the finger appears stable in the CT images (Fig. 21) and the mean advance of the wetting front is approximately constant at a rate equivalent to the first three hours of the experiment (Fig. 22). About 11 hours into the experiment, the mean wetting front slows and the variance of the front position grows as the finger intercepts and fills the crack at the bottom of the column (Fig. 21).

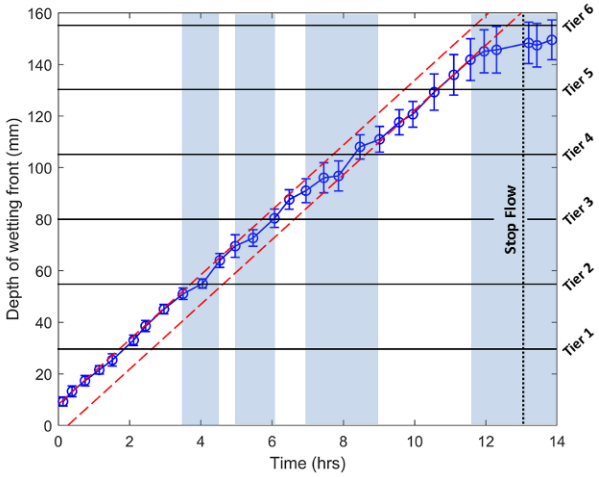

Figure 22: Wetting front progression in CT1. Vertical bars on points indicate spatial variance at the front. Red dashed lines highlight initial rate. Blue shading indicates deviation from initial rate.

Bulk electrical resistivity measurements are taken in the upper, middle and lower regions of the column as well as averaged across the entire column (Fig. 23). Upper bulk resistivity is first to reduce as the wetting front passes the current electrode A at tier 1. As the wetting front approaches tier 3 or potential electrode N, apparent resistivity reduces to its minimum and remains unchanged for the duration of the experiment.

Middle bulk resistivity responds after 2 hours of infiltration as the front nears the array's current electrode A at tier 2. Lower bulk resistivity responds as the wetting front nears tier 3 at around 4 hours. The total bulk resistivity begins to respond simultaneously with the upper bulk response and resistivity measured continues to decline steadily until 7 hours.

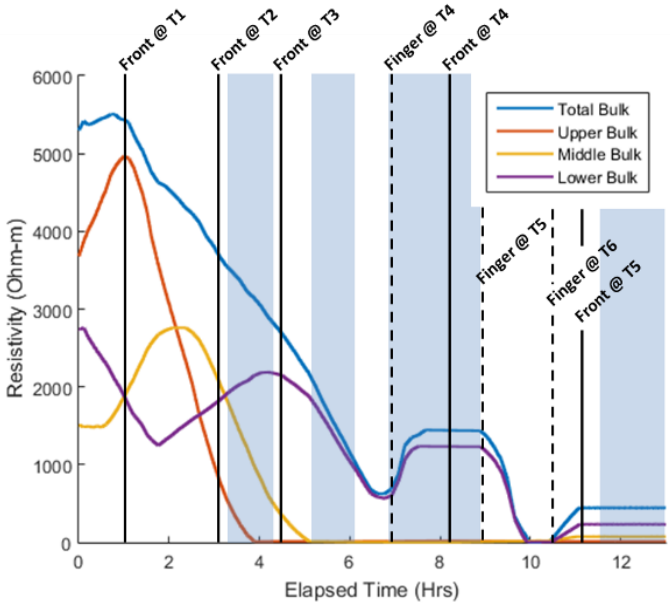

Figure 23: Vertical bulk electrical resistivity monitoring during infiltration into CT1 column.

Initial responses (maxima peaks) of upper, middle and lower bulk resistivity to the wetting front all occur approximately 1.5 hours apart and reduction follows nearly the same rates on all three sensing regions. Initial responses near corresponding A electrodes is a consistent trend seen in simulations as the effective resistivity in the sensing region begins to reduce. The response times observed are an indication that the wetting front was progressing at roughly a constant rate for the first 6-7 hours, which is reinforced by wetting front analysis (Fig. 22). After 5 hours of irrigation the finger begins to form at the wetting front and by 6.5 hours the finger penetrates down to tier 4 and the lower and total bulk resistivity signals begin to increase as water moves down with the finger and water content behind the front decreases temporarily causing an

increase in effective resistivity (Fig. 21, A). Tier 4 is where the first potential electrode M is for the lower bulk array, and this could be a similar effect as seen in simulations where potential difference increased slightly as the macropore moved between electrode A and M (Fig. 16, D).

However, the behavior from 6.5 to 7 hours is also shared with the total bulk ER array, which does not use electrodes at tier 4. One possible explanation is that air is being displaced by solution in the pore space and as the finger progresses downward, air is simultaneously moving upward around it. This rising air would reduce water content by displacing pore water behind the wetting front, thereby increasing the effective resistivity of the soil matrix in the column. Similar observations were made in a study on flow instability as a result of air entrapment by Wang, et al. (1998). CT imagery shows some indication that this may be occurring (Fig. 21, B) as regions of black voxels indicating lower water content can be seen flanking the sides of the finger above tier4. At 7 hours a similar feature is also visible on the upper left side of the finger marked 'A' near tier 3.

The reasoning behind this is that the lower boundary of the column has a porous ceramic plate for which air could not overcome the entry pressure. Air pressure in the column is likely increasing continuously as the wetting front progresses downward trapping and compressing air in the lower column until pressure builds enough to begin displacing fluid from pore space above and causing flow instability (Wang, 1998). This

concept is additionally supported by a pressure release which occurred in the column after the upper cap was removed (Appx. 4.4).

Between 7 and 9 hours in the experiment total and lower bulk resistivity plateaus (Fig. 23) while the wetting front slows down as the finger elongates, then at 8 hours the front surges forward and by 9 hours resumes its initial velocity (Fig. 22). This slowdown again a likely result of air pressure holding the fluid back until a critical point when it redistributes upward into the matrix and wetting surges forward with the reduced pressure. After 9 hours the finger reaches tier 5 where potential electrode N is shared by both total and lower bulk arrays, and by 10 hours all vertical resistivity is reduced as the finger reaches the lower current electrodes at tier 6 and bridges connectivity between all vertical arrays.

Electrical resistivity monitored across horizontal planes at tier 1, 3 and 6 had similar responses to the wetting front progression in the column (Fig. 24). Resistivity is relatively stable at all horizontal tiers until the wetting front enters the sensing region of each array.

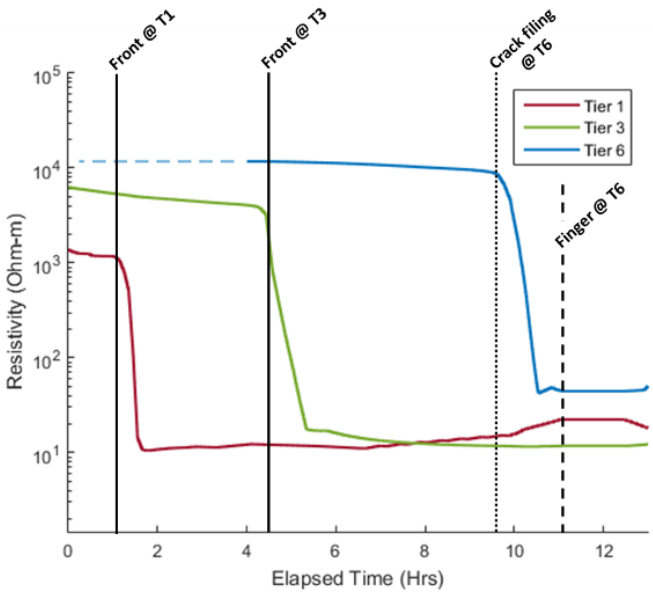

Figure 24: ER monitoring at horizontal electrode tiers during infiltration into CT1 column.

Resistivity at tier 1 reduces rapidly between 1 and 1.5 hours as the front passes through its horizontal plane as a uniform front. Apparent resistivity at tier 3 begins to reduce as the wetting front approaches, however the reduction here takes twice as long from 4.5 to 5.5 hours. This slower rate correlates with the onset of finger flow at that time and location (Fig. 22) causing the local effective resistivity to reduce more slowly. The reduction in front velocity after 7 hours is reflected by the late arrival time of the resistivity reduction at tier 6, which reduces at the same time as the horizontal crack at tier 6 saturates and increases connectivity within the array (Appx. 4.5).

In order to better compare these data and other experimental data as well as simulations, the resistivity responses are normalized from a time axis of experiment duration to an axis of estimated wetting front depth. Time is converted to estimated depth by considering the known volumetric flow rate of the irrigation pump and the porosity and initial water content of the soil (Eqn. 8).

$$d_f = \frac{t \cdot j}{\phi - \theta_i} \qquad \text{(Equation 8)}$$

Where d_f is depth of front (cm), t is time (min), j is flux (cm/min), ϕ is porosity and Θ_i is initial water content.

When normalized from time to associated estimated wetting depth, some interesting trends become apparent. Horizontal tiers respond to wetting approximately 1 cm above each array plane (Fig. 26). The response behavior from each horizontal tier

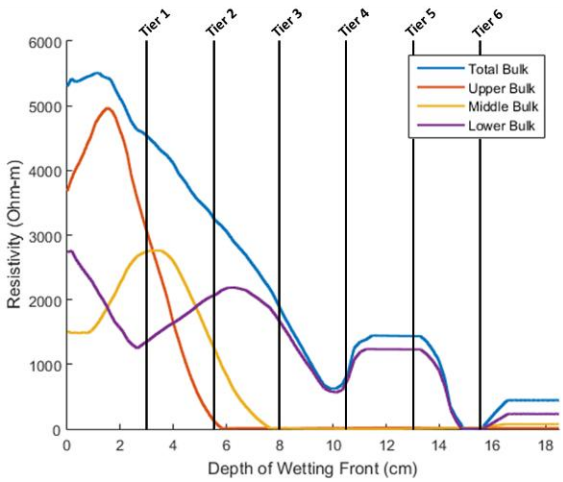

Figure 25: Vertical bulk electrical resistivity normalized to estimated depth of wetting front from soil surface.

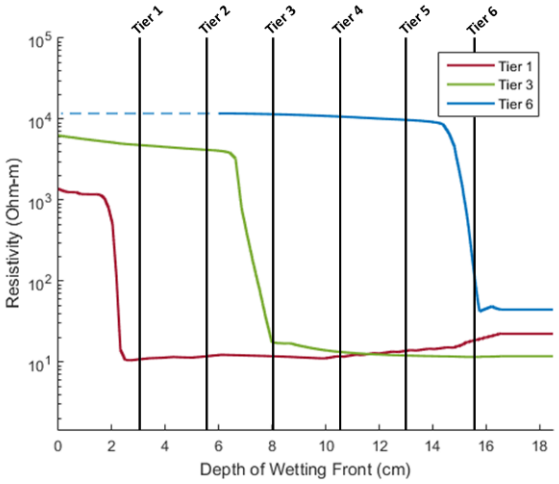

Figure 26: Horizontal resistivity normalized to estimated depth of wetting front.

is in good agreement with the results of simulating a uniform wetting front passing through a horizontal array (Fig. 16, A). Comparing horizontal and vertical responses, there is alignment between estimated wetting front depths and the depths that responses are expected from the vertical and horizontal arrays.

Figure 27 shows calculated anisotropy of the vertical and horizontal apparent resistivity responses to uniform wetting in this experiment. In the upper column, horizontal resistivity reduces nearly independently as the wetting front

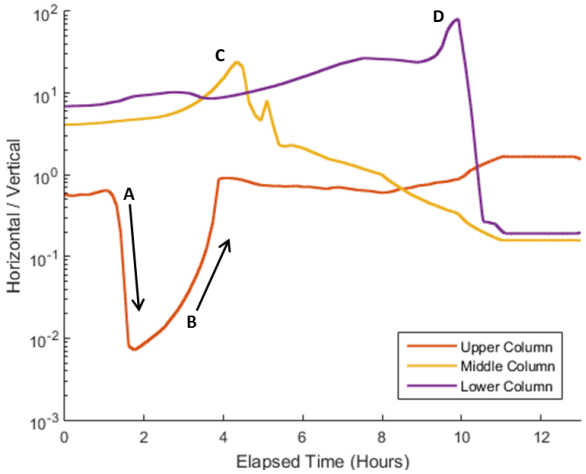

Figure 27: Calculated anisotropy of column CT1 vertical and horizontal resistivity.

passes through the tier 1 electrode array (Fig. 27, A), but then as flow penetrates downward, vertical resistivity begins to reduce as wetting increases between potential electrodes (Fig. 27, B). Anisotropy in the middle column shows a positive peak between 4 and 5 hours (Fig. 27, C), which corresponds with time and depth that the finger was initially developing at the wetting front (Fig. 22). Similarly in the lower column there is a positive peak observed at 9.5 hours (Fig. 27, D), at which time the horizontal crack at tier 6 is seen to be filling in the CT data (Fig. 21). Both orientations show reducing resistivity between 5 and 11 hours (Fig. 27, C), but downward slope indicates change in the horizontal direction is greater.

3.2.2 COLUMN CT2 MACROPOROUS EXPERIMENT

Following the homogenous experiment with CT1, infiltration into heterogeneous column CT2 was monitored (Fig. 28). Because graphite electrodes were used in this CT2 column, CT data from this experiment was able to be processed to provide the spatial distributions of water content as well as quantify degree of saturation of each voxel. Infiltration begins and wetting progresses as a thin layer at the upper surface which flows downward as a film of fluid into the macropore channel. Vertical cross sections show flow along the macropore walls for the first 3.5 hours, where fluid is infiltrating downward from the surface at the same time it can be seen in figure 27, point A, imbibing into the soil matrix from the macropore. By the time 5 hours has past, there is a higher degree of saturation locally surrounding the upper vertical portion of the

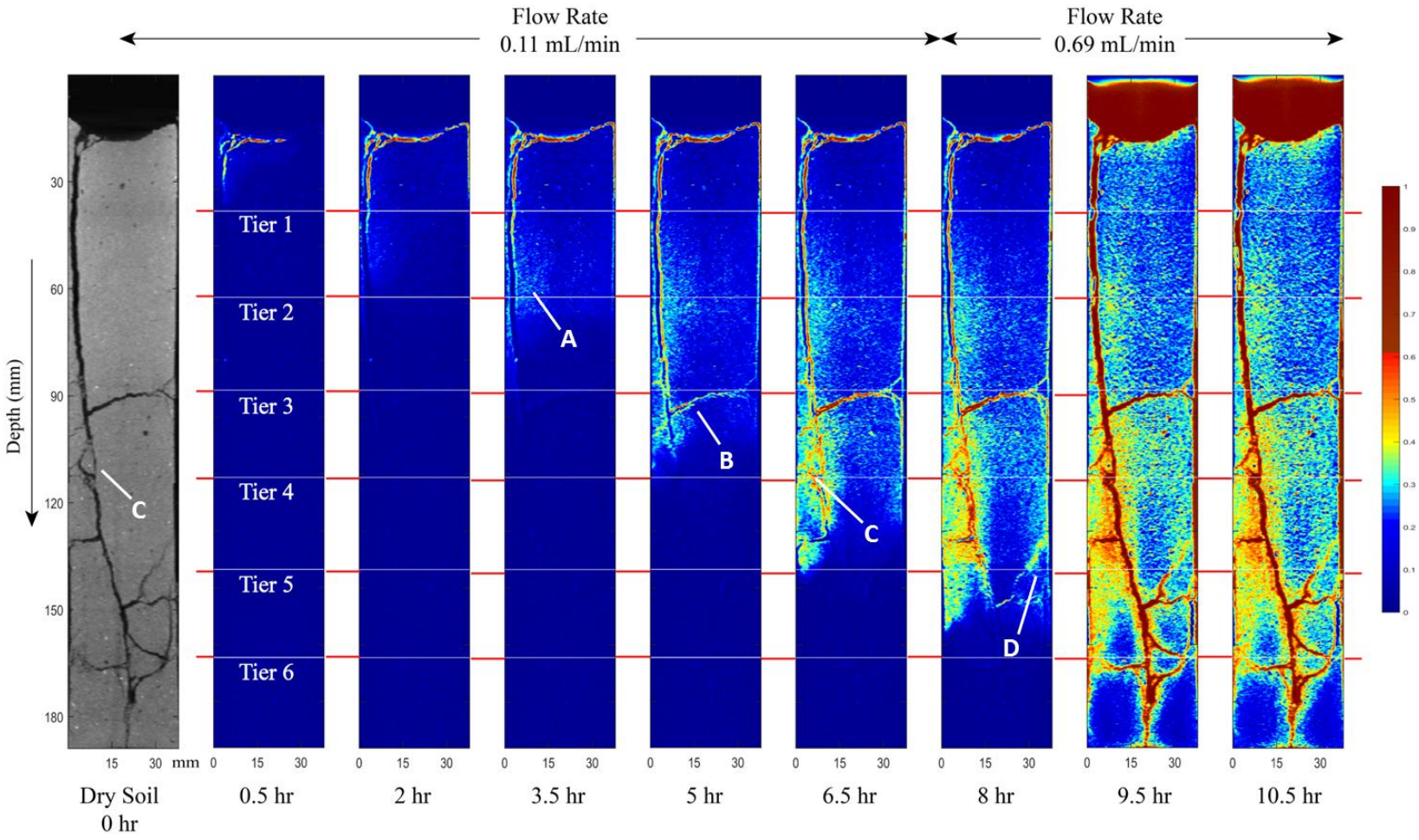

Figure 28: Vertical cross-sections of water content in column CT2 experiment. Color scale indicates degree of saturation from 0 (blue) to 1 (red). X-ray cross section to left shows structure of macropore network in black within gray soil matrix. (Adapted from Mamun)

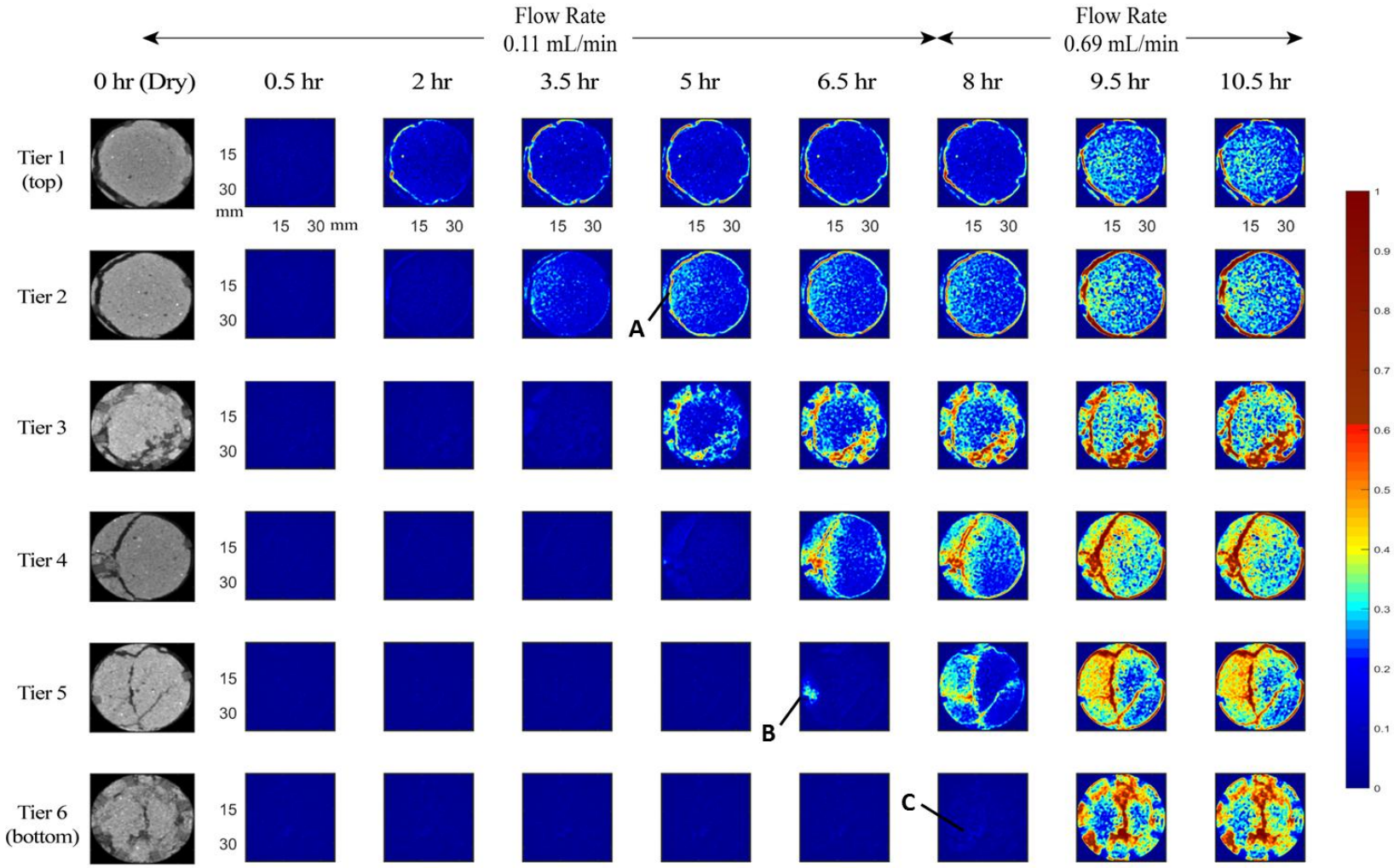

Figure 29: Horizontal cross-sections of column CT2 during infiltration. Horizontal planes at each electrode tier are depicted through time. Color scale represents saturation. X-ray images on left show soil matrix and crack network as well as tips of electrodes. (Adapted from Mamun)

macropore and fluid is accumulating in the horizontal crack at tier 3 (Fig. 28, B).

The macropore structure between tier 3 and tier 4 is fragmented and less of an open channel as above (Fig. 28, C). By 6.5 hours this macropore region beneath the horizontal crack is facilitating imbibition into the soil matrix proximal to the macropore and preferential wetting on the left side of the column. After 8 hours of irrigation the flow rate is increased and the macropore network saturates completely as fluid ponds at the upper surface of the soil. It is apparent from horizontal cross-sectional images that near the end of the experiment, the lower half of the column is more saturated than the region above tier 3 (Fig. 29). Additionally, the distribution of fluid above tier 5 is preferentially to the left side of the column in and around the primary macropore channel.

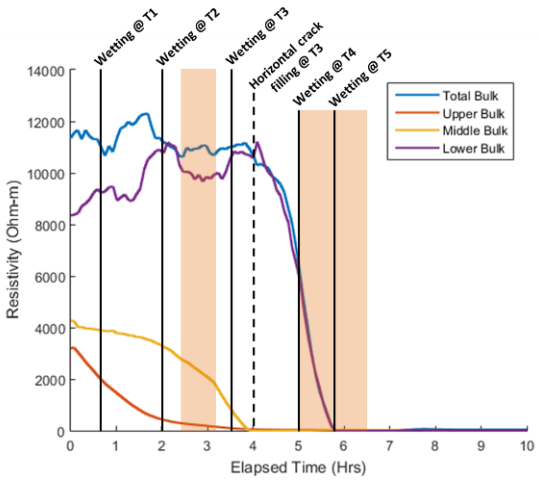

Figure 30: Vertical bulk ER measurements during infiltration of column CT2. Orange shading indicates periods of local matrix wetting and slowed progression in the macropore.

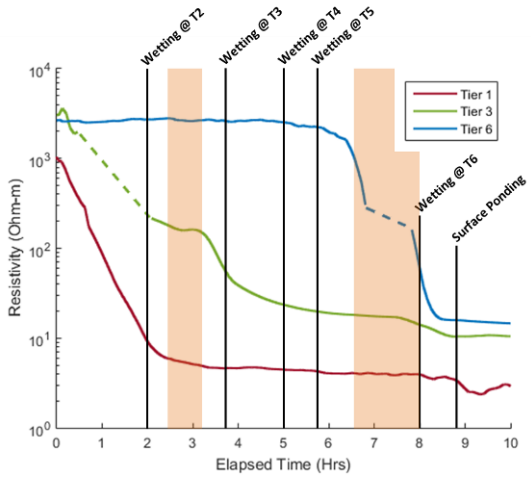

Figure 31: Horizontal tier ER measurements during infiltration of column CT2. Dashed portions of data are interpolated as a result of large error and signal noise.

Bulk electrical resistivity response to infiltration in this heterogeneous column differs from the homogenous column results (Fig. 30). As flow enters the column, upper bulk ER begins to reduce within minutes and continues to steadily decline for 2 hours until wetting reaches tier 2. After 2 hours, upper bulk ER reduces gradually as more fluid is imbibed into the soil matrix near the macropore (Fig. 28, A). Middle bulk ER begins to reduce very slowly from early time, then around 2 hours the rate increases as wetting reaches current electrode A at tier 2. By 4 hours time, the horizontal crack shown in figure 28, point B, is beginning to fill at which point the upper and middle bulk resistivity reaches a minimum.

Interestingly, lower and total bulk ER behaves quite similarly throughout infiltration showing a fair amount of variation in early measurements. After the crack at tier 3 begins filling, the signals begin to decline simultaneously. At 5 hours the signals merge and follow the same pathway through a period of matrix wetting and limited downward macropore flow seen around the structural feature at point C in figure 28. The similar behavior of lower and total bulk resistivity arrays seen in both the homogeneous and macroporous experiments is likely a result of the shared potential electrode N and current electrode B as well as the array sensing regions being very similar. Once wetting reaches the depth of tier 5 at around 6 hours, all vertical resistivity signals are fully reduced and remain as such for the remainder of the experiment.

Horizontal ER measured at tier 1 begins to reduce within minutes as well and steadily declines over the course of 2 hours, after which it continues to reduce slightly until reaching a minimum at 9 hours (Fig. 31). Tier 3 ER had some response that started to decline early on but was interrupted by high noise and error before stabilizing around 2 hours. Once measurements stabilize, resistivity is seen to have reduced by about 1700 Ohm-m since noise began at 30 minutes. Tier 3 ER reduces from 2-2.75 hours but then stalls for about 30 minutes before hastening to decline steadily for an hour during which tier 3 is seen to be wetting (Fig. 28). This steady decline in apparent resistivity at tier 1 and 3 is a result of the gradual increase in effective conductivity in the upper column as infiltration channels down through the macropore and imbibition begins to occur within the soil matrix.

Resistivity of tier 6 remains fairly constant for the first 5 hours before reducing slowly as wetting reaches tier 4. By 6.5 hours, ER at tier 6 begins to drop rapidly as the wetting front passes through tier 5 (Fig. 29, B). Shortly after, measurements have a period of high error during which resistivity only declines by about 150 Ohm-m. This stall in tier 6 resistivity is likely related to the period of slowed macropore advancement as matrix around the structural feature shown in figure 28, point C, continues to wet. By 7.7 hours there is still minimal wetting at tier 6 (Fig. 29, C) but once the flow rate is increased and the macropore begins to fully saturate, filling additional cracks in the network (Fig. 28, D) resistivity begins to reduce rapidly. This flooding in the macropore

elicits a response from tier 3 as well, and once ponding begins at the surface, tier 1 shows an additional reduction as the upper soil matrix increases in saturation.

When looking at vertical and horizontal resistivity normalized to a depth axis it is apparent that resistivity reduces more rapidly in this heterogeneous column than in the homogeneous experiment. Vertical resistivity in the upper column responds very rapidly and when wetting is estimated to be arriving at tier 2, the upper and middle bulk resistivity is reduced to nearly zero (Fig. 32). Lower and total bulk resistivity is completely reduced by an estimated wetting depth of 8 cm or the location of tier 3. Horizontal resistivity measured at tier 1 changes rate of reduction or reaches the apex of its curve right around the depth of tier 1 (Fig. 33, A). The apex of reduction of tier 3 resistivity occurs at an estimated wetting depth of 5.4 cm or just before the depth of

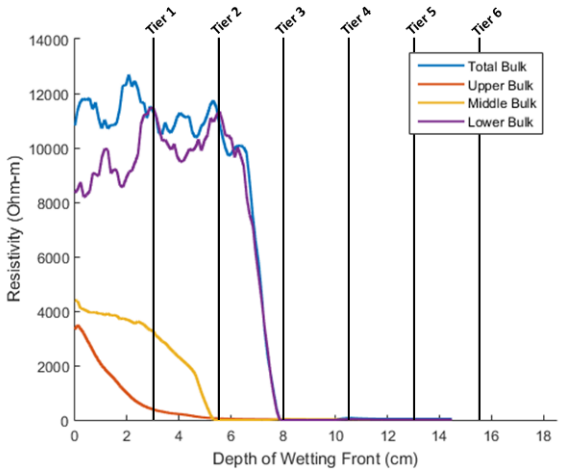

Figure 32: Vertical bulk ER normalized to estimated depth of wetting front relative to upper soil surface.

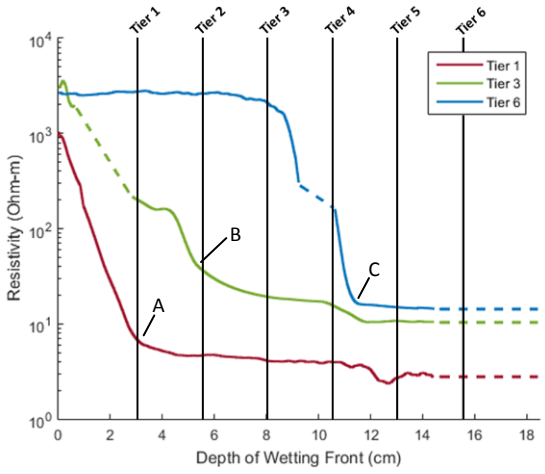

Figure 33: Horizontal ER normalized to the estimated depth of wetting front relative to upper soil surface.

tier 2 (Fig. 33, B). Resistivity measured at tier 6 is fully reduced by an estimated wetting depth of 11.5 cm where the apex of reduction is sharper than tier 1 and 3 (Fig. 33, C).

Anisotropy of apparent resistivity response to macropore wetting is different than in the case of a uniform front. In this case, in the upper and middle region of the column, vertical and horizontal resistivity are both reducing slowly (Fig. 34, A'). This is due to flow penetrating downward in the macropore while some fluid is also imbibing into the matrix near tier 1 (Fig. 28). Just after 3.5 hours the anisotropy of the middle column increases sharply as vertical apparent resistivity begins to reduce more rapidly as the area between the middle bulk array current and potential electrode is wetted (Fig. 34, B'). Then by 5 hours, the horizontal crack at tier 3 is wetting (Fig. 28, B) which causes a rapid reduction in horizontal apparent resistivity thereby reducing anisotropy in the middle of the column (Fig. 34, C').

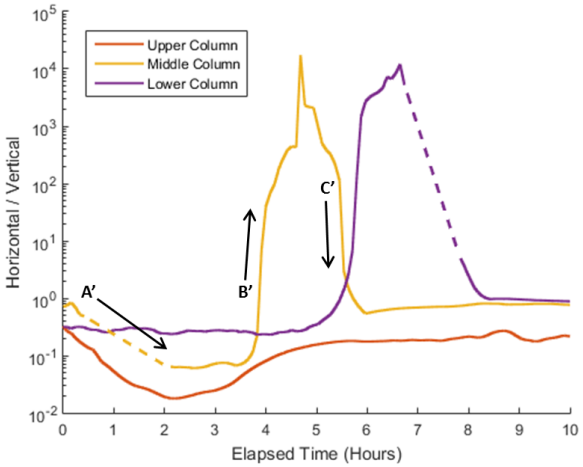

Figure 34: Anisotropy of vertical and horizontal resistivity measurements

Again a sharp positive anisotropy peak is seen around 6.5 hours in the lower part of the column. The increase in lower column anisotropy beings at 5 hours when vertical resistivity is seen to be decreasing rapidly due to wetting at the lower bulk array

potential electrode M which continues to flood the area between potential electrodes shortly after (Fig. 28, C). Wetting is then reaching the depth of tier 6 by 8 hours by which time horizontal resistivity and anisotropy is reduced. Consistently, peaks in anisotropy data indicate some form of preferential flow; finger flow in the CT1 experiment and macropore filling in this CT2 experiment.

Simulation of horizontal ER in a homogeneous system shows a curve profile that drops fairly rapidly and has an apex in the reduction at the array depth (Fig. 16, A). The horizontal results here show a more gradual drop in resistivity than was simulated in the macroporous system, but the vertical resistivity results show change much sharper than the simulation. This is surely a result of the complexity in the true system versus the simple simulation geometry. In this case there is spatially variable matrix wetting, complex macropore network with variable saturations, and three dimensional space. Effective resistivity reduces when wetting in the macropore creates connectivity within the sensing region, but is further reduced by imbibition into the soil matrix.

Comparing these results from the macroporous column experiment to the results of the homogeneous column experiment there are some distinct differences. Vertical bulk resistivity in the CT1 column responded with nearly equal rates of resistivity reduction where as in column CT2, responses all have different reduction profiles and are minimized at earlier times. Horizontal resistivity in column CT1 is reduced sharply as the wetting front passes through each electrode array, but here in

CT2 reduction at tier 1 and 3 is more gradual as the effective resistivity in the sensing region of the array is reduced. Early responses in column CT2 indicate that as fluid was transmitted through the macropore network in the column, connectivity between electrodes increased quickly as wetting progressed to greater depths more rapidly. Note that the wetting front reaches tier 3 through the macropore in column CT2 by 3.5 hours (Fig. 28) but not until 5 hours in column CT1 (Fig. 21).

Generally, both CT experiments indicate resistivity monitoring is sensitive to changes in flow, for example the resistivity response to the formation of the finger in CT1 or the period in CT2 where fluid was imbibing into the matrix more than progressing deeper through the macropore. Apparent resistivity response to the mostly uniform wetting front in CT1 was gradual vertically and sharp horizontally, similar to results of the uniform wetting simulations. In contrast the response to macropore flow seen in CT2 was sharper in the vertical array orientation and more gradual horizontally. This results from the dynamics of effective resistivity changes in time with different character of wetting. Prevalent indicators of preferential flow would then be response times which are earlier than predicted as well as sharp changes in vertical apparent resistivity indicating rapid change in connectivity within a measurement region. Additionally, positive peaks in horizontal to vertical calculated anisotropy are observed to occur at of preferential flow events in both CT column experiments.

3.4 LYSIMETER COLUMN EXPERIMENTS

3.4.1: UNIFORM WETTING EXPERIMENT

Increasing to a larger scale soil system, a series of experiments are conducted with lysimeters that mimic field conditions while still maintaining some control and sensing ability. The first experiment was conducted by injecting flow from the bottom of the lysimeter, thereby minimizing opportunities for preferential flow and maintaining a uniform wetting front. Bulk electrical resistivity in the lysimeters is converted to apparent saturation using Archie's law (Eqn. 3) for direct comparison to saturation measured by the moisture probes and load cells.

As the wetting front rises up from the bottom of the column, the lower moisture probe begins to respond first and shows an increase from 42% to 73% saturated over the course of an hour (Fig. 35). Bulk electrical resistivity begins to respond early as well and indicates increasing saturation at a slightly slower rate than the lower moisture probe but roughly equals the rate of all other sensors. Resistivity shows an initial apparent saturation of 44% and rises to 74% when the column is filled.

The middle moisture probe at 25 cm depth begins to interact with the wetting front after about 45 minutes and reaches a peak saturation of 68% at the 4 hour mark as well. Last to respond is the upper moisture probe at 16 cm depth after about 80 minutes of flow. Bulk ER and the moisture probes share a maximum peak at 240 minutes, at

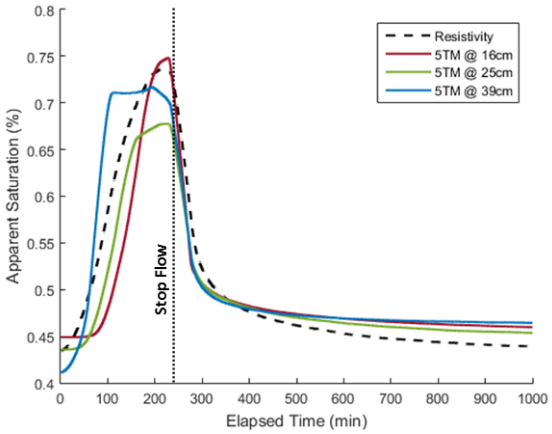

Figure 35: 5TM moisture probe and vertical bulk electrical resistivity data.

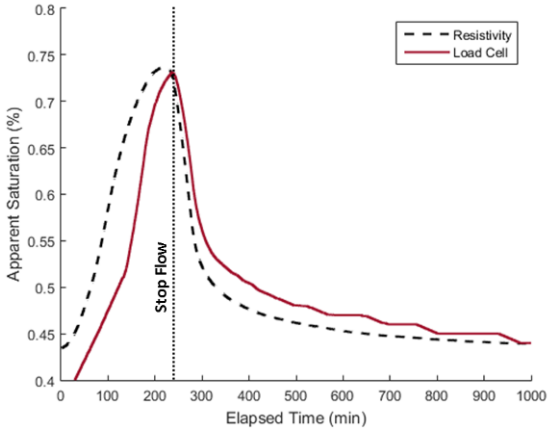

Figure 36: Load cell mass balance data along with bulk ER data.

which time water was observed ponding at the upper soil surface and flow was stopped and drainage was initiated. Mass balance measured by the load cells in the column begins to increase at time 0 when injection starts and apparent saturation changes from 35% to a maximum peak of 73% at 240 minutes as well (Fig. 36). Load cell response to drainage follows the same path of other sensors initially but slows down around 350 minutes as drainage slowed and began to exit in pulses.

Ratio plots show the relationship between bulk ER and other sensing methods during wetting and drainage. Bulk ER and the moisture probes respond to the uniform wetting front at nearly a 1:1 ratio (Fig. 37). They follow the same path during wetting and drying and only diverge slightly near the end of the drying cycle. The relationship between saturation from load cells and bulk ER is different in that the wetting and drying path form an open loop with some curvature on each side (Fig. 38). Load cell wetting responds more rapidly than ER at early times and slows later. During early

drainage both sensing methods respond at nearly the same rate until late drainage when the rate of change in ER slows. Drainage from the lysimeter produced 1.6 liters and 0.6 liters remained in storage within the soil matrix, indicated by the separation of initial wetting and final drying positions.

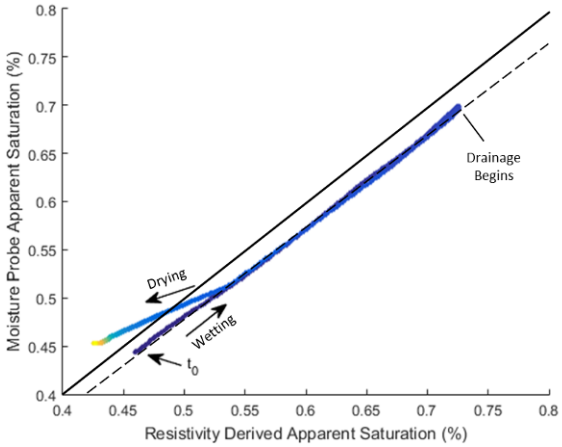

Figure 37: Ratio plot showing the relationship between saturation measured by moisture probes and bulk electrical resistivity.

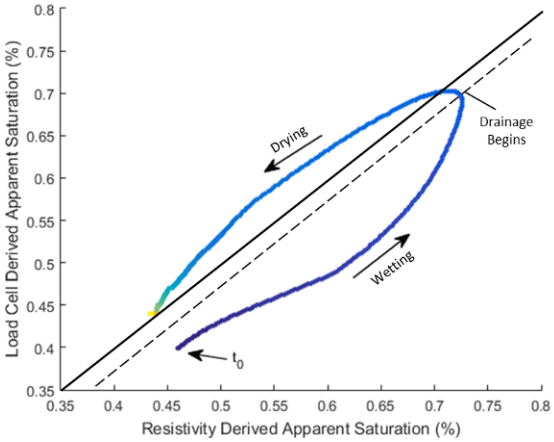

Figure 38: Ratio plot showing the relationship between saturation derived from the load cells and bulk electrical resistivity.

Important characteristics of this experiment are the relative response times and rates of each sensing method. Ratio plots showing a slope near to 1 indicate each sensing method was measuring roughly the same change in soil moisture through time. The sensing methods all reached a similar peak saturation value, within a 10% range in saturation. In order to best compare this dataset with other experiments, time series sensor data is normalized to distance or position of the wetting front (Fig. 39). For lysimeter experiments, since flow in this case is from the bottom up and other experiments will infiltrate from the top down, position of the wetting front is plotted as

relative to the current electrodes in the lysimeter. Position zero here is the lower current electrode B.

One important characteristic of this normalized data is the agreement with the moisture probes reaching peak saturation when the wetting front arrives at the depth of each probe (Fig 39). Additionally, the bulk electrical resistivity response agrees well with the simulation data for a uniform wetting front (Fig. 16, C). In the COMSOL simulation, vertical bulk resistivity is reduced when the wetting front reaches the second potential electrode and the region between electrodes M and N is well wetted. Here, apparent resistivity is minimized or apparent saturation peaks when the wetting front reaches the second potential electrode, or electrode M in this case since wetting is from the bottom upwards. The responses of the moisture probes and resistivity which indicate reaching saturation are in good agreement with the estimated arrival of wetting front depth in each case.

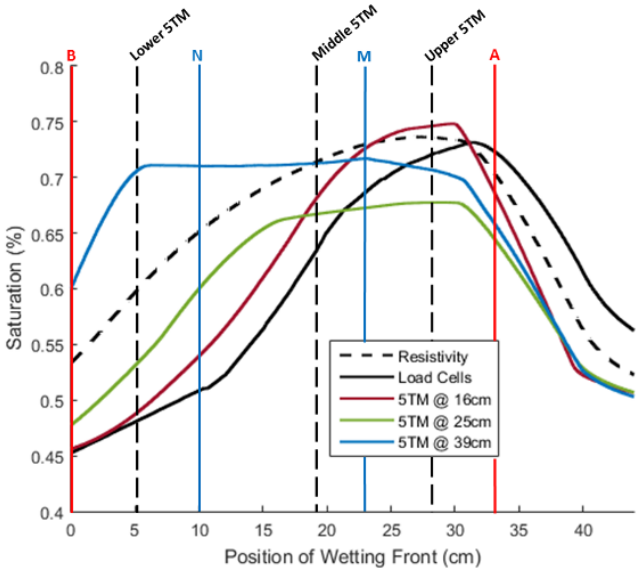

Figure 39: Uniform wetting experiment sensing data normalized to estimated position of wetting front above the lower current electrode B in the lysimeter ER array.

3.4.2: STEADY INFILTRATION EXPERIMENT

Following a period of drying to field capacity in lysimeter LYS-1, an infiltration experiment is conducted at a steady low flow rate over a long duration. Unfortunately, load cell data is not available for this experiment as it was corrupted during collection. Bulk electrical resistivity signal begins to show a slight response to infiltration after roughly 60 minutes, about 10 minutes prior to wetting arriving at the upper moisture probe (Fig. 40). As infiltration progresses downward, apparent saturation from the bulk ER signal continues to slowly increase. The wetting front arrives at the middle moisture probes at 25 cm depth around 110 minutes.

Signal from bulk ER begins to change rapidly just after at 130 minutes and apparent saturation increases by 45% over a period of about 40 minutes (Fig. 40). Finally, infiltration reaches the lower moisture probe after 170 minutes. Moisture probes all rise to an average saturation of 47%. Bulk ER continues to slowly increase until effluent begins to discharge around 320 minutes when interestingly ER begins to increase more rapidly. Once flow is halted, measured saturation declines

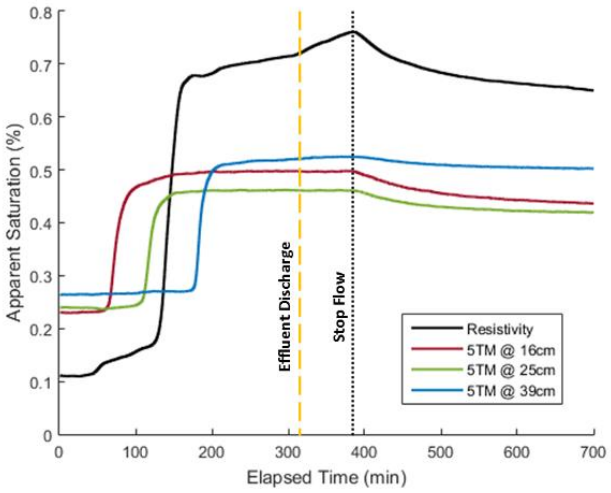

Figure 40: Results from steady low flow infiltration experiment in lysimeter LYS-1.

from the perspective of all sensing methods simultaneously. Total volume of effluent discharge is 1 liter, leaving approximately 3 liters remaining in storage at the end of the experiment.

The ratio plot of this experiment looks fairly different from the uniform wetting experiment in that the sensors seem to be responding almost independently (Fig. 41). This is likely a feature caused by the lower rate of wetting front progression here. Flux into the column was approximately the same as the uniform wetting experiment but the initial water content in the column is much lower here. As a result the wetting front is estimated to move only 0.16 cm/min compared to an estimated 0.20 cm/min in the uniform wetting experiment. Important features outstanding in the relationship between moisture probes and resistivity are the deviation from a slope of 1 and the relative magnitude of change in resistivity.

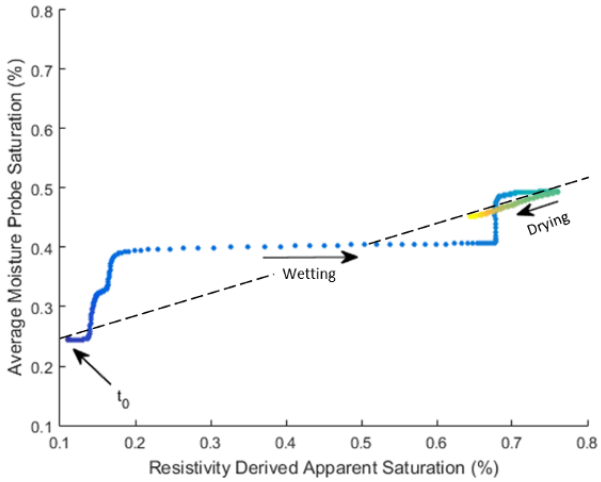

Figure 41: Ratio plot showing relationship between bulk ER data and moisture probe data.

Normalizing the sensor data to a depth axis shows some deviation from expected arrival times in this experiment (Fig. 42). The upper moisture probe does report saturation at the depth predicted, the same behavior seen by the probes in the

uniform wetting experiment (Fig. 39). However, the middle moisture probe seems to report the wetting front arrival just earlier than predicted and the lower probe reports saturation at the estimated depth of electrode N. This early arrival at the lower moisture probe comes in 5 cm before the probe depth, corresponding to about a 30 minute expected time difference. Bulk resistivity also reports saturation at around 17 cm or 30-40 minutes ahead of the expected arrival time of the wetting front. Additionally, the rate of change of all sensors from initial response to full saturation is more rapid than the responses seen in the uniform wetting experiment.

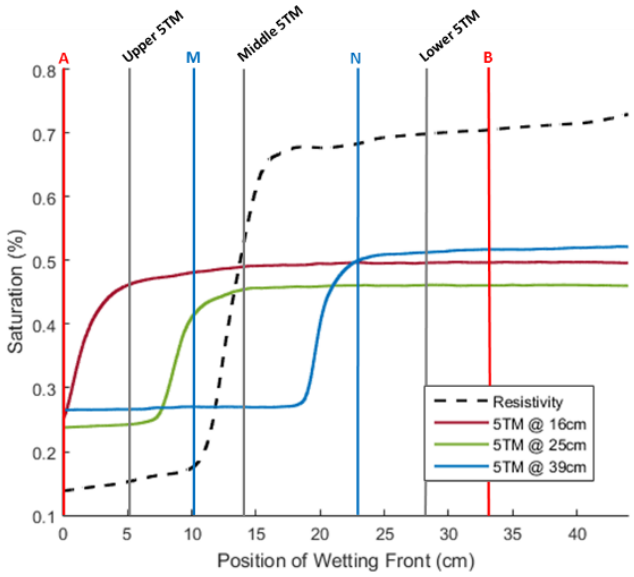

Figure 42: Sensor data normalized to the estimated wetting front depth in the lysimeter relative to the upper current electrode.

Comparing this infiltration data to the previous uniform wetting front experiment there are some similarities but also key differences. In both experiments resistivity begins to respond just prior to the first moisture probe as wetting interacts with the first current electrode. The first moisture probe to respond to the wetting front in both experiments behaves similarly, indicating at early times the character of the wetting front was similar. As infiltration progresses in this experiment, moisture probes begin to report saturation earlier than expected indicating that wetting is progressing

more rapidly than predicted based on the rate of irrigation. Vertical bulk resistivity reports increasing apparent saturation at a rate slightly faster than the moisture probes as well. These sensor responses could be attributable to preferential flow developing in the column as wetting progresses.

Infiltrating fluid which bypasses parts of the soil matrix will penetrate deeper than predicted with a uniform front, as seen in the CT column experiments. This behavior would explain early wetting reported by the lower moisture probes here as well as the character of the electrical response. As wetting in a macropore network through a soil system increases, so does connectivity between electrodes monitoring the system causing a reduction in bulk electrical resistivity. This bulk ER response to flow changes rapidly, as is seen with total bulk resistivity response to macropore flow in the CT2 column experiment (Fig. 30) and the larger magnitude of change is similar to the simulation results of vertical resistivity (Fig. 16, D). The continued increase in apparent saturation from resistivity after the moisture probes stabilize indicates there is additional wetting occurring, potentially imbibition of fluid into less saturated soil matrix from a macropore network. This subtlety may not be detected by moisture probes as the measurement region is fairly local to the probe location and may already be well wetted.

3.4.3: RAINFALL SIMULATION EXPERIMENT

A short series of rainfall simulations was conducted to monitor infiltration pulses through the lysimeter once macropore structures were observed to have formed. The lysimeter was allowed to dry for two weeks prior to the two short rainfall events. During infiltration of the first rainfall event, the upper 5TM moisture probe begins to show wetting at around 20 minutes, followed by the middle probe at 40 minutes and then the lower probe at 60 minutes (Fig. 43). Maximum saturation reported by upper and middle moisture probes is at 80 minutes but the lower probe peaks at 100 minutes.

Increased saturation is reported by bulk ER readings after just 10 minutes and the rate of wetting observed continues to increase until apparent saturation peaks at 80 minutes (Fig. 44). Saturation from load cells increases immediately with irrigation and

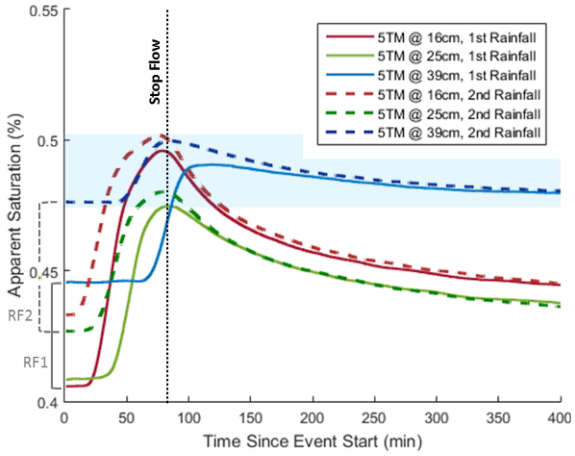

Figure 43: Moisture probe data where first rainfall event is shown as solid lines and the second event is dashed. Blue shaded region indicates range of peak saturations measured.

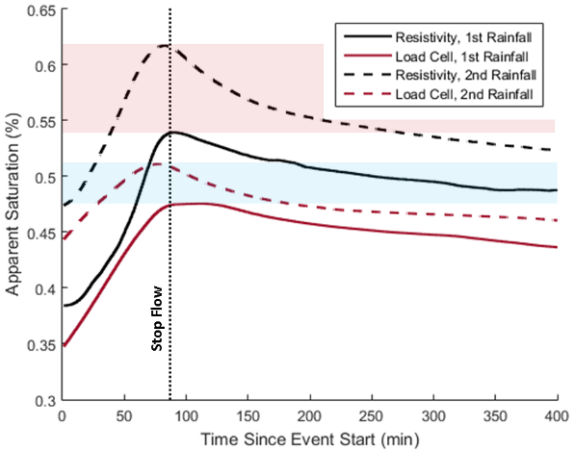

Figure 44: Bulk ER and load cell data. First rainfall event is shown as solid lines and the second event is dashed. Red shaded region indicates range of peak saturation reported by bulk apparent resistivity.

maintains a constant rate of change until peaking at 90 minutes when irrigation ceases. Total volume infiltrated during the first event is 700 mL and total effluent volume drained is 250 mL, indicating storage of 450 mL which results in the second rainfall event having a slightly wetter initial condition than in the first event.

When the second rainfall event begins after 12 hours of drainage and redistribution, the soil is more saturated than the initial conditions of the previous event. The upper portion of the column is 43% saturated and grades downward to 47% saturation in the lower column (Fig. 43). During this event, the upper 5TM moisture probe responds to wetting just after 10 minutes, where the middle probe responds by 30 minutes and the lower probe responds at 50 minutes. Maxima of the upper probes occur again at 90 minutes but the peak of the lower probe only follows by about 10 minutes. Bulk ER responds within minutes to infiltration and increases steadily until it peaks at 80 minutes. Resistivity and load cell measurements show a reduction of water content more rapid than during drainage of the first event (Fig. 44). Total volume infiltrated during the second event was again 700 mL and a total effluent volume of 600 mL drained from the column resulting in only 100 mL remaining in storage.

During both infiltration events, all moisture probes initially respond within about 20 minutes of each other, but the top and middle probes follow a similar saturation rate and peak almost simultaneously. The lower moisture probe response lags behind during the first event, but not as long as expected, and in the second event the lower probe

peak occurs very shortly after the other probes. This is an indication that infiltration is penetrating into the column rapidly in the first event and even more so in the following event as the column is wetter initially. Apparent saturation measured by the load cells is within the same range as the moisture probes, as indicated by the blue shaded region in figures 43 and 44. However, in both cases bulk ER indicates higher degree of saturation.

Ratio plots of the relationship between sensing methods for this experiment series feature some characteristics which differ from the uniform wetting scenario as well. Results from both rainfall events show a deviation from equal ratio slope where apparent saturation derived from bulk ER is changing more rapidly than moisture probes or load cells (Fig. 45). Load cell response is initially more rapid than bulk ER as irrigation is added to the column but not yet infiltrated into the ER array sensing region. Bulk ER and moisture probe responses do not follow the same wetting and drying pathway in this case. In the first rainfall event, the drying pathway does not return to the initial condition but stops approximately halfway along the wetting path due to storage in the soil matrix.

Interestingly, all the relationships share a common kink feature in the bottom portion of the drying curve where for some time bulk ER is relatively stable while the other sensors indicate falling water content, followed by a period of the inverse where bulk ER reduces while the other sensors remain relatively stable (Fig. 45). This feature is likely related to the end of effluent discharge and the beginning of redistribution. Load

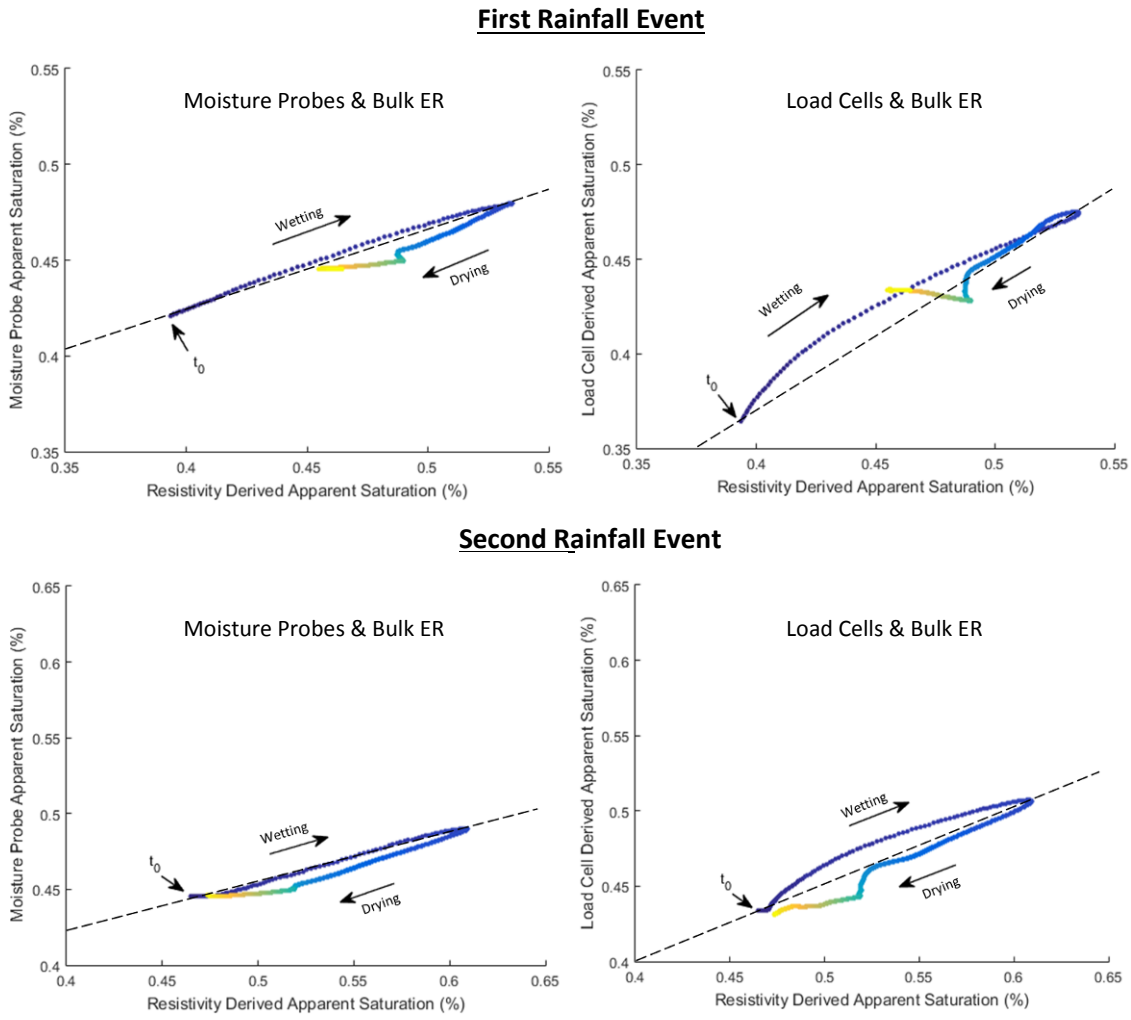

Figure 45: Ratio plots showing relationship between bulk ER and other sensing methods in the lysimeter column during the rainfall simulation experiment.

cells show mass leaving the bottom of the column which is outside the ER array sensing region, and once effluent stops redistribution of moisture in the soil matrix could reduce the effective resistivity in the sensing region further reducing the electrical signal.

Direct comparison can again be done between these infiltration events and previous experiments by normalizing the time axis to estimated wetting front. Resulting

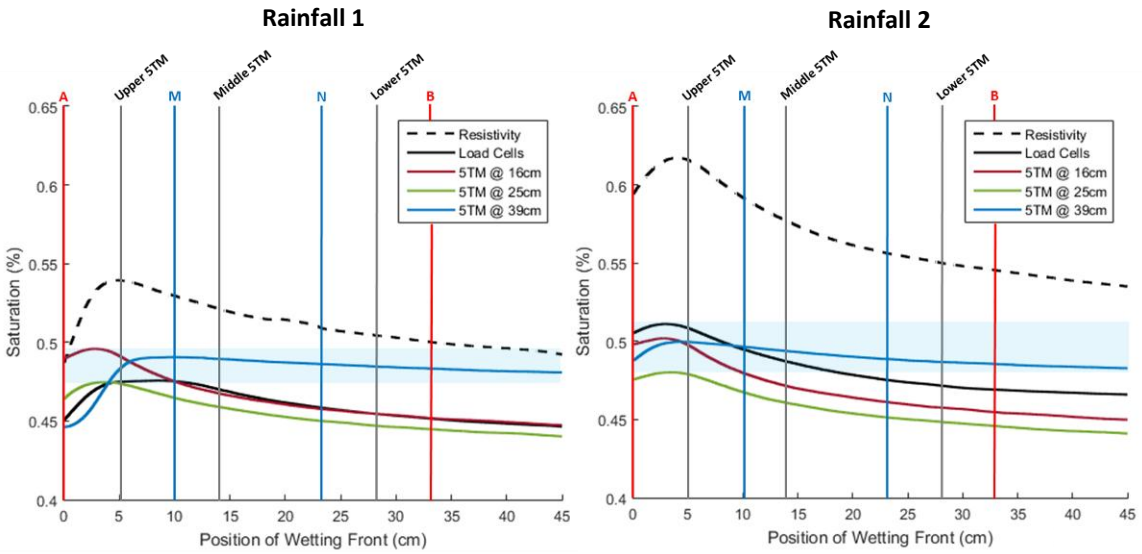

Figure 46: Sensing data from each rainfall event normalized to depth of wetting front relative to the top electrode tier 1 or electrode 'A'. Rainfall event 1 is shown on left and event 2 on right. Blue highlight indicates range of peak saturation measured by moisture probes and load cells.

plots indicate that infiltration in these wetting events is progressing through the soil column more rapidly than would be predicted (Fig. 46). During both rainfall events, the predicted depth of a uniform wetting front by the end of 1.5 hours would be 15-18 cm from the soil surface or as represented here, 4-7 cm past current electrode A. However, by the time the wetting front should be arriving at the upper moisture probe, all sensing methods in the column have already reported increased saturation and reached peak water content recorded.

During this rainfall simulation experiment, both irrigation events had very similar responses with the only difference between the experiments being the initial water content in the column at the start of irrigation. Trends in sensor response characteristics are similar to the previous steady long duration infiltration experiment (section 3.4.2).

Apparent saturation measured by bulk electrical resistivity was 10-30% larger than saturations indicated by the moisture probes or load cells, which all reported similar ranges of saturation indicated by blue shading in figure 43, 44 and 46. Additionally, the early arrival time of each sensing method is indicative of preferential flow occurrence, enabling parts of the soil matrix to be bypassed. Ratio plots skewed to more rapid electrical resistivity response is consistent with potential occurrence of preferential flow and deviates from results found in the uniform wetting experiment (Fig. 37). Supplementary information is also gathered in the form of 2D X-rays of the lysimeter column after this experiment to determine if there is evidence of macropore network formation in the column. Results of the X-rays show clear cracks in the soil structure at multiple depths in the column that could facilitate preferential flow (Appx. 5.1).

3.4.4: ARTIFICIAL MACROPORE EXPERIMENT

The final experiment conducted with the lysimeter platform is engineered to produce macropore dominated flow through the soil profile. Lysimeter column LYS-2 is used to modify an otherwise homogenous soil structure with a 1 inch diameter artificial macropore. Irrigation is dyed with a blue tracer and infiltration is monitored using the same sensing methods as previous lysimeter experiments. In this extreme case of macropore flow, irrigation at the surface only infiltrated the upper soil matrix by approximately 1.5 cm into the upper soil matrix but channeled through the macropore and bypassed much of the upper soil matrix.

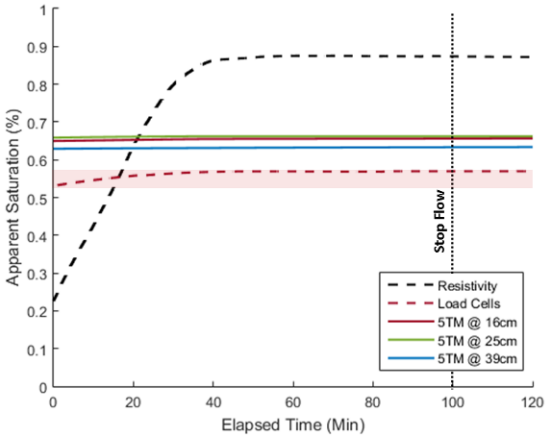

Figure 47: Sensing results from macropore experiment in lysimeter LYS-2.

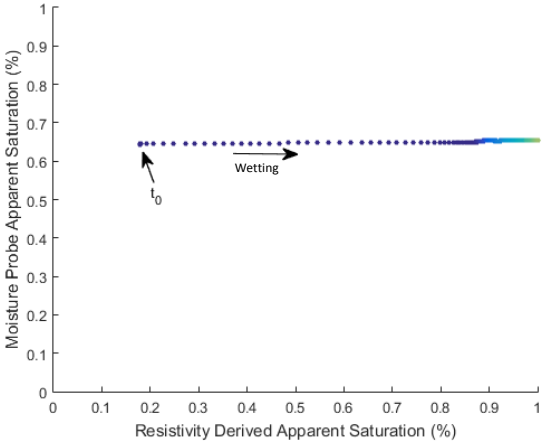

Figure 48: Macropore experiment ratio plot between moisture probes and bulk ER.

Response from all the moisture probes for the duration of the experiment was minimal though the infiltration volume was detected by the load cells (Fig. 47). Response of bulk ER signal was significantly greater with a 70% change in apparent saturation. The relationship between moisture probes and the electrical resistivity signal in this case is dramatically different than previous experiments such that a ratio plot of the methods shows a horizontal slope of nearly zero (Fig. 48). Within 40 minutes the macropore structure in the column is saturated and irrigation began to pond at the soil surface. Once ponding at the surface develops, preferential flow began to occur along the column side walls at the outer soil boundary (Fig. 49). Once a ponded depth of approximately 1 cm was observed the irrigation was halted and the column was allowed free evaporation during redistribution and drainage.

No effluent was produced by the soil column for the duration of the experiment. Following a period of one week the remaining irrigation solution is siphoned out of the

column and the soil profile is excavated. Soil is removed in layers approximately 1 inch thick from the upper surface downward and the distribution of blue tracer dye is documented (Fig. 49). Irrigation is found to have consistently penetrated about 1 cm into the soil matrix at the soils upper surface and along the walls of the macropore structure. Dye tracer solution was found along the outer soil boundaries at a majority of excavated depth sections and is found to periodically extend inward in small volumes (Appx. 5.8).

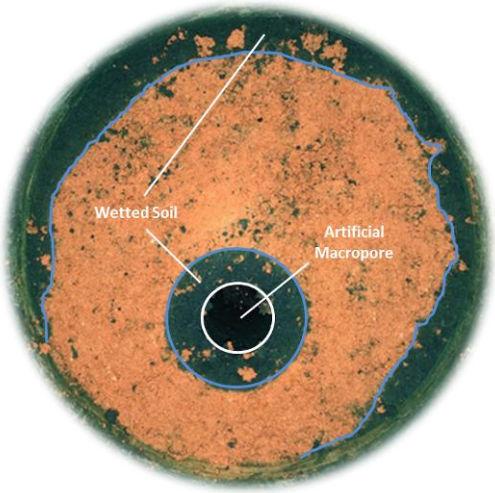

Figure 49: Excavated cross-section of lysimeter column LYS-2 after macropore experiment with blue tracer dye.

Soil matrix in this lysimeter column LYS-2 was packed to a higher soil density than the lysimeter LYS-1 used in previous experiments, and permeability in the soil matrix was much less as indicated by the extent of wetting in the soil after a week of redistribution. Given preferential flow along the column walls occurred in this experiment it is probable that the same occurred in other experiments with lower density packing. Additionally, the observed resistivity response to macropore filling in this experiment is informative in terms of the magnitude of apparent saturation reported in comparison to minimal wetting observed in the soil matrix. Similar characteristics were observed in both the steady infiltration experiment and rainfall simulations in the lysimeters.

SECTION 4: CONCLUSIONS

4.1 RESEARCH CONCLUSIONS

In assessing the ability of bulk electrical resistivity monitoring to determine the occurrence of a uniform wetting front versus preferential flow through a heterogeneous system, the examination of simulation data and experimental results reveal some consistent trends that suggest the application is viable. Simulations of resistivity response to preferential flow revealed that wetting in a macropore causes increases in effective conductivity of the measurement region of an electrical array, thereby eliciting a reduction in apparent resistivity. Uniform wetting front simulations showed characteristics of apparent resistivity response such as gradual reduction in resistivity as the wetting front passes through an array as well as the position of the wetting front relative to electrodes when resistivity responses occur. These characteristics from the simulations matched behavior of apparent resistivity observed in the CT1 column experiment and uniform front lysimeter experiment.

Comparing the results from the CT column experiments, vertical bulk resistivity was observed to reduce gradually with uniform wetting and more rapidly when preferential flow was occurring through the macropore network (Fig. 50). Conversely, horizontal apparent resistivity reduced sharply with the progression of the uniform

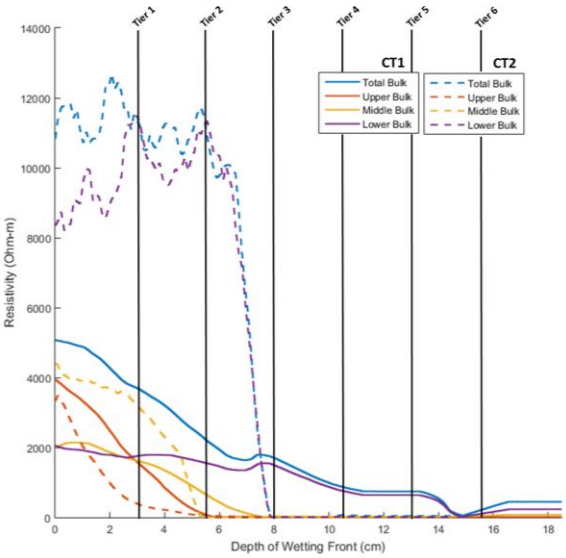

Figure 50: Vertical bulk resistivity measurements for CT1 and CT2 column experiments. CT1 uniform wetting shown as solid lines, CT2 macroporous wetting shown as dashed lines.

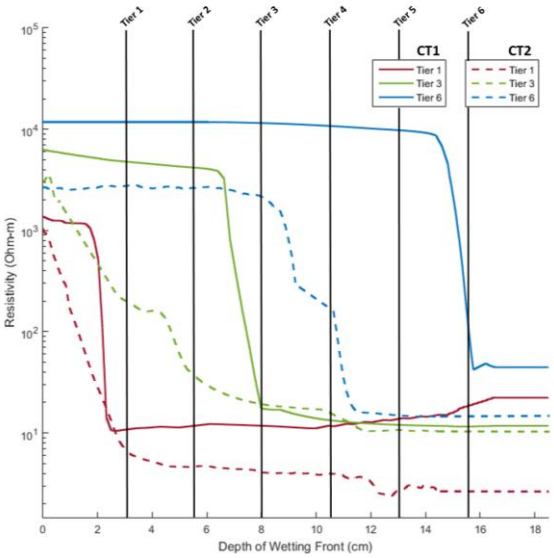

Figure 51: Horizontal bulk resistivity measurements for CT1 and CT2 column experiments. CT1 uniform wetting shown as solid lines, CT2 macroporous wetting shown as dashed lines.

wetting front and gradually during preferential flow (Fig. 51). This difference in rate of change of apparent resistivity with infiltration in macroporous and non-macroporous systems is attributable to the differences in anisotropy of effective conductivity. Anisotropy of electrical resistivity measurements in the CT columns is observed to show distinct peaks or spikes when preferential flow is occurring within the system and the magnitude of anisotropy during macropore flow is significantly larger than during uniform wetting.

Results from the lysimeter experiments also show similar apparent resistivity behavior to the CT column experiments. In the uniform front lysimeter experiment, apparent resistivity reduces gradually with the progression of wetting (Fig. 52). Though

in comparison, the other infiltration experiments in the lysimeter show more rapid reduction in apparent resistivity over shorter periods of time. Generally, there is also a trend of higher magnitude apparent resistivity values associated with vertical bulk resistivity measurements during preferential flow. In the macroporous CT2 column experiment, the change in middle, lower, and total bulk resistivity values was more than twice the magnitude of change seen in the non-macroporous experiment CT1 (Fig. 50). Similarly the change in apparent resistivity in the steady infiltration and macropore lysimeter experiments was much larger magnitude than in the uniform wetting experiment. Recall as well that apparent saturation derived from bulk electrical resistivity in the lysimeters was larger than saturations measured by moisture probes in all but the uniform wetting case.

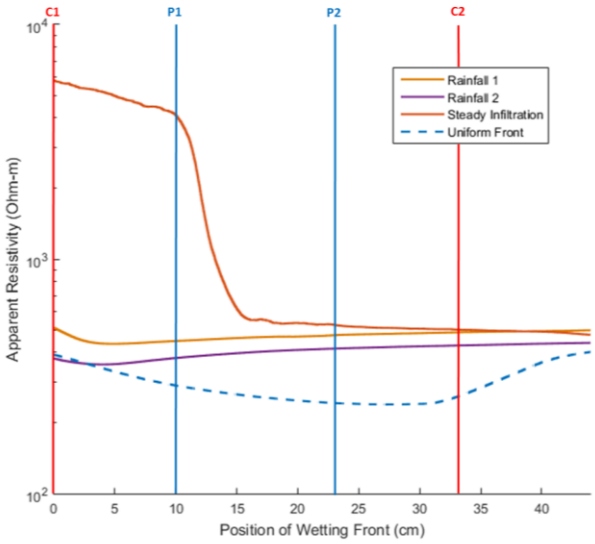

Figure 52: Vertical bulk resistivity of lysimeter experiments normalized to position of wetting front within the electrode array.

Another characteristic observed across all experiments is sensor response times which occur earlier than predicted during preferential flow. This is compared across experiments by calculating how early wetting arrives at each sensor relative to estimated arrival time using equation 8. Early arrivals relative to predicted time is presented as a percentage of predicted arrival time using equation 9. In the

$$\frac{Predicted\ Arrival - Observed\ Arrival}{Predicted\ Arrival} \cdot 100 \qquad \text{(Equation 9)}$$

CT column experiments, resistivity measurements indicated saturation earlier in the macroporous column than the homogeneous column in almost every electrode array configuration (Fig. 53). Likewise, in the lysimeter rainfall simulation experiments, sensors indicated peak saturations much earlier than expected. Generally, experiments which likely had preferential flow occurring during infiltration there is a significant

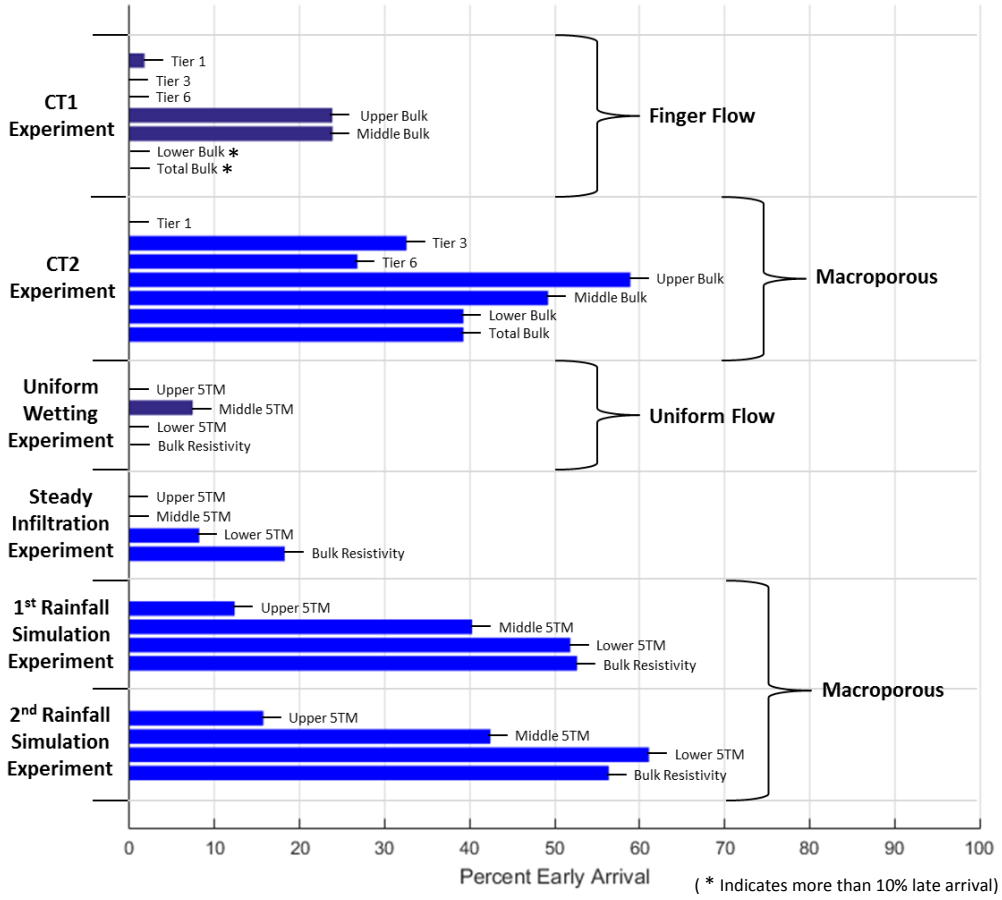

Figure 53: Relative arrival times of sensing methods in each experiment. Arrival times normalized to early arrival time's percentage of expected arrival time. 0% early arrival would correspond with estimated arrival time from equation 9. Dark blue indicates experiments with uniform wetting fronts.

increase in arrival time relative to the expected arrival time of the wetting front.

Overall, the primary indicators of preferential flow observed in bulk electrical resistivity data are rapid rates of change in vertical apparent resistivity, early arrival times relative to what is predicted using bulk soil properties, sharp spikes in electrical anisotropy and the increased magnitude of apparent saturation indicated by electrical resistivity. These characteristics indicate that electrical resistivity is a viable method for application in detecting preferential flow during infiltration in a heterogeneous system. Further investigation of this application would undoubtedly strengthen the capabilities of the method.

4.2 FUTURE WORK

This line of research would be advanced through the collection of additional laboratory experiments, field lysimeter monitoring and through simulations with additional complexity. In order to investigate the electrical resistivity response to the activation and deactivation of macropore flow, a series of sequential wetting events could be designed for a macroporous CT column. Infiltration should be applied to the same column over multiple events of equal flux and short duration with a period of redistribution in between. This would provide cycles of wetting and drainage in a macropore network, leading to the potential to observe repetitive trends in monitoring data related to the activation and deactivation of the macropore.

Additionally, longer term monitoring of multiple lysimeter columns deployed in the field and exposed to natural rainfall events would provide a suite of electrical resistivity observations of infiltration. Including measurements of anisotropy in the lysimeter columns would be beneficial considering the promising results obtained here with the CT columns. Monitoring infiltration in lysimeters with various extents of macropore networks or plant rooting would be helpful to understand the apparent resistivity response to varying degrees of preferential flow. Simulations with increased complexity such as 3D models that couple electrical physics with active flow dynamics and more variations of macropore geometry and electrode array geometries would be very helpful to understand how the effects of heterogeneity are realized in observations of apparent resistivity.

Ultimately this work could lead to the development of a practical application of ER monitoring whereby inexpensive sensors integrated with simple four electrode arrays could be deployed throughout a field site and establish multiple observation points of infiltration characteristics. Monitoring data as such could provide information about the extent of preferential flow occurring at a contaminated field site from the meter scale to landscape scale. This sort of data would provide additional insight into an environmental system to better inform predictive models and thereby facilitate increased efficiency of contamination remediation at degraded sites.

REFERENCES

Archie, G.E. (1942) The electrical resistivity log as an aid in determining some reservoir characteristics, Transactions of the American Institute of Mining and Metallurgical Engineers. Vol. 146, Pg. 54-61.

Beven, K., Germann, P. (2013) Macropores and water flow in soils revisited, Water Resources Research. Vol. 49, 3071-3092.

Binley, A. (2013) R2 readme version 2.7a, Lancaster Environment Centre, Lancaster University. http://www.es.lancs.ac.uk/people/amb/Freeware/R2/R2.htm (Accessed March, 2018).

Bogaard, T.A., Greco, R. (2015) Landslide hydrology: from hydrology to pore pressure, Wiley Interdisciplinary Reviews: Water, Vol. 3.

COMSOL. (2019) COMSOL Multiphysics 5.2a software documentation.

Decagon Devices (2017a) MPS-1 dielectric water potential sensor operator's manual. http://manuals.decagon.com/Manuals/Discontinued/MPS-1-Operators-Manual-(discontinued).pdf (Accessed Feb, 2017).

Decagon Devices (2017b) 5TM water content and temperature sensors. http://manuals.decagon.com/Manuals/13441_5TM_Web.pdf (Accessed Feb, 2017).

Fowler, D.E., Moysey, S. (2011) Estimation of aquifer transport parameters from resistivity monitoring data within a coupled inversion framework, Journal of Hydrology. Vol. 409, 545-554.

Google (2019) Map data. https://goo.gl/maps/JFVVfGtAPtvaBhcdA (Accessed June, 2019).

Herman, R. (2001) An introduction to electrical resistivity in geophysics, American Journal of Physics. Vol. 69, No. 9, 943-952.

Jarvis, N.J. (2017) A review of non-equilibrium water flow and solute transport in soil macropores: principles, controlling factors and consequences for water quality, European Journal of Soil Science. Vol. 58, 523-546.

Li, M., Tang, Y. B., Bernabe, Y., Zhao, J. Z., Li, X. F., Bai, X. Y., Zhang, Z. H. (2015) Pore connectivity, electrical conductivity and partial water saturation: network simulations, Journal of Geophysical Research: Solid Earth. Vol. 120, 4055-4068.

Liu, Z., Moysey, S. (2012a) Can the onset of macropore flow be detected using electrical resistivity measurements, Soil Science Society of America Journal. Vol. 76, No. 1.

Liu, Z., Moysey, S. (2012b) The dependence of electrical resistivity-saturation relationships on multiphase flow instability, ISRN Geophysics.

Luo, L., Lin, H., Halleck, P. (2008) Quantifying soil structure and preferential flow in intact soil using X-ray computed tomography, Soil Science Society of America Journal. Vol. 72, pg. 1058 – 1069.

Mamun, A., Moysey, S., Dogan, M., Murdoch, L. (2018) Visualizing macropore flow mechanisms using 4D X-ray computed tomography imaging within a heterogeneous porous medium, American Geophysical Union Fall Meeting 2018. Section H34F.

Omega. Economical OEM-style single point load cells. http://www.omega.com/pressure/pdg/LCAE.pdf (Accessed Feb, 2017).

Powell, B. (2017) Radionuclide waste disposal: development of multi-scale experimental and modeling capabilities, South Carolina DOE EPSCoR Implementation renewal proposal. Project DE-SC0012530.

Simunek, J., Jarvis, N.J., van Genuchten, M.Th., Gardenas, A. (2003) Review and comparison of models for describing non-equilibrium and preferential flow and transport in the vadose zone, Journal of Hydrogeology. Vol. 272, 14-35.

Singh, Y. (2013) Electrical resistivity measurements: A review, International Journal of Modern Physics: Conference Series. Vol. 22, Pg. 745-756.

Savannah River Site (SRS) (2019) SRS history highlights. https://www.srs.gov/general/about/history1.htm (Accessed June, 2019).

Wang, Z., Feyen, J., van Genuchten, M. Th., Nielsen, D.R. (1998) Air entrapment effects on infiltration rate and flow instability, Water Resources Research. Vol. 34, No. 2, 213-222.

Wightman, W.E, Jalinoos, F., Sirles, P., Hanna, K. (2003) Application of geophysical methods to highway related problems, Federal Highway Administration, Central Federal Lands Highway Division, Lakewood CO. Publication FHWA-IF-04-021.

APPENDICES

1: PHYSICAL SIMULATION

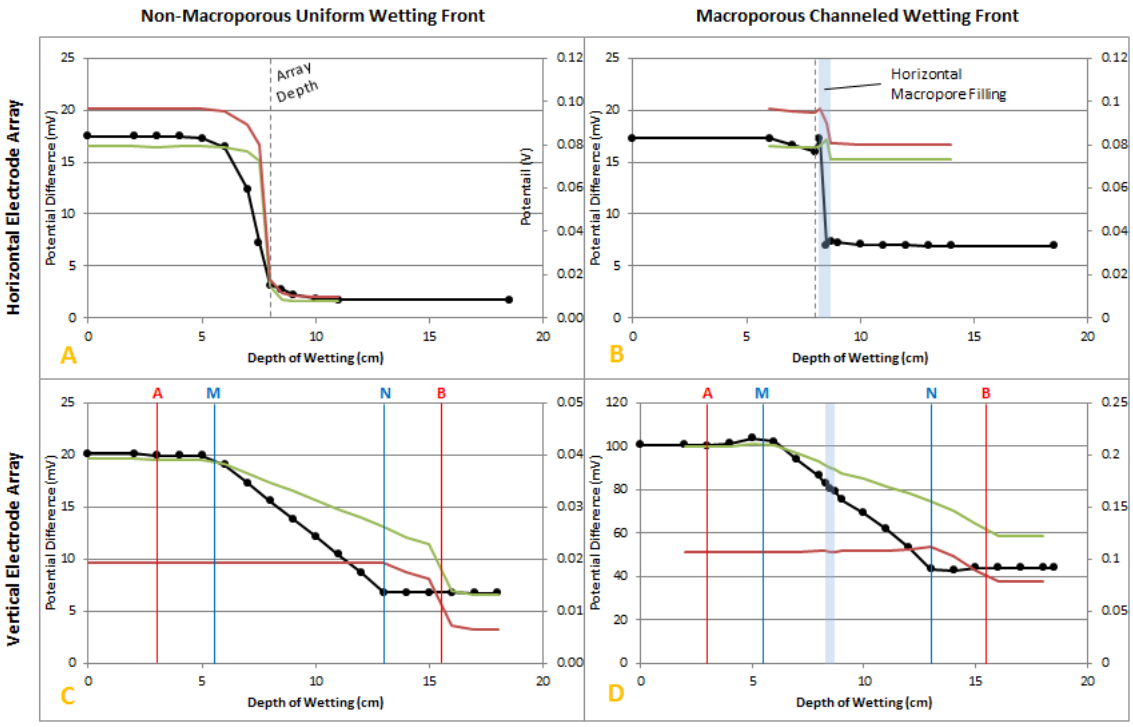

Appendix 1.1: COMSOL simulation results showing electrical potential differences (in mV) for each simulated scenario but also including potential (in Volts) measured at each electrode M (green) and N (red).

Additional potential data from simulations is presented within this figure. Point measurements of electric potential from each potential electrode are shown. The relative changes between them in difference cases may be informative as opposed to just viewing their computed difference. The higher potentials are measured by the M electrode, and lower by the N electrode. Individual potential plotted to the secondary y-axis and is represented in Volts as opposed to potential difference in mV.

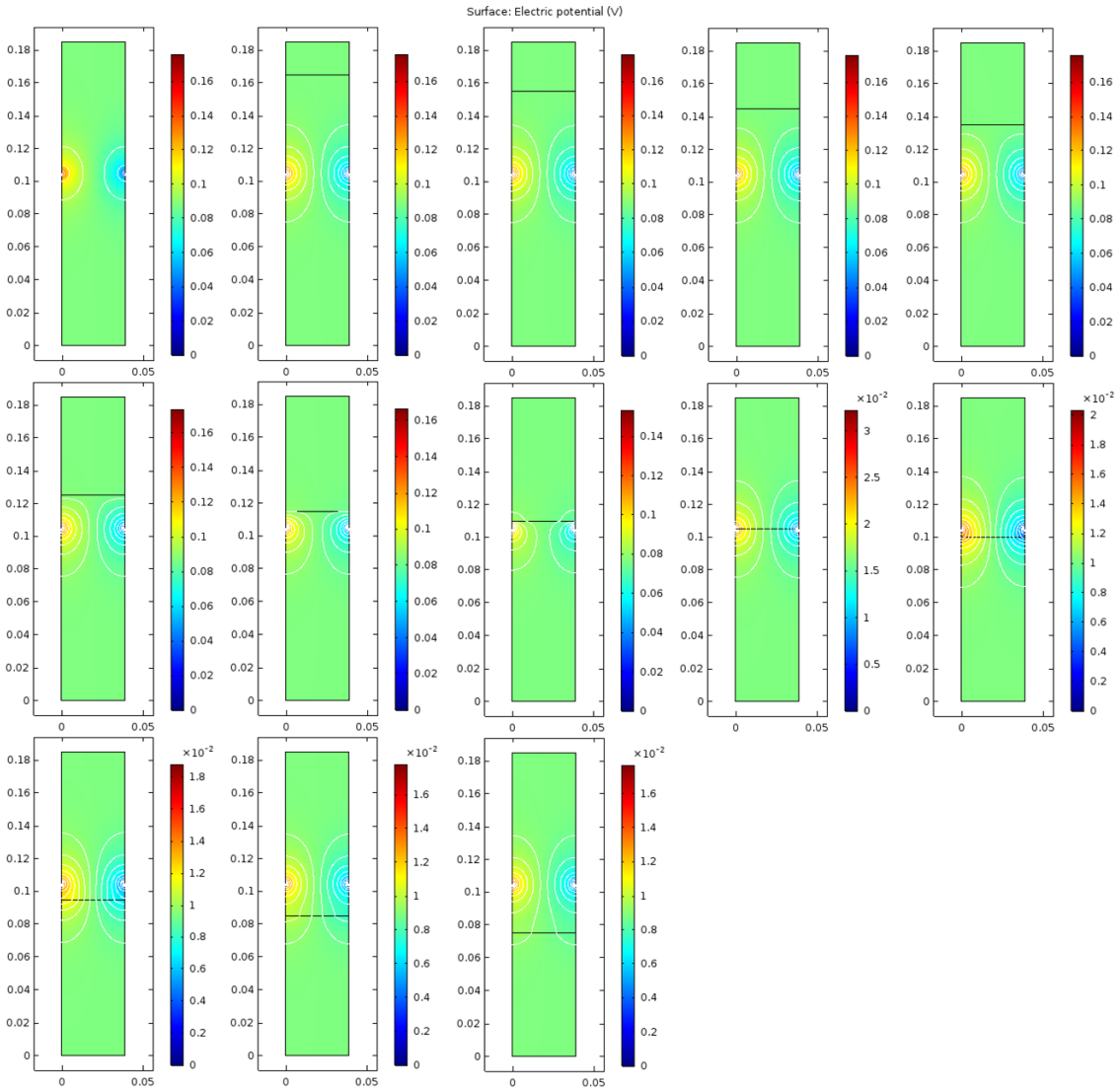

Appendix 1.2: COMSOL simulation results showing electrical potential field distribution as a homogeneous wetting front passes through a horizontally oriented electrode array. Model steps are presented from left to right, top to bottom. The wetting front boundary is represented by the thin black line in the model space.

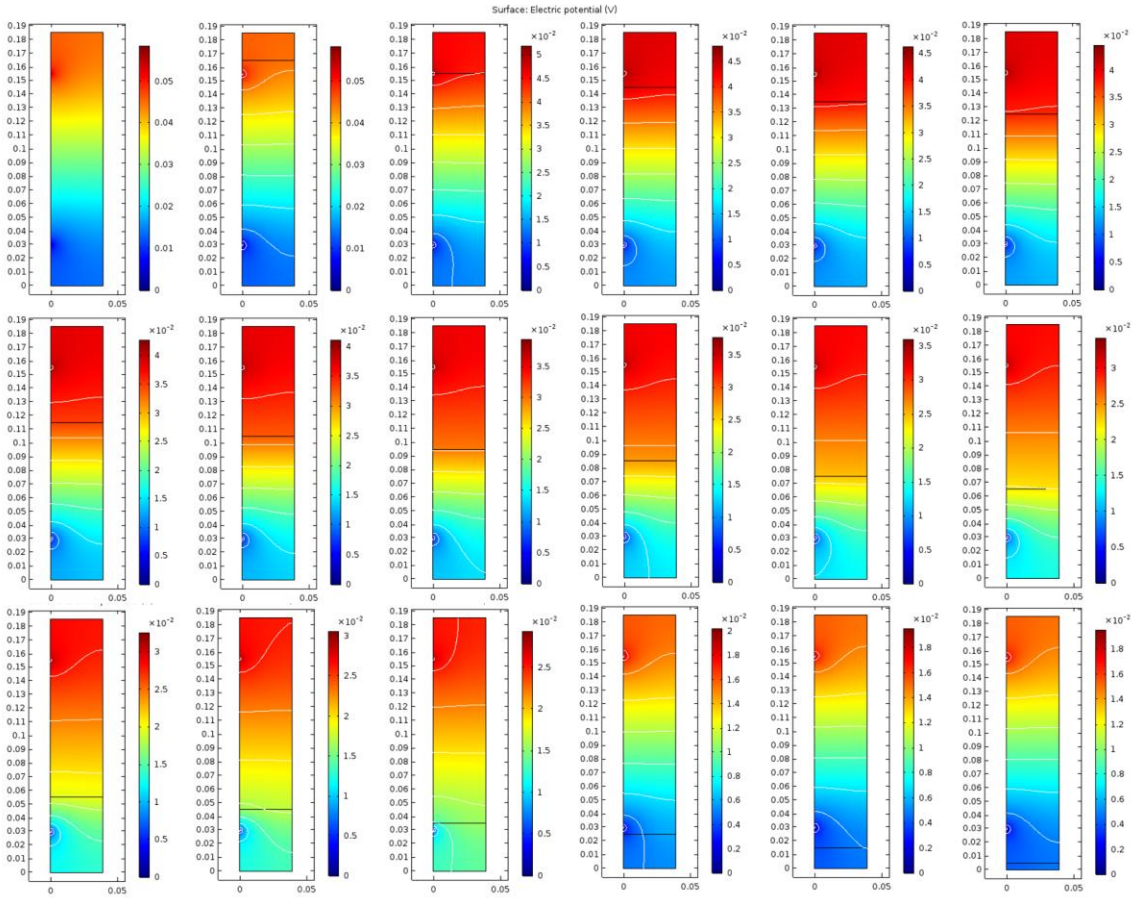

Appendix 1.3: COMSOL simulation results showing electrical potential field distribution while a homogeneous wetting front progresses through a vertically oriented electrode array along the left side of the model space.

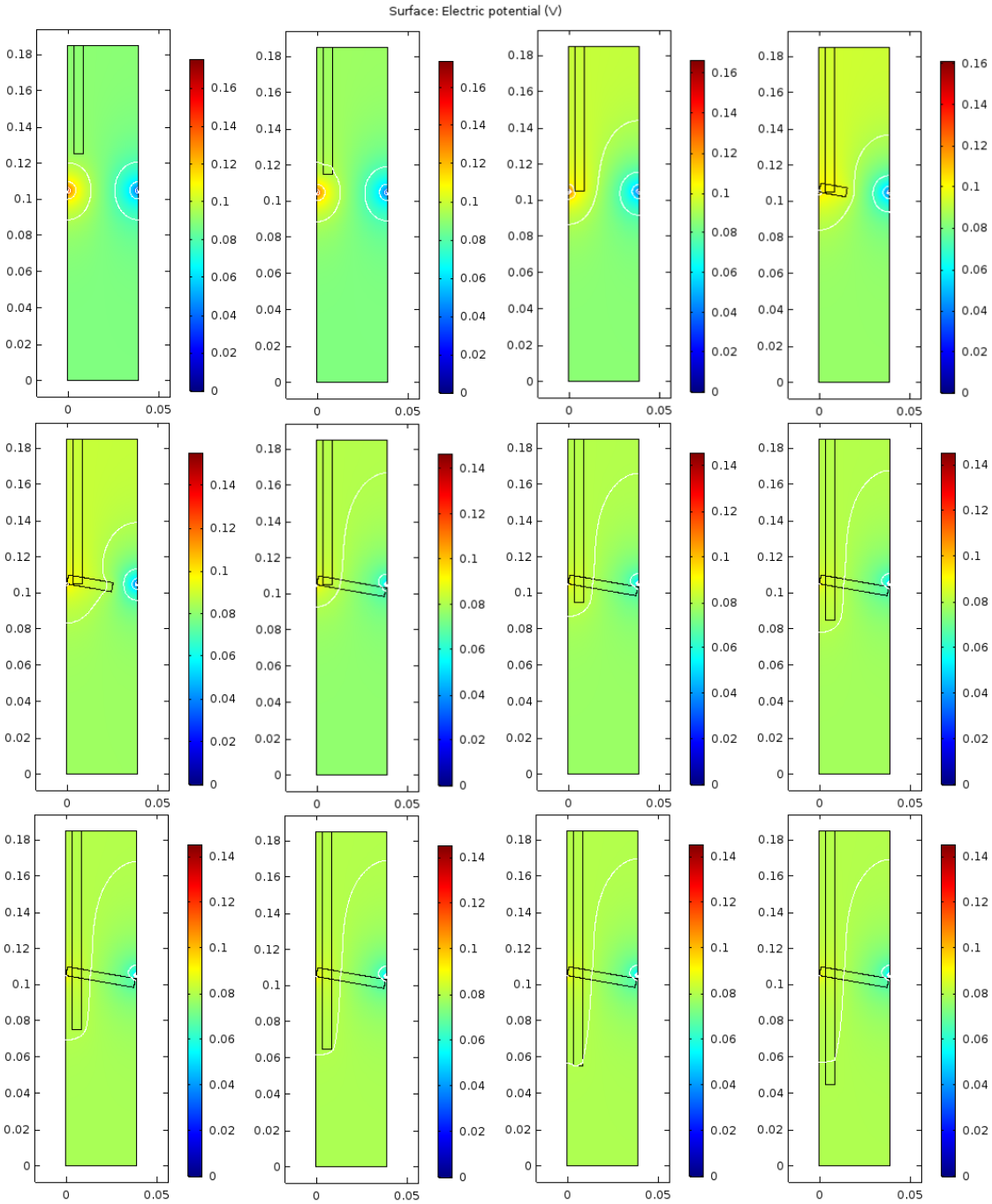

Appendix 1.4: COMSOL simulation showing electrical potential field distribution resulting from a wetted area in a macropore structure as it progresses past a horizontal electrode array. Black rectangles represent the wetted area of the macropore structure at each model step.

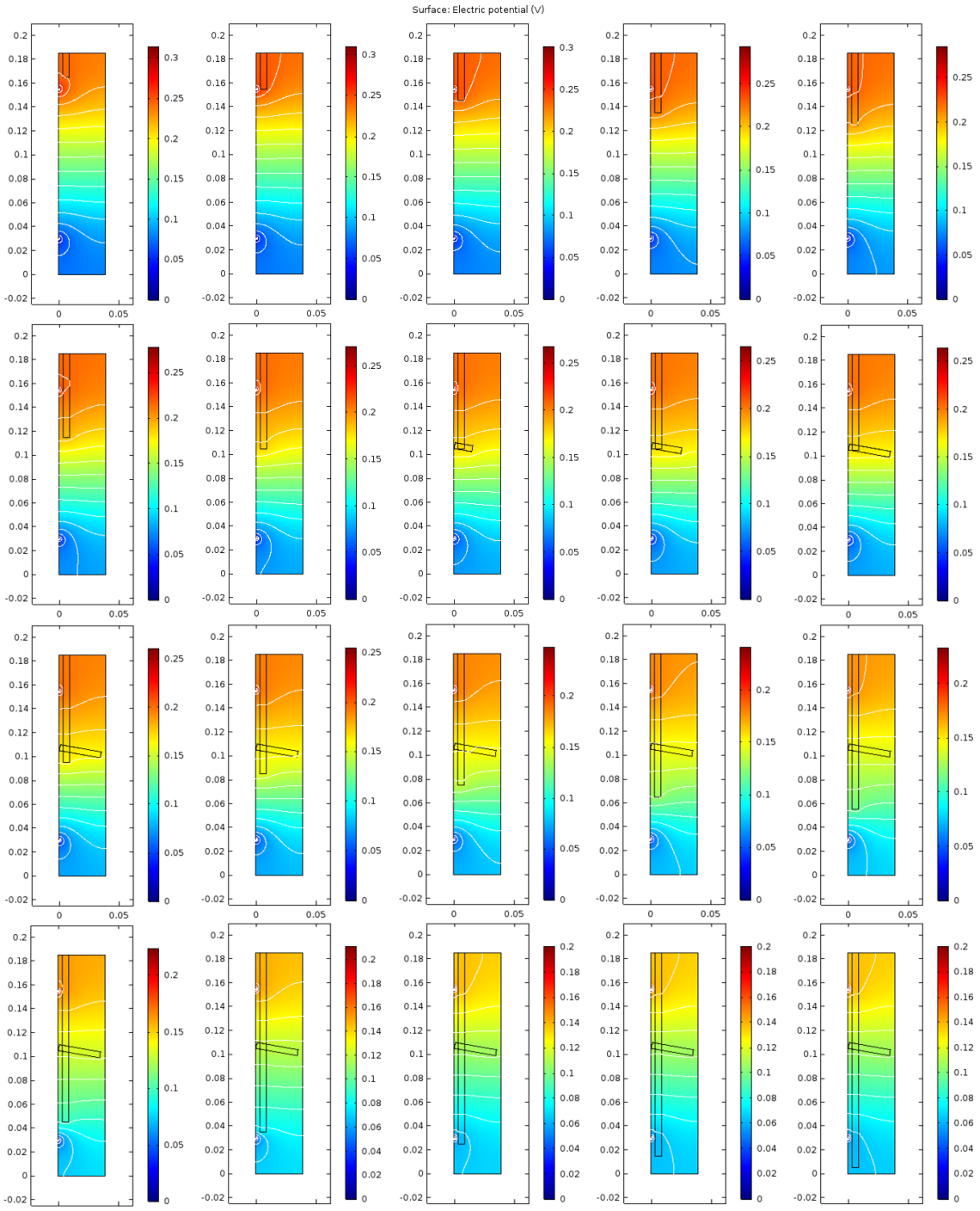

Appendix 1.5: COMSOL simulation showing electrical potential field distribution resulting from wetting in a macropore structure passing through a vertically oriented electrode array.

2: ARCHIE'S LAW CALIBRATION

Appendix 2.1: Humboldt soil testing box used for measuring resistivity of calibration samples with IRIS SYSCAL-Pro

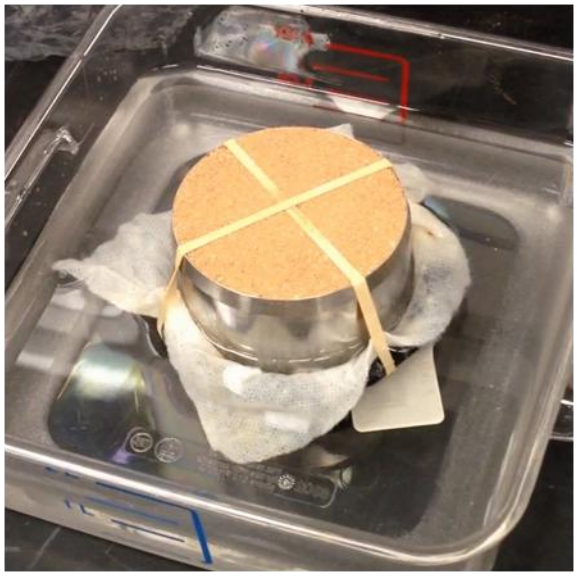

Appendix 2.2: Laboratory setup used for determining porosity. Steel cylinder with known volume filled with soil sits in a basin of water with a filter cloth to retain soil structure. Soil column is allowed to saturate from the bottom by capillary pressure.

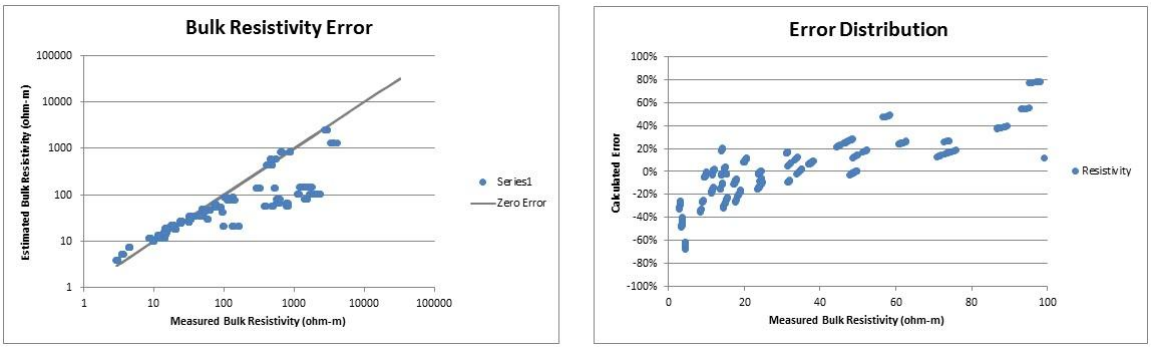

Appendix 2.3: Figures show measurement error from calibration experiments. Left figure shows theoretical zero error and with each measurements relative distance from minimum error. As resistivity increases so does the potential for erroneous measurements. Right figure shows calculated error in relation to resistivity, again showing increased error at higher resistivity values.

3: ERROR ANALYSIS AND SENSOR CALIBRATIONS

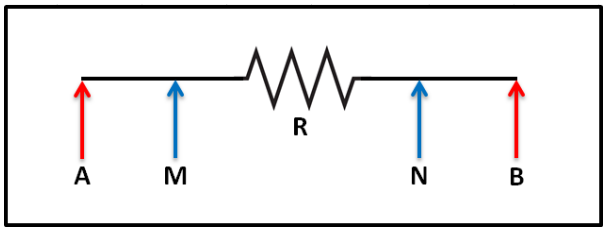

Appendix 3.1: Quadripole measurement configuration for resistance testing of IRIS SYSCAL-Pro. A & B represent current (I) connections and M & N represent potential (V) measurement connections. R represents a resistor with constant line resistance.

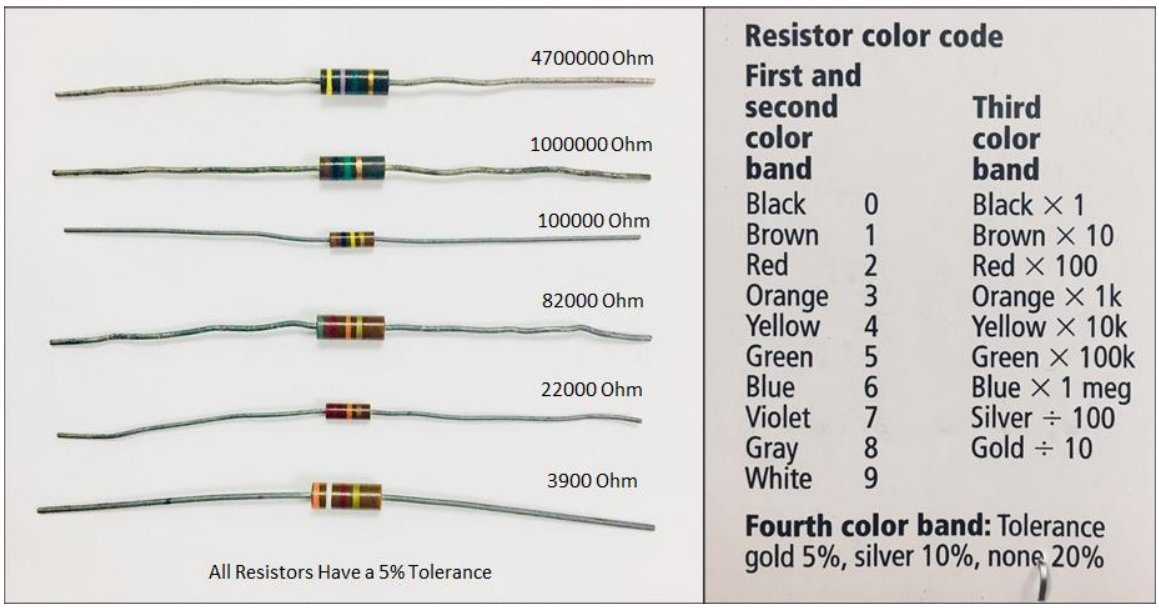

Appendix 3.2: Resistors used to test IRIS SYSCAL-Pro. Each resistor shown above was used with each channel in a quadripole configuration (Appx. 2.1). For example, the first measurement uses channels 1 through 4 where 1=A, 2=M, 3=N, 4=B. Each consecutive channel tested used the same configuration by increasing A,B,M,N each by 1 respectively until A=48, M=1, N=2, B=3.

Measurement error of the IRIS SYSCAL-Pro resistivity meter used is assessed by measuring resistance across engineered resistors with a known resistance value. Most channels are found to have similar responses except channels 3-6 and 26. Measurements have higher error when measuring larger resistances. Measurements of resistor 4, which has a resistance of 100,000 Ohms, consistently have the highest error across all channels.

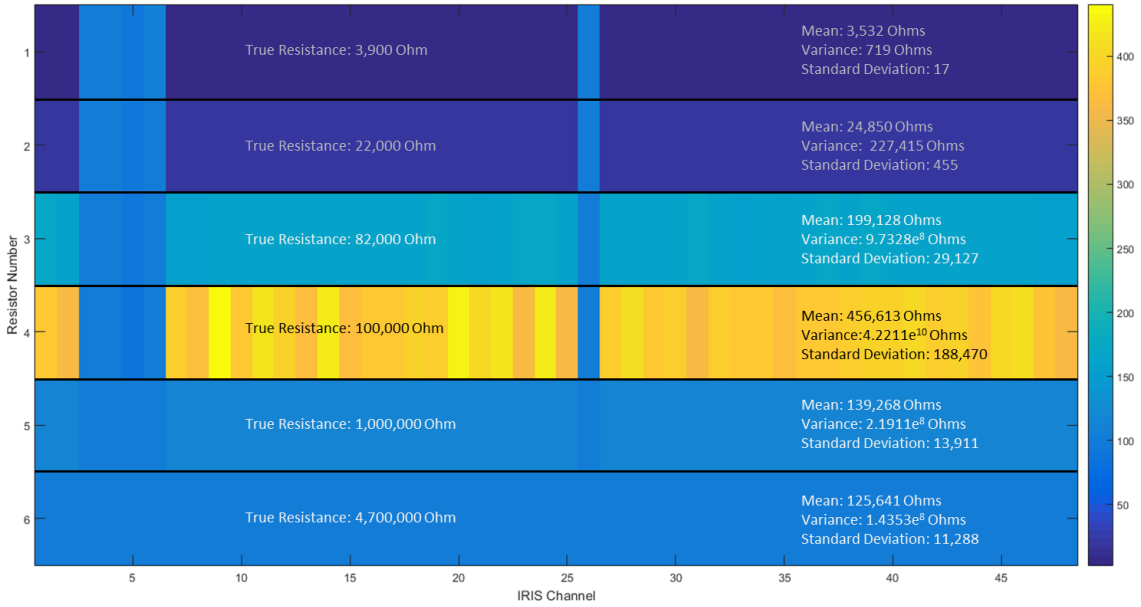

Appendix 3.3: Representation of percent error in measurements of resistors with known values using IRIS SYSCAL-Pro resistivity meter. Color bar to right indicates percent error. IRIS channels 1 through 48 are represented as columns along the x-axis. Resistors are represented as rows in the y-axis. Resistor 1 is the lowest Ohm resistor used where resistor 6 is the largest (Appx. 3.2).

Electrical resistivity tomography (ERT) gathered in the lysimeter columns needs to have the resolution capabilities and accuracy evaluated because unconventional electrode array geometry is used. ERT control images were taken in a 6 inch diameter polyvinyl chloride (PVC) ring that is 8 inches tall with a 48 electrode array identical to each of the arrays installed into the lysimeter columns (Appx 3.4). The ERT testing column is sealed at the base and around each electrode which allows the column to be filled completely by solution (no soil) or packed with a prepared soil sample. By packing the column with soil samples or solution and including imaging targets at distinct locations with known geometry it is possible to compare the captured ERT image with the known physical configuration of the system or forward model. Sample configurations include homogenous NaCl solution, solution with an air void target, wetted soil matrix with a dry soil target, and a wetted soil matrix with air void (Appx. 3.5). Imaging targets are all two inches in diameter and are centered in the horizontal plane of the imaging region. Tomography data produced from this series of control experiments is used to refine inversion parameters in Andrew Binley's R2 software package to improve image reconstruction (Appx. 3.6).

Appendix 3.4: ERT array testing column.

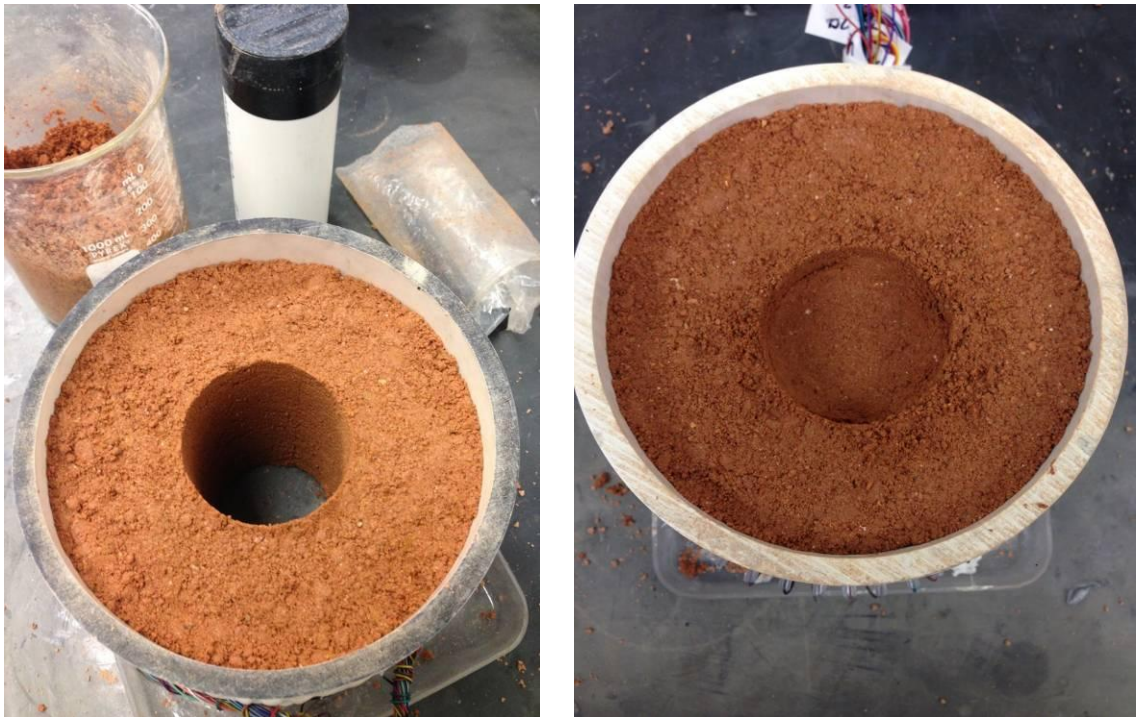

Appendix 3.5: ERT array testing columns. Column on left shows wetted soil with air void target design, where the column shown on the right has wetted soil with a dryer more resistive soil core target. Similarly, an air void is created in the center of a NaCl solution sample by placing an empty glass beaker in the center of the imaging field.

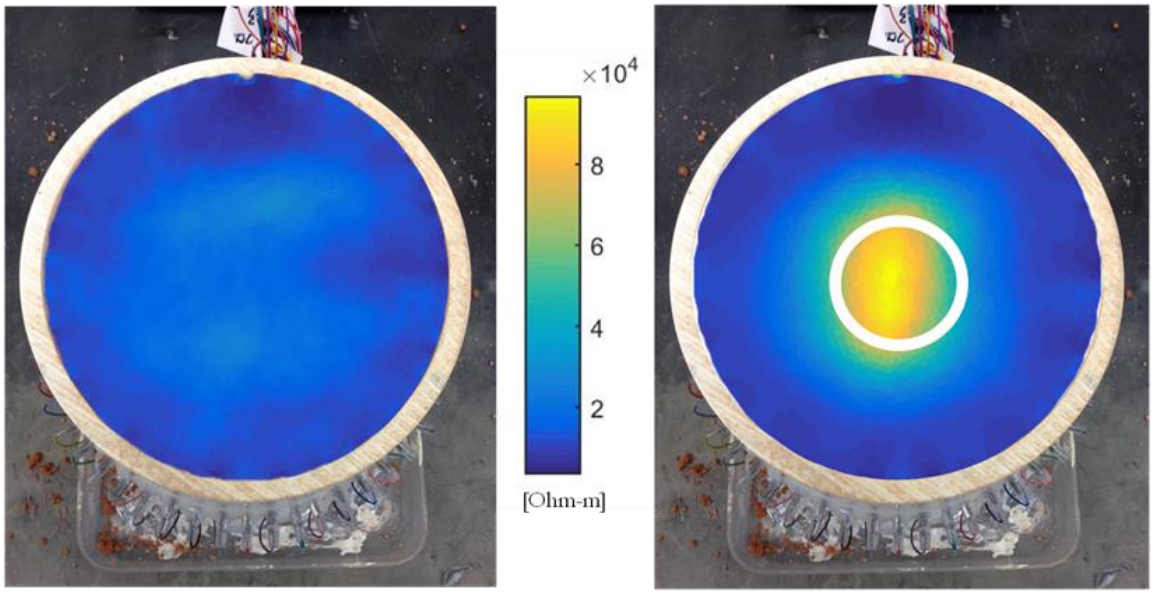

Appendix 3.6: ERT array test showing results from a homogenous system on the left and a heterogeneous system with an imaging target outlined in white on the right.

Calibration data is collected by Dr. Mine Dogan for the SRS sandy loam soil. Using a METER Hyprop instrument, soil matric potential is related to water content and soil moisture release curves are developed (Appx. 3.7). This calibration allows water content to be determined by pressure measurements from the Decagon MPS-1 and MPS-6 matric potential probes in the lysimeter columns.

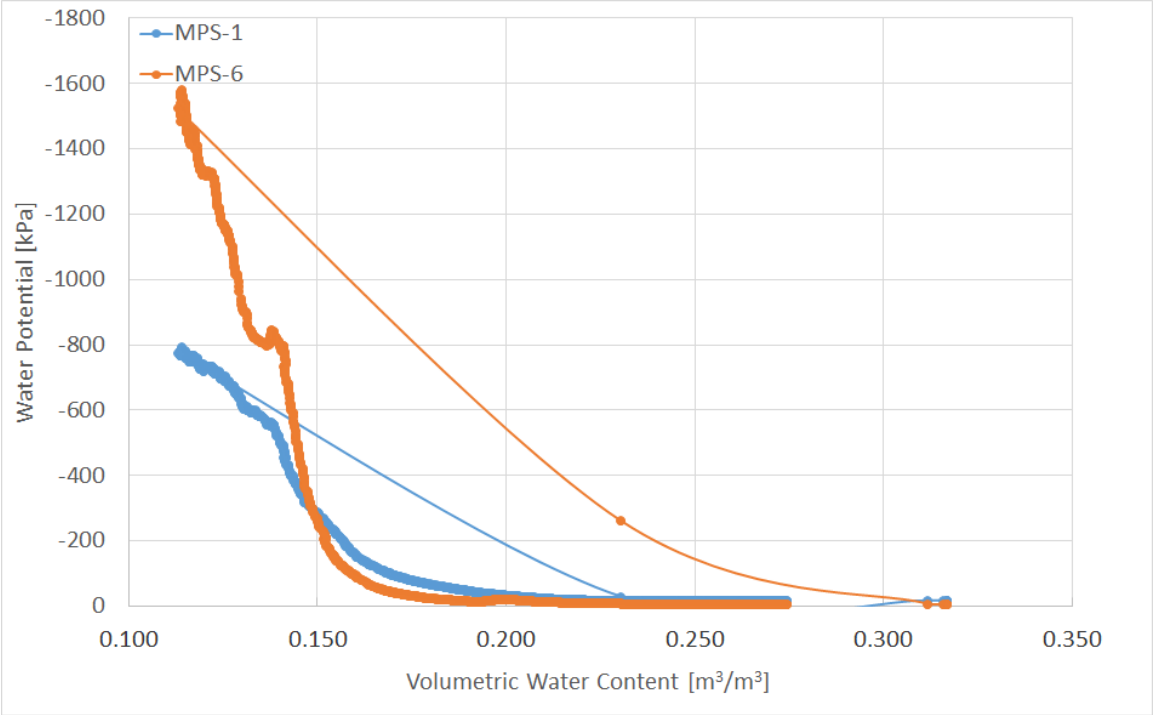

Appendix 3.7: Matric potential probe calibration data collected with METER Hyprop using SRS sandy loam soil. Data collected by Dr. Mine Dogan at Clemson University in 2015.

Calibration data for Omega load cells is collected to establish a measurement window or range and linearly correlates output signal to a weight value (Appx. 3.8).

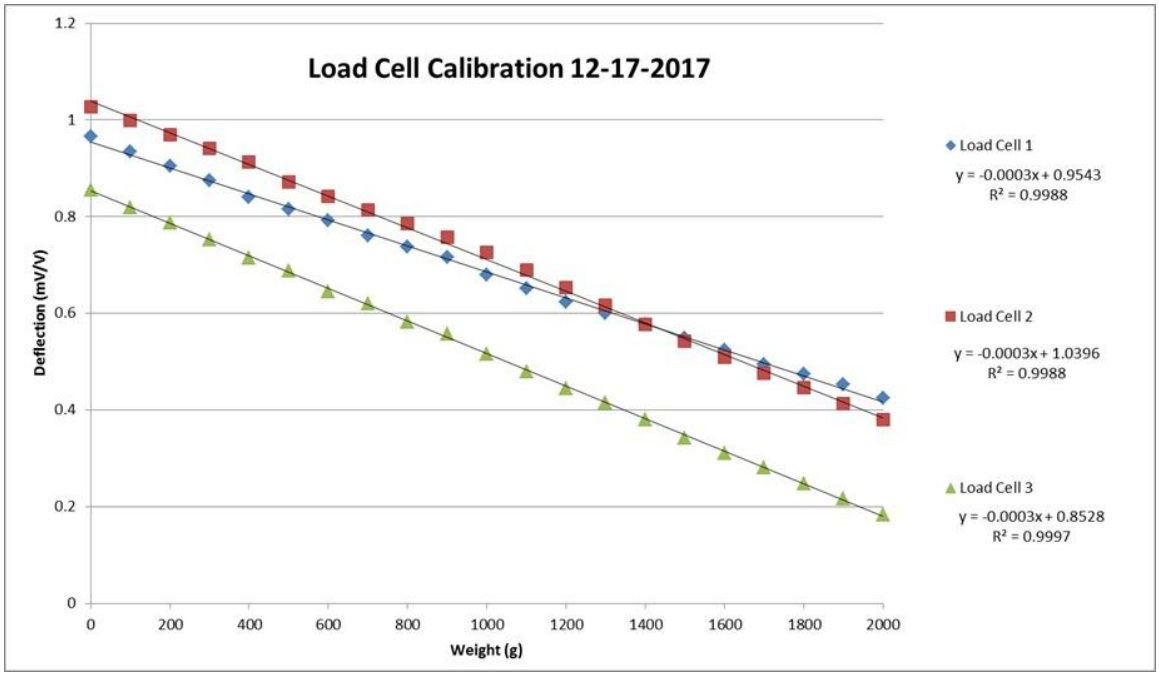

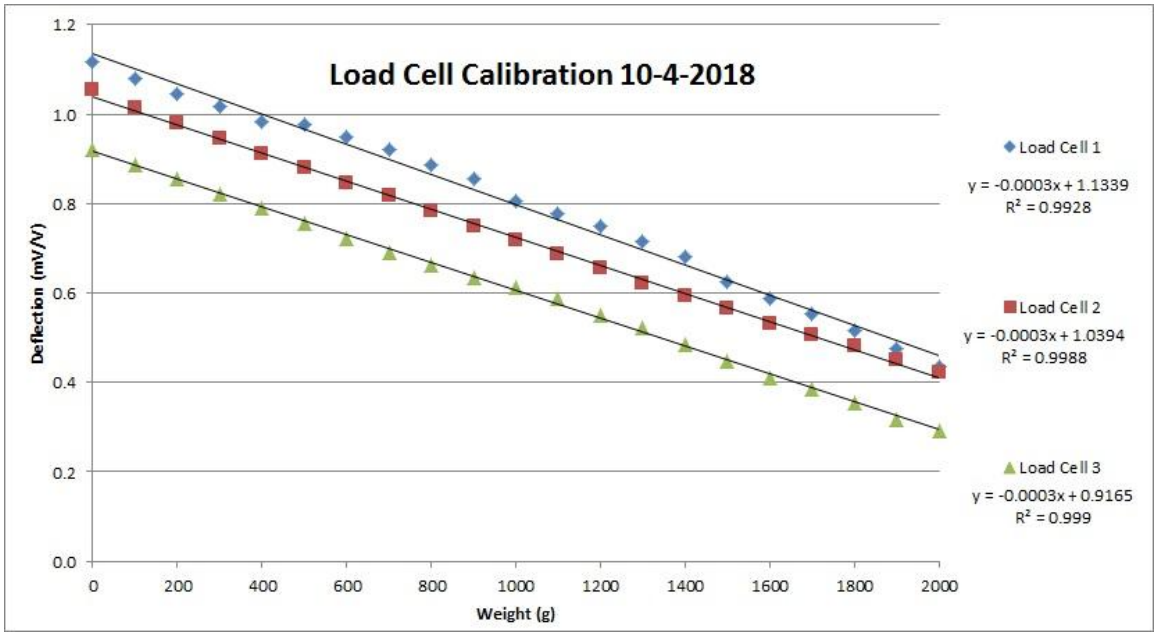

Appendix 3.8: Lysimeter load cell calibration data used to convert sensor output of mV/V to an associated mass load.

4: CT IMAGING COLUMNS

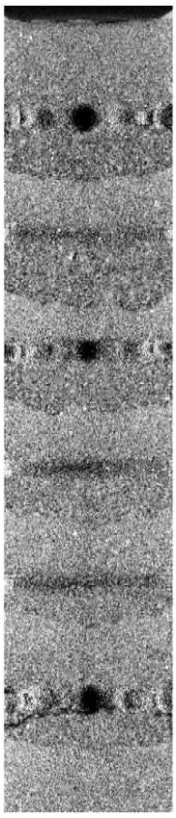

Appendix 4.1: X-ray cross sectional slice of CT column CT1 after packing and electrode installation. Packing layers are visible and X-ray attenuation by steel electrodes is also visible at tiers 1, 3 and 6.

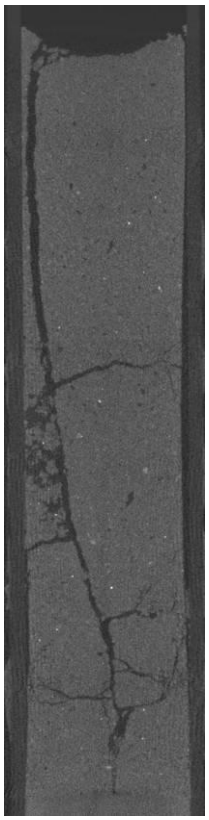

Appendix 4.2: X-ray cross sectional slice of CT column CT2 after packing and electrode installation.

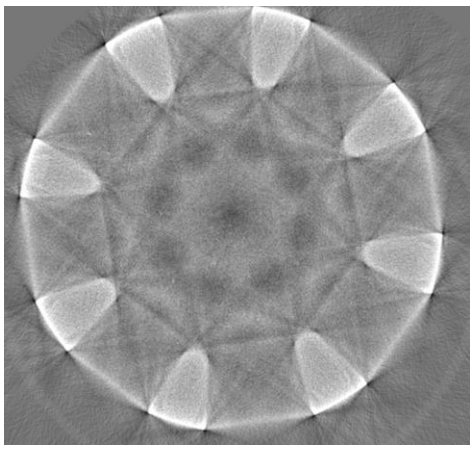

Appendix 4.3: Cross-sectional X-ray image of horizontal electrode plane in CT column CT1 where stainless steel electrodes are used. Artifacts from attenuation are clearly visible and no soil matrix is discernible.

Appendix 4.4: Photos taken of CT column CT1 the day following the experiment.

After flow was halted in the CT1 experiment, the upper cap was removed and the column was allowed to evaporate overnight. Pressure buildup within the column was large enough to cause an upper section of soil to fracture, separate and then rise in the column pushing ponded influent with blue tracer over the column walls causing it to spill over into secondary containment as seen in the image to the left. This soil section likely acted as a confining layer to air pressure, being overlain by ponded solution and saturated.

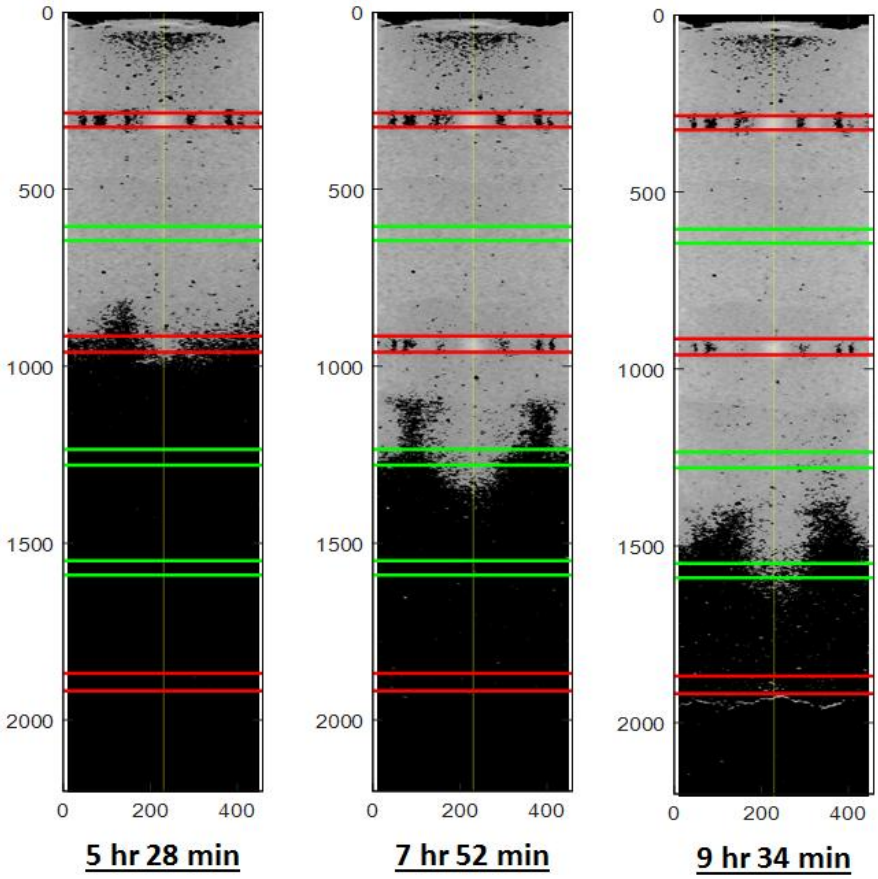

Appendix 4.5: Additional time steps of CT scan images for CT1 homogenous column experiment.

Additional flow scans for homogeneous CT column CT1 show the 5.5 hour arrival time of the wetting front at tier 3, when finger flow is starting to initiate. Additionally at 8 hours when vertical resistivity is holding constant but air may be redistributing upward. Lastly, at 9.5 hours when the first sign of water content is visible in the lower horizontal crack, despite the finger being a few centimeters away. An indication that some dispersed fluid was perhaps not being detected by the X-rays until it begins to accumulate in the crack.

5: LYSIMETER COLUMNS

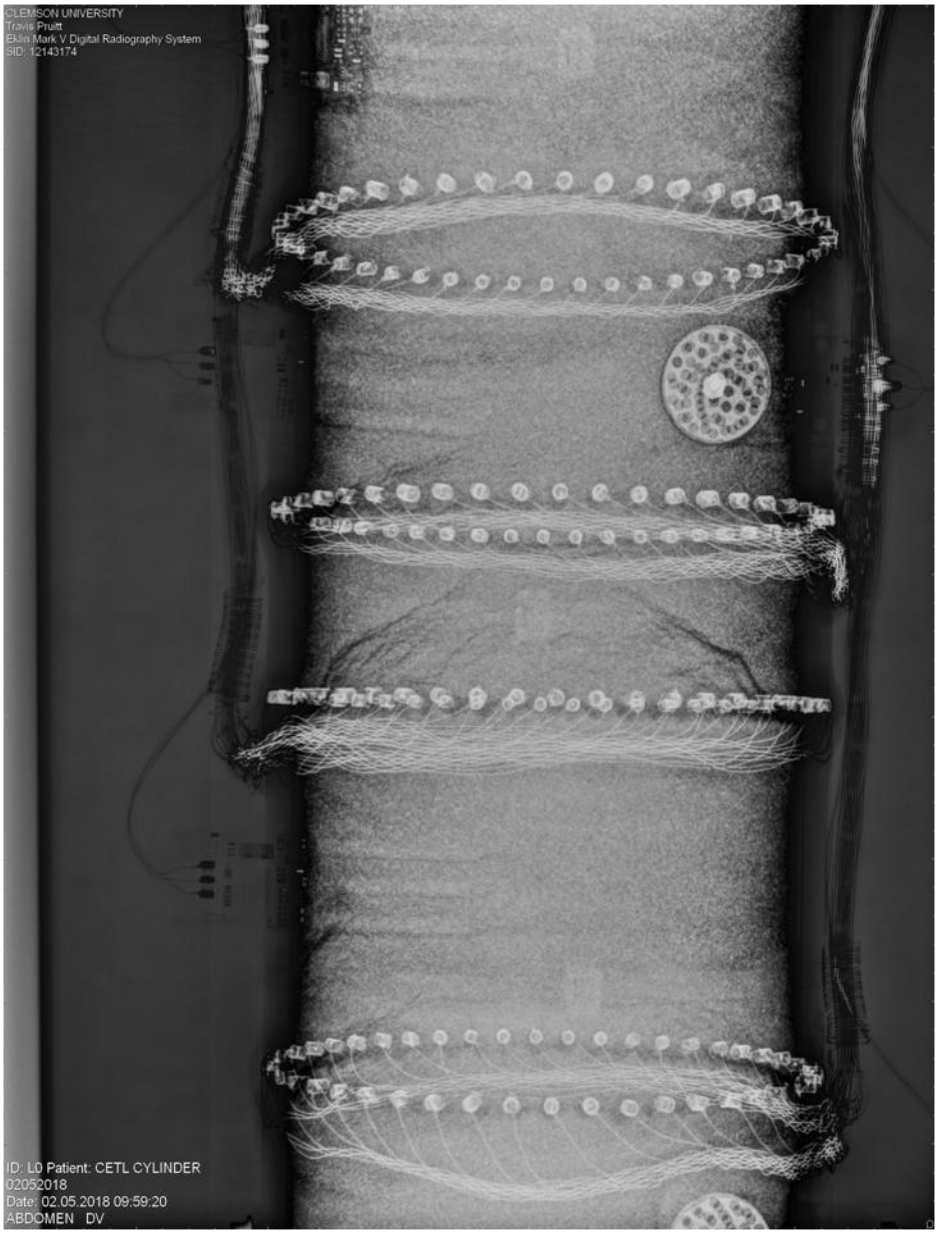

Appendix 5.1: Longitudinal X-ray of upper portion of lysimeter LYS-1. Moisture and matric potential probes can be seen along with rings of electrodes and faint outlines of zip ties used to hold external cables in place. Also notable is the slight concavity of the soil profile near the walls of the column and the cracks propagating from the electrode tiers upward toward the center.

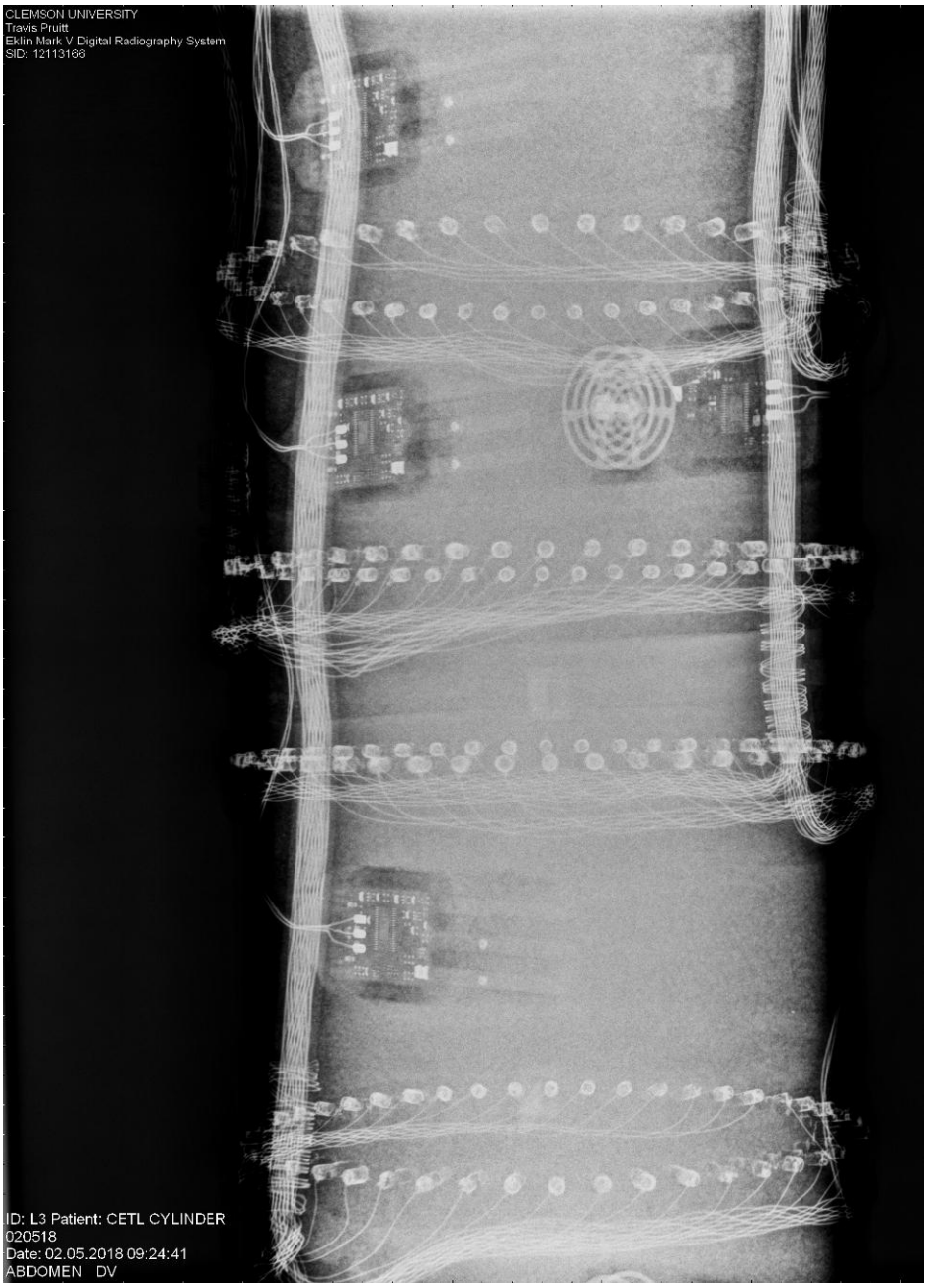

Appendix 5.2: Longitudinal X-ray of lysimeter LYS-2 showing probes and electrodes. External cabling looks closer in to the column as a result of the orientation of the image, one set of cables is in front and one is behind the column. Of note is the soil edge sitting straight and flush against the column wall as well as absence of cracking or layering.

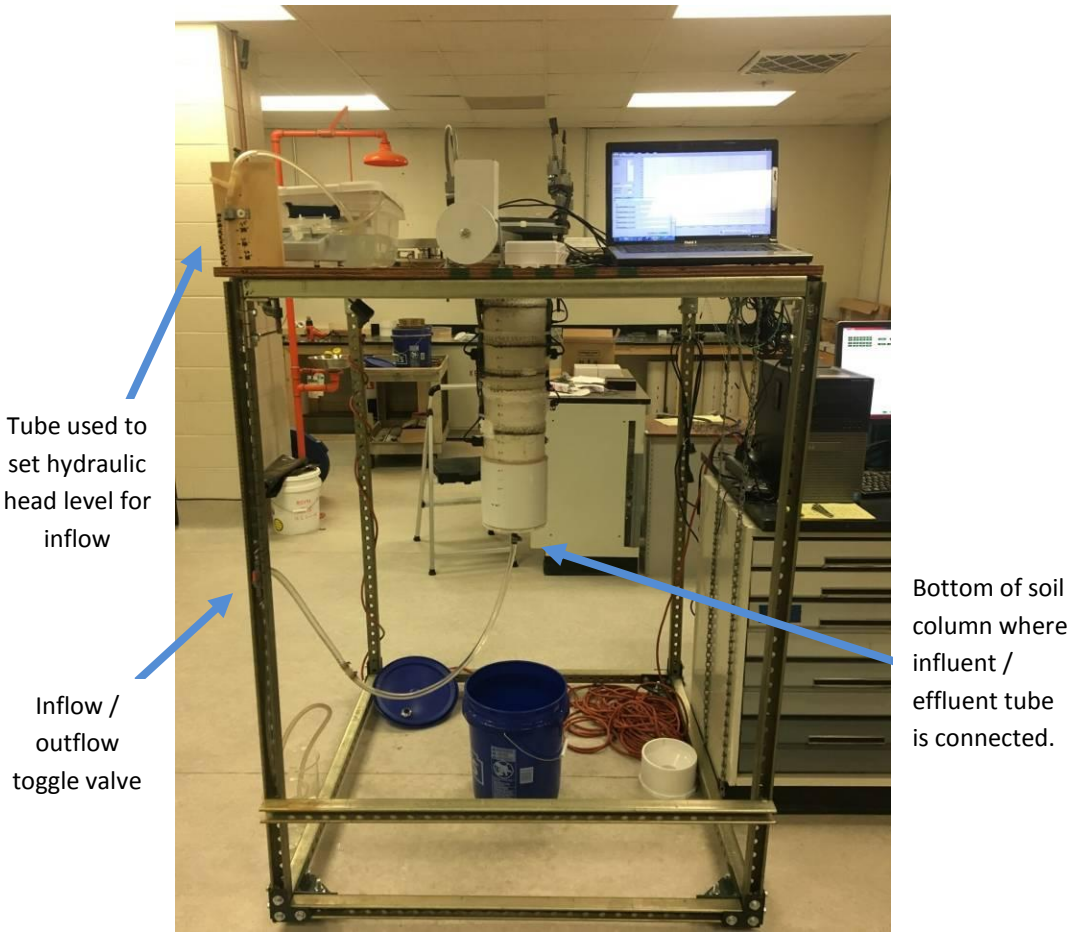

Appendix 5.3: Photo of uniform wetting front control experiment in lysimeter column LYS-1. Column is seen suspended by load cell assembly in a structural frame. Desktop PC to right is running COMSYS-Pro to collect resistivity data and laptop on frame is displaying probe and loadcell data for real time monitoring.

Appendix 5.4: Photo of setup of steady low flow infiltration experiment. Peristaltic pump feeds influent from reservoir into the columns upper surface (Appx. 4.5).

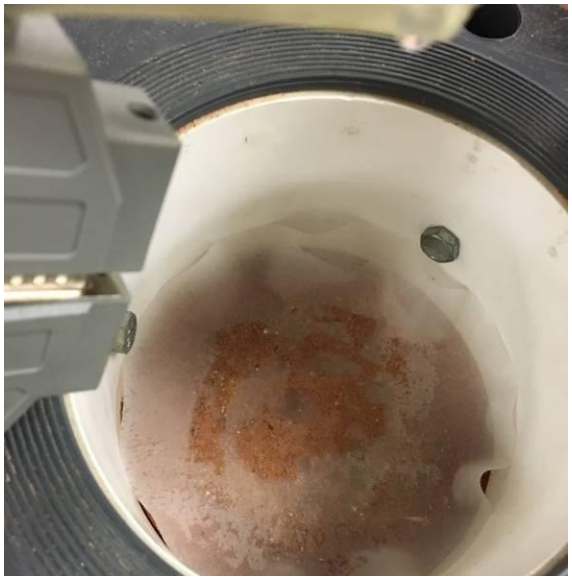

Appendix 5.5: Thin nylon mesh placed at upper soil surface of lysimeter to prevent soil erosion and disperse falling irrigation drips.

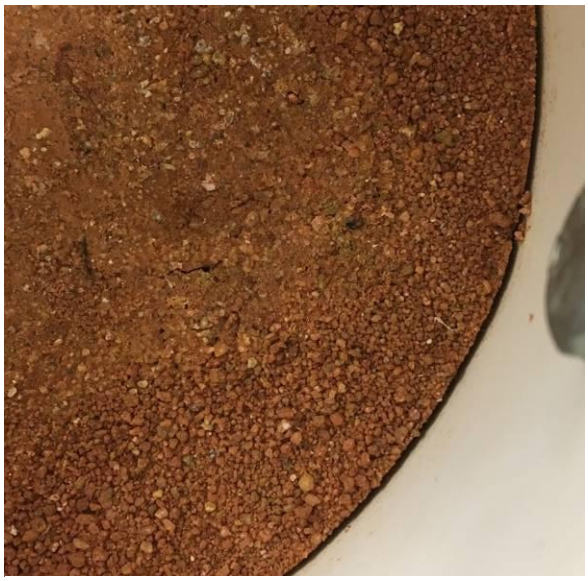

Appendix 5.6: Contact area between soil matrix and column wall at the upper soil boundary. A small gap is seen to have developed as soil shrinks from drying.

Appendix 5.7: Photo on left shows the offset orientation of engineered macropore. Photo on right shows drip location of irrigation indicated by blue tracer dye.

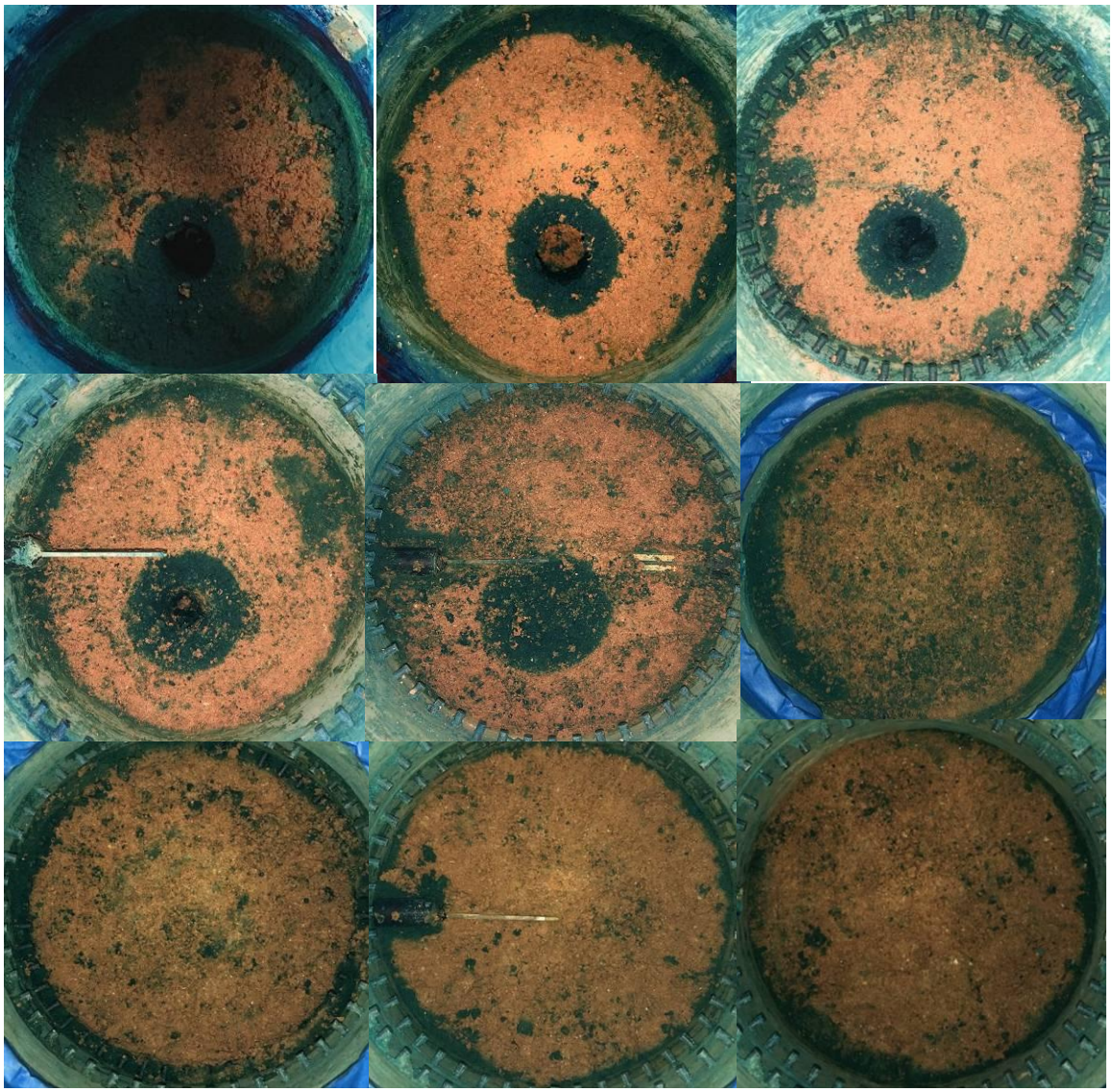

Appendix 5.8: Excavated cross-sections of macropore experiment in LYS-2. Top left to bottom right, depths from soil surface are 1 inch, 3 inches, 5 inches, 7 inches, 9 inches, 11 inches, 13 inches, 15 inches, and 16 inches.